University of Warsaw
Faculty of Physics

Doctoral Thesis

New insights into the problem of a single hole in an antiferromagnet

Nowe spojrzenie na problem pojedynczej dziury w antyferromagnetyku

Piotr Wrzosek

Supervisor:

dr hab. Krzysztof Wohlfeld, prof. UW

A dissertation in fulfillment of the requirements for the degree of Doctor of Philosophy

Warsaw, June 2023

Contents

List of Publications

1. K. Bieniasz, P. Wrzosek, A. M. Oleś, and K Wohlfeld, *From "weak" to "strong" hole confinement in a Mott insulator*, SciPost Physics **7** (5), 066 (2019).

2. P. Wrzosek, K. Wohlfeld, D. Hofmann, T. Sowiński, and M. A. Sentef, *Quantum walk versus classical wave: Distinguishing ground states of quantum magnets by spacetime dynamics*, Physical Review B **102** (2), 024440 (2020).

3. P. Wrzosek and K. Wohlfeld, *Hole in the two-dimensional Ising antiferromagnet: Origin of the incoherent spectrum*, Physical Review B **103** (3), 035113 (2021).

4. P. Wrzosek, A. Kłosiński, K. Wohlfeld, and C. E. Agrapidis, *Rare collapse of fermionic quasiparticles upon coupling to local bosons*, Phys. Rev. B **107**, 205103 (2023).

5. P. Wrzosek, A. Kłosiński, Y. Wang, M. Berciu, C. E. Agrapidis, and K. Wohlfeld, *The fate of the spin polaron in the 1D antiferromagnet*, arXiv:2203.01846 [submitted].

List of Abbreviations

1D	one-dimensional; one dimension.
2D	two-dimensional; two dimensions.
ARPES	angle-resolved photoemission spectroscopy.
BCS	Bardeen–Cooper–Schrieffer.
ED	exact diagonalization.
***high-*T_c**	high-temperature.
SAW	self-avoiding walk(s).
LRO	long-range order.
LSW	linear spin-wave theory.
SCBA	self-consistent Born approximation.
UV	ultraviolet.

Chapter 1

Introduction

Strongly interacting electron systems are one of the core problems studied in condensed matter physics. A good example can be a Mott insulating transition metal oxide with a partially filled d band [1]. Based on the band theory, one could expect such a system to be a conductor. But it does not have to be the case when the Coulomb repulsion between two electrons put on the same d orbital is sufficiently strong. Instead of the Bloch wave [2, 3], which is typically formed in "uncorrelated" metals, the high potential barrier from Coulomb interactions leads to the localization of the electrons [4, 5]. In the end, the system may become insulating.

There are numerous compounds characterized by such behavior. Standard examples are copper oxides, also called cuprates, e.g. La_2CuO_4, $Ca_2CuO_2Cl_2$ [6, 7]. In these materials, copper is formally in a $3d^9$ configuration with copper ions organized in square lattices [8]. The whole structure consists of a set of CuO_2 planes with almost no transfer of electrons between the planes, see Fig. 1.1(a-b). Effectively, this makes them two-dimensional systems. Moreover, these materials can be doped with holes. The doping is realized when the lanthanum or the calcium atom is substituted with an atom that has different valence. To maintain the crystal structure, the missing electrons are pulled from the CuO_2 planes, and this way holes are introduced to the CuO_2 planes [9]. For a doping x, the corresponding materials are for instance $La_{2-x}Sr_xCuO_4$ [10] or $Ca_{2-x}Na_xCuO_2Cl_2$ [11, 12]. Besides hole doping, there is a class of materials where electron doping is possible [13–16].

At zero temperature and without doping these materials are antiferromagnets with superexchange as the driving mechanism for the magnetic correlations [8]. Upon doping the temperature of the phase transition to the ordered state goes down rather quickly and the long-range order is no longer present for dopings higher than 5% [18]. At the same time, short-range antiferromagnetic correlations are still there. Further doping leads to a superconducting state [8, 17–20]. A schematic phase diagram is shown in Fig. 1.1(c). Importantly, this is not an ordinary BCS superconductor but the so-called *high-T_c* superconductor [19]. The fundamental difference lies in the pairing mechanism. For typical superconductors, the effective attractive interaction between the electrons comes from the coupling to phonons [21]. But in the *high-T_c* superconductors the electron pairing is rather not realized through phonons. It is believed that pairing is possible due to coupling to the magnetic excitations yet a possible mechanism is still a subject of scientific debate due to difficult and therefore incomplete studies of its details [22]. Finally, the name comes from unexpectedly high temperatures for the phase transition to the superconducting state reaching the order of $100K$ [23]—much higher than in the case of conventional superconductors (typically few Kelvins).

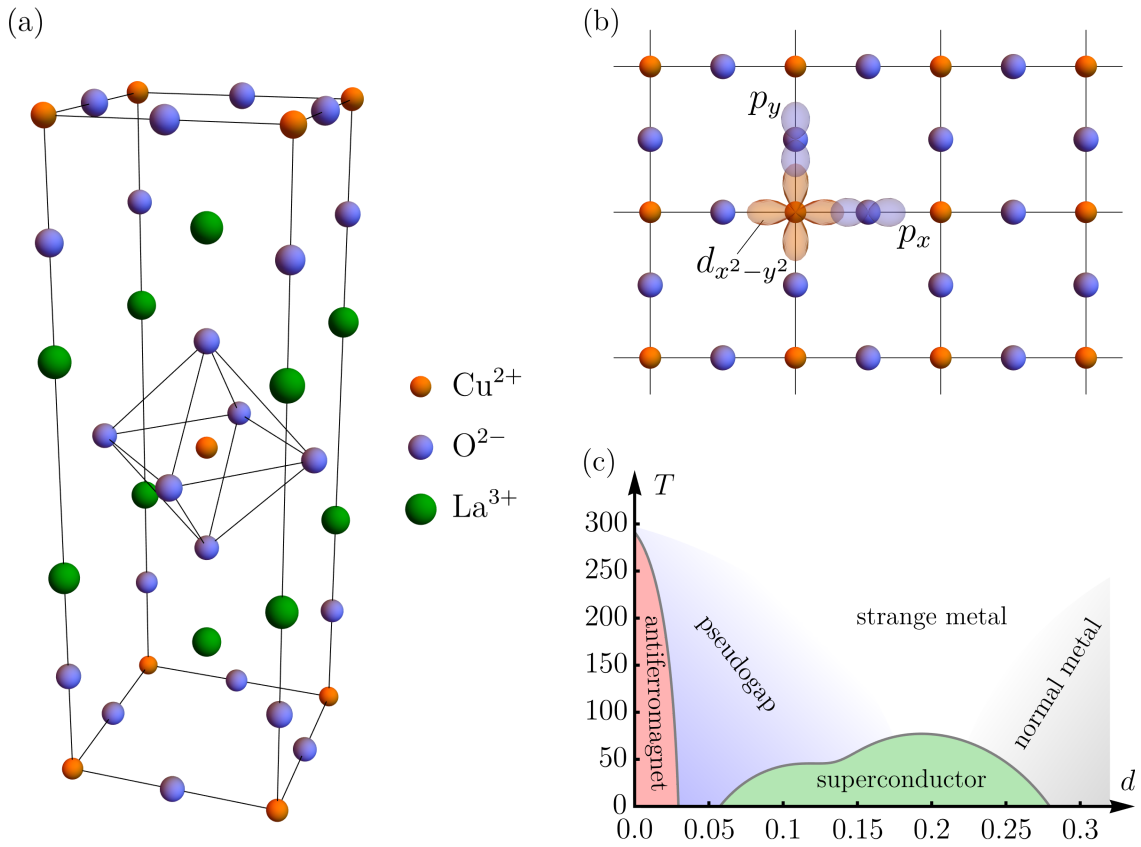

Figure 1.1: (a) Crystal structure of La_2CuO_4. (b) Single copper oxide plane. Copper ions form a square lattice. Orbitals hosting doped holes and responsible for magnetic properties have been denoted around one of the copper ions. (c) Temperature T and hole doping d dependent schematic phase diagram of a cuprate compound (inspired by Ref. [17]).

With a closer look at the electronic structure, we can see the $3d^9$ configuration of the copper ions makes one of the five d orbitals half-filled in the undoped system since the d shell can contain a maximum of 10 electrons at the same time. Due to a crystal field, the orbitals are significantly split in energy with the $x^2 - y^2$ orbital being energetically least favorable [18]. Thus in low enough temperatures, compared to the energy split between the highest orbitals, this would be the only orbital that is not fully filled with electrons. Effectively, the system can be seen as a single-band problem. With doping, the electrons are pulled from the oxygen ions in the copper oxide planes. Each introduced hole forms a so-called Zhang-Rice singlet [24] on the four oxygen ions around the center copper ion. But the way this singlet moves and interacts allows us to describe this system as if the electron was removed from the copper ion. This makes the single-band Hubbard model [25] on the square lattice a good candidate for an effective model of cuprates.

1.1. Effective model for cuprates

Throughout many years of studies, it has been well established that the Hubbard model with the electron hopping up to the 3$^{\text{rd}}$ nearest neighbor captures well many

key features of the cuprate physics [26]. Some studies also suggest that introducing a nearest neighbor attractive interaction V between the electrons improves its accuracy even further [27]. At the same time, the complexity of the model due to its large Hilbert space (4 states per site; e.g. over $4 \cdot 10^9$ states for a lattice with only 16 sites) makes it difficult to study numerically. On the other hand, the Hubbard model with just nearest neighbor hopping is exactly solvable in 1D [28, 29]. Unfortunately, one cannot say the same about its 2D counterpart, or at least such a solution has not yet been discovered [4].

Nevertheless, the assumption that onsite Coulomb repulsion is much stronger than electron hopping ($U >> t$), which is true for cuprate compounds, allows for effective treatment of the Hubbard model. For large U it is very unlikely to find $d_{x^2-y^2}$ orbitals doubly occupied. As shown in previous works [30], these states can be projected out or more precisely treated as virtual states. With this approach, the nearest neighbor Hubbard model with hopping t and onsite Coulomb repulsion U in half-filling maps onto the Heisenberg model with spin exchange $J = 4t^2/U$ where electrons are frozen in place. Away from half-filling, the electrons can start moving to unoccupied sites. Such a model, which is valid only for the case of strong electron repulsion U and for small dopings, is called the t–J model [18, 30] and it will be the central model for the studies presented in this dissertation. Its Hamiltonian reads,

$$\hat{H} = -t \sum_{\langle i,j \rangle \sigma} \hat{\tilde{c}}^{\dagger}_{i\sigma} \hat{\tilde{c}}_{j\sigma} + \text{H.c.} + J \sum_{\langle i,j \rangle} \left(\hat{\mathbf{S}}_i \hat{\mathbf{S}}_j - \frac{1}{4} \hat{\tilde{n}}_i \hat{\tilde{n}}_j \right). \tag{1.1}$$

The summation indexed by $\langle i, j \rangle$ runs over all pairs of sites i, j that are nearest neighbors, where the pair is simply defined as a two-element set $\{i, j\}$. The symbol $\sigma \in \{\uparrow, \downarrow\}$ represents z component of the electron's spin. Operator $\hat{\tilde{c}}^{\dagger}_{i\sigma} = \hat{c}^{\dagger}_{i\sigma}(1 - \hat{c}^{\dagger}_{i\bar{\sigma}} \hat{c}_{i\bar{\sigma}})$ creates electron only on sites that are not yet occupied by another electron [31, 32]. Operator $\hat{\tilde{n}}_i = \sum_\sigma \hat{\tilde{c}}^{\dagger}_{i\sigma} \hat{\tilde{c}}_{i\sigma}$ counts electrons on site i. It is equal to $\hat{n}_i = \sum_\sigma \hat{c}^{\dagger}_{i\sigma} \hat{c}_{i\sigma}$ for all the states without double occupancy. Finally, $\hat{\mathbf{S}}_i = (\hat{S}^x_i, \hat{S}^y_i, \hat{S}^z_i)$ is 3-component spin operator, where $\hat{\mathbf{S}}_i \hat{\mathbf{S}}_j = \sum_{\xi \in \{x,y,z\}} \hat{S}^{\xi}_i \hat{S}^{\xi}_j$ is a scalar product of the spin projections. In what follows, the z-axis is chosen as the spin quantization axis.

So far, the mentioned examples were *quasi*-2D systems. There is also a wide range of *quasi*-1D transition metal oxides, including cuprate compounds [33]. A good example is $Ba_2CuO_{3+\delta}$ [34]. Without doping this system is an antiferromagnet, with d band electrons localized similarly to the 2D case. Doping allows d band electrons to move along CuO chains while the hopping between the chains remains substantially suppressed. As well as the 2D case, the lightly doped 1D cuprates also can be relatively well described by the t–J Hamiltonian [35–37]. That being said, the current microscopic understanding of "the t–J physics" in the two cases is qualitatively very different.

1.2. Angle-resolved photoemission spectroscopy

To uncover the key difference between 1D and 2D cuprates, we introduce a technique widely used in the studies of cuprates—angle-resolved photoemission spectroscopy (ARPES) [38, 39]. With this technique, the electrons can be excited to leave the sample. This is possible due to the photoelectric effect when the energy of light shined at the sample is higher than the binding energy of electrons in the sample [40]. Typically this is realized with UV light, but dependent on the material even visible light

might be enough. By collecting the emitted electrons from different angles and measuring their energies one obtains information about the electronic band structure of the sample, i.e. the dispersion relation $E(k)$.

Removing an electron from the sample leaves a hole in the sample. Therefore with ARPES, one can gain access to the physics of a single or few holes introduced to an otherwise undoped system. This key feature of ARPES opens the door to the understanding of e.g. motion of a single hole added to a Mott insulator [20]. Fundamentally, there is a simple connection between the ARPES measurement and the single-particle Green's function, which makes the interpretation of the measurements relatively straightforward,

$$A(k,\omega) = -\frac{1}{\pi} \lim_{\delta \to 0^+} \mathrm{Im}\ G(k, \omega + i\delta), \tag{1.2}$$

where

$$G(k,\omega) = \langle \psi_0 | \hat{c}^\dagger_{k\sigma} \left(\omega - \hat{H} + E_0 \right)^{-1} \hat{c}_{k\sigma} | \psi_0 \rangle. \tag{1.3}$$

Here $A(k,\omega)$ is called a (single particle) spectral function, and it is proportional to the intensity of a signal measured by ARPES [20, 41] when detecting electrons with momentum k and energy ω. State ψ_0 is the ground state of the system before removing the mentioned electron $\hat{c}_{k\sigma}$ with momentum k and spin σ. E_0 is the energy of the ground state ψ_0. After the electron is removed, the initial state $\hat{c}_{k\sigma}|\psi_0\rangle$ is no longer the ground state and the system is allowed to evolve with propagator $\hat{G}(\omega) = \left(\omega - \hat{H} + E_0 \right)^{-1}$.

1.3. ARPES of undoped cuprates: state of the art

While the physics of undoped cuprates is well understood [1, 42, 43], lightly doped cuprates are a far richer playground for physical investigations. Among the challenging studies of doped copper oxides, the problem of a single hole introduced to the otherwise undoped cuprate is probably "the easiest from the hardest". In the literature, there are few well-established concepts when it comes to the motion of a single hole in the antiferromagnet. The two most important for this thesis are *spin-charge separation* in 1D systems [28, 35, 44–51] and *spin polaron* in 2D setup [52–59]. It is crucial to understand both of them, at least at the conceptual level.

1.3.1. Spin-charge separation in 1D

Let us start with the 1D case. At half-filling, the system is a chain of immobile electrons with spins ordered antiferromagnetically. In reality, such perfect ordering is spoiled by the spin fluctuations from the exchange processes, but at a starting point, this is neglected. With the ARPES experiment, we can remove one electron from the chain and thus create a hole, as shown in Fig. 1.2.(a). Now the electrons can jump to this one unoccupied site. As a result, the hole moves in the opposite direction. At the same time, two neighboring spins become aligned ferromagnetically [Fig. 1.2.(b)]. This costs some energy since it locally breaks the antiferromagnetic order. On the other hand, the further motion of the hole (now called a holon) away from the pair of ferromagnetically aligned spins does not spoil the antiferromagnetic ordering of the rest of the spins—it just shifts them [Fig. 1.2.(c)]. On top of that, the superexchange process opens a way for pair of ferromagnetically aligned spins to move as well [Fig. 1.2.(d)]. In the

presence of spin fluctuations, such a pair becomes a mobile quasiparticle—a spinon—the fundamental excitation of 1D antiferromagnet that carries a spin $s = \frac{1}{2}$. In the thermodynamic limit, the holon and the spinon can separate and move independently of each other.

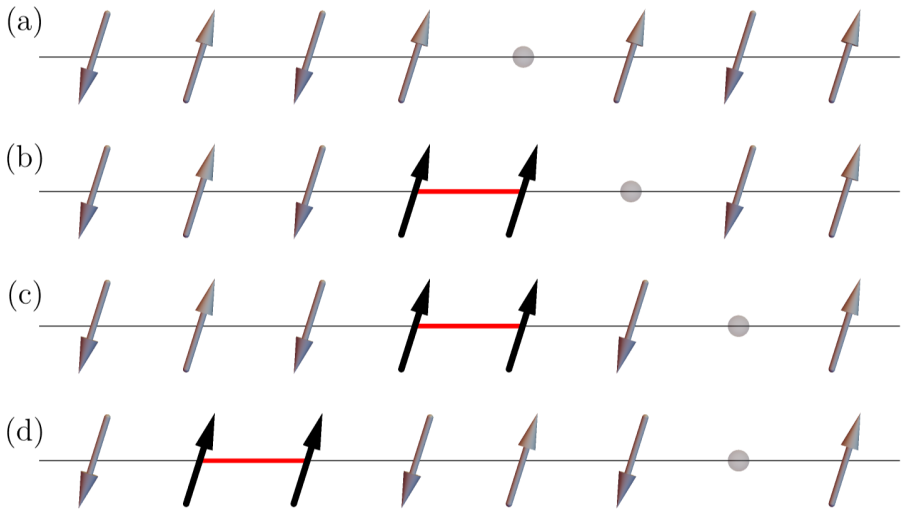

Figure 1.2: Spin-charge separation picture in the 1D t–J model (1D antiferromagnet). A hole (gray circle) is introduced to the system by exciting an electron out of the sample in the ARPES experiment. Initially, the propagation of the hole leads to the creation of a single spin excitation—pair of ferromagnetically aligned spins (black arrows) (a)-(b). Such an excitation costs energy as it locally breaks the order in the system. The unsatisfied bond is denoted in red. The hole (now called holon) can move further away without spoiling the antiferromagnetic order (b)-(c). Moreover, the spin exchange processes allow for the motion of the spin excitation (now called spinon) (c)-(d). As a result, the holon (charge excitation) and the spinon (spin excitation) can separate and move independently of one another.

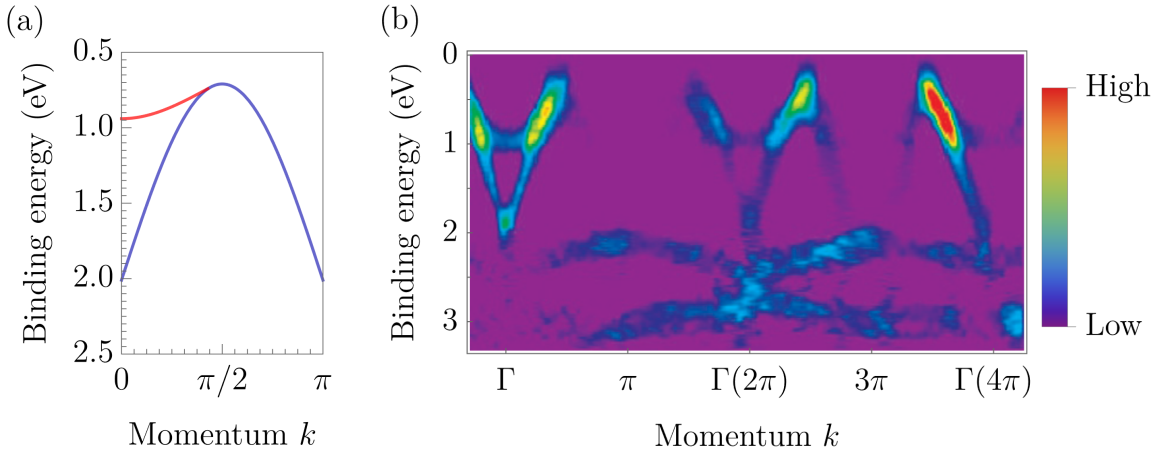

Figure 1.3: (a) Theoretical holon dispersion (blue solid line) and the edge of the spinon-holon continuum (red line) of the 1D cuprate. (b) Experimental data from ARPES measurement on 1D cuprate compound ($SrCuO_2$). Theoretically predicted features are visible in the experiment. Figures taken from Ref. [35]

The described phenomenon is visibly reflected in the shape of the spectral function

of the single hole injected into the 1D antiferromagnet. Analytically calculated main features of such a spectral function are shown in Fig. 1.3.(a). The red line follows the edge of the so-called spinon-holon continuum. The blue line is, on the other hand, called the holon branch, since it corresponds to a dispersion of a free holon. Those features of the spin-charge separation to some extent can be also seen in the ARPES experiments [35]. The experimental ARPES spectrum on a 1D undoped cuprate is shown in Fig. 1.3.(b). At first sight, a comparison between the two figures supports the spin-charge separation concept. But the resolution of such experiments is typically very poor. Later in this work, it will be shown that good resolution is crucial in determining whether spin-charge separation happens in real materials. This has to be verified since, in reality, 1D cuprates are rather *quasi*-1D systems, with the coupling between the chains strong enough to alter their physics (see Sec. 5.3).

1.3.2. Spin polaron in 2D

When we go beyond 1D systems, the situation changes. Initially, when the added hole makes the first move, the difference is rather quantitative. Instead of one unsatisfied bond (pair of neighboring parallel spins), there are three bonds aligned ferromagnetically. The qualitative difference appears when the hole moves further away. Now with each hop of the hole, more unsatisfied bonds are created, leading to the growth of the energy of the system.

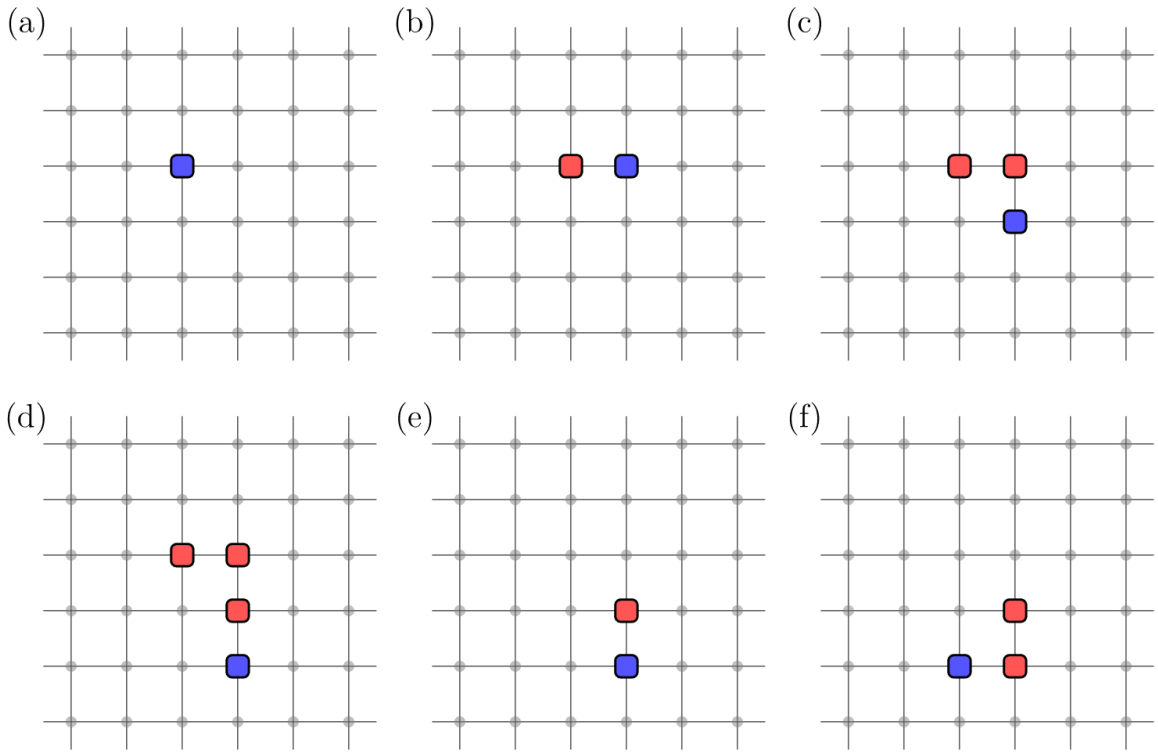

Figure 1.4: Propagation of a hole in the 2D antiferromagnet (t–J model on a square lattice). Initially, the hole (blue square) is introduced to the system (a). The hole moves through the lattice exciting (or annihilating) magnons (red squares) (a)-(d), (e)-(f). Magnons cost energy and thus the hole cannot move freely. But pairs of neighboring magnons can be annihilated by the spin exchange processes (d)-(e). Altogether, the hole dresses in a small cloud of magnons and forms a weakly mobile quasiparticle.

A standard physical picture in this case is then expressed in terms of a hole that is propagating through the system and exciting (or annihilating) magnons (magnetic excitations) with each hop. The initial antiferromagnetic configuration of spins is now represented by a vacuum state for the holes and magnons. Once the hole is introduced, it will propagate through the system creating magnons (which represent spins misaligned with respect to the original AF order). This is shown in Fig. 1.4. Due to the growing potential from introduced magnons, the hole is bounded in space. But the exchange processes present in the t–J Hmiltonian (1.1) can cause spin-flips and repair destroyed ordering—a pair of neighboring magnons can be annihilated and thus the hole can be liberated from the confining potential. In the end, the hole can dress in a cloud of magnons and form a weakly mobile quasiparticle—a spin-polaron.

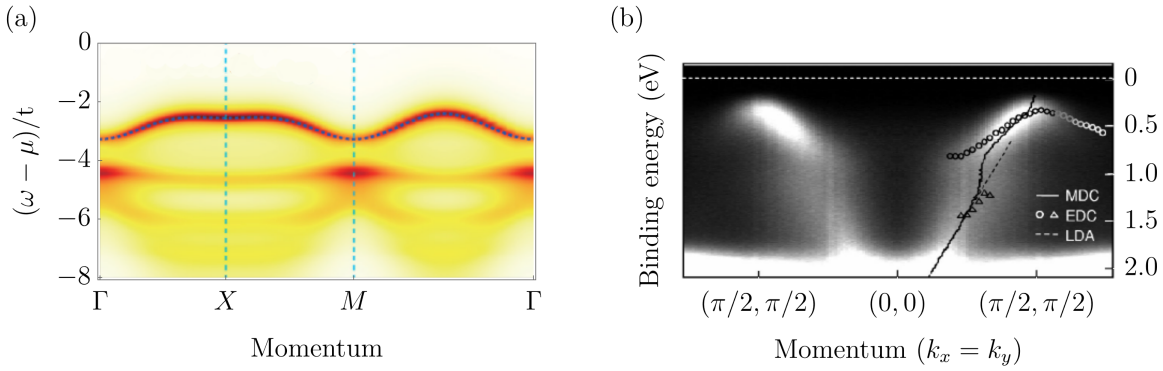

Figure 1.5: (a) Self-consistent Born approximation treatment of a spectral function of a single hole introduced to the otherwise undoped 2D t–J model. The figure was taken from Ref. [60]. (b) Experimental data from ARPES measurement on a 2D cuprate compound $Ca_2CuO_2Cl_2$. The figure was taken from Ref. [61]. Theoretically calculated existence and dispersion of a quasiparticle find a confirmation in the experimental data.

The theoretically calculated and experimentally measured ARPES on a 2D undoped cuprate is shown in Fig. 1.5. The notable difference concerning the 1D case is the existence of a dispersive delta-like peak in the spectrum at the ground state energy of the system that is separated from the broad continuum [60]. This indicates the existence of the mobile quasiparticle. On top of that, the agreement with the dispersion of the experimentally measured high-intensity peak further supports the spin polaron picture in 2D [61]. For this reason, the spin polaron has earned its popularity and it was considered in many previous works [52–59].

1.4. Issues with current knowledge

1.4.1. Reasons for differences between 1D and 2D cases

The physics of a single hole in 1D cuprates is understood in terms of spin-charge separation. On the other hand, in the 2D cuprates the doped hole dresses in a cloud of magnons to form a spin polaron. This means that the state-of-the-art description and understanding of a single hole in the antiferromagnet depends on the dimension one considers. The disadvantage of having two different languages to talk about 1D and 2D cuprates becomes transparent when it comes to relating the physics of the hole in these two cases. The different description does not allow for a direct comparison. It is not

clear, for example, to what extent the physics of a hole in 1D and 2D cuprates is indeed different. It may as well be much more similar than described in the existing literature. But to unambiguously relate the two cases one would need to use the same description for both. Therefore, an important question is whether we can have a unified approach to this problem. So far, the efforts in this direction only considered 2D t–J model described in the 1D language in an attempt to explain the ARPES experiments on 2D cuprates by making connections to the spin-charge separation [62]. An alternative approach, which will be the core method of this thesis (see Sec. 1.5), is to do the opposite, i.e. to describe both the 1D and 2D t–J model in terms of spin polaron physics.

1.4.2. Long-range order in *quasi*-1D cuprates

When discussing 1D cuprates one should keep in mind that these are not true 1D systems but rather *quasi*-1D systems [33, 34]. Precisely, these are bulk crystals with copper-oxygen chain-like structures spanned across the material. One can consider a single chain to be a 1D system only approximately due to the small but finite coupling between the neighboring chains [63, 64]. This coupling leads to the existence of the antiferromagnetic long-range order (LRO) in *quasi*-1D cuprates at low temperatures [63]. The spin-charge separation, on the other hand, assumes the absence of the LRO. But what replaces the spin-charge separation in case it is no longer a valid picture? Could it be a spin polaron? The answer to this question may have important consequences for the description of the ground state of a single hole in a cuprate as well as for the interpretation of the ARPES measurements on *quasi*-1D cuprates.

1.4.3. Role of magnon-magnon interactions

A typical approach to 2D spin polaron physics is based on the linear spin-wave theory (LSW) [5]. The LSW is an approximation where terms in the Hamiltonian of the order higher than quadratic in bosonic operators are simply discarded. This excludes for example the magnon-magnon interactions from the considerations. In principle, the existence of the LRO suggests that LSW should work well and the approximation made is qualitatively insignificant. But when the hole moves through the antiferromagnet several magnons are created spoiling the antiferromagnetic order. In this situation, it is not clear whether LSW can be successfully applied. Similarly, if we consider 1D t–J model (or 2D t–J model with finite doping) then LSW may no longer be applicable due to lack of LRO. Altogether, it becomes important to ask about the role of the magnon-magnon interactions in these systems, e.g. in the formation of a spin polaron.

1.5. Core method of this thesis: magnon-holon basis of 1D and 2D t–J models

The different understanding of the same model, dependent on the dimensionality of the lattice (spin-charge separation in 1D and spin polaron quasiparticle in 2D square lattice), did not help with recognizing that some of the results presented in the previous works were not sensible. In this work, a different approach has been taken. Regardless of the dimensionality and whether it is Ising limit in the consideration or not, the Hamiltonian is reexpressed using the spin polaron language. Let us carefully go through

all the corresponding transformations of the Hamiltonian, laying a base for most of the considerations presented in this work.

1.5.1. Transformation to magnon-holon basis

In the polaronic description, the electron operators $\hat{\tilde{c}}_{i\sigma}$ and spin operators $\hat{S}_i^{\xi}$ are replaced with combinations of spinless fermion (holon) operators $\hat{h}_i$ and bosonic (magnon) operators $\hat{a}_i$. In the standard way, this typically is incorporated by applying the so-called slave-fermion [53, 54] and Holstein-Primakoff [65] transformations. The essence of the slave-fermion transformation lies in the possibility of rewriting the electron creation and annihilation operators such that the charge and the spin degrees of freedom become split into two operators. Holstein-Primakoff allows us to further reexpress spin operators in terms of bosons $\hat{a}_i$.

We start by rotating spins in one sublattice (i.e. every second site in each direction) by π around the x axis. After the rotation the t–J Hamiltonian reads,

$$\hat{H}_{\mathrm{rot}} = -t \sum_{\langle i,j\rangle\sigma} \hat{\tilde{c}}^{\dagger}_{i\sigma}\hat{\tilde{c}}_{j\bar{\sigma}} + \mathrm{H.c.} + J\sum_{\langle i,j\rangle}\left(\hat{S}_i^x\hat{S}_j^x - \hat{S}_i^y\hat{S}_j^y - \hat{S}_i^z\hat{S}_j^z - \frac{1}{4}\hat{\tilde{n}}_i\hat{\tilde{n}}_j\right), \tag{1.4}$$

where $\bar{\sigma} \equiv -\sigma$. By introducing the ladder operators,

$$\hat{S}_j^{+} = \hat{S}_j^x + i\hat{S}_j^y, \tag{1.5}$$

$$\hat{S}_j^{-} = \hat{S}_j^x - i\hat{S}_j^y, \tag{1.6}$$

one can write the rotated t–J Hamiltonian in the following form,

$$\hat{H}_{\mathrm{rot}} = -t \sum_{\langle i,j\rangle\sigma} \hat{\tilde{c}}^{\dagger}_{i\sigma}\hat{\tilde{c}}_{j\bar{\sigma}} + \mathrm{H.c.} + \frac{J}{2}\sum_{\langle i,j\rangle}\left(\hat{S}_i^{+}\hat{S}_j^{+} + \hat{S}_i^{-}\hat{S}_j^{-}\right) - J\sum_{\langle i,j\rangle}\left(\hat{S}_i^z\hat{S}_j^z + \frac{1}{4}\hat{\tilde{n}}_i\hat{\tilde{n}}_j\right). \tag{1.7}$$

The above-performed transformation can be denoted as,

$$\hat{H}_{\mathrm{rot}} = \mathcal{R}_A\hat{H}\mathcal{R}_A^{-1}, \tag{1.8}$$

where $\mathcal{R}_A$ denotes the rotation of spins in sublattice A. Accordingly, the states of the system also have to be transformed,

$$|\psi_{\mathrm{rot}}\rangle = \mathcal{R}_A|\psi\rangle, \tag{1.9}$$

such that,

$$\langle\psi_{\mathrm{rot}}|\hat{H}_{\mathrm{rot}}|\psi_{\mathrm{rot}}\rangle = \langle\psi|\mathcal{R}_A^{\dagger}\mathcal{R}_A\hat{H}\mathcal{R}_A^{-1}\mathcal{R}_A|\psi\rangle = \langle\psi|\hat{H}|\psi\rangle. \tag{1.10}$$

The last equation is true since for the rotation $\mathcal{R}^{\dagger} = \mathcal{R}^T = \mathcal{R}^{-1}$. When we write all the states in the eigenbasis of $\hat{S}^z$ operator, then effectively rotation $\mathcal{R}_A$ amounts to flipping every second spin, e.g.:

$$\begin{aligned}\mathcal{R}_A|\downarrow\uparrow\downarrow\uparrow\downarrow\uparrow\ldots\rangle &= |\uparrow\uparrow\uparrow\uparrow\uparrow\uparrow\ldots\rangle,\\ \mathcal{R}_A|\uparrow\downarrow\uparrow\downarrow\uparrow\downarrow\ldots\rangle &= |\downarrow\downarrow\downarrow\downarrow\downarrow\downarrow\ldots\rangle,\end{aligned} \tag{1.11}$$

where $\uparrow$ ($\downarrow$) stands for the spin $s = \frac{1}{2}$ ($-\frac{1}{2}$) respectively. Rotation of the sublattice A has to be applied to all of the states in the basis leading to a new basis composed of rotated states.

Now once rotation has been performed, we can introduce the transformation to the magnon-holon basis. It consists of slave-fermion transformation combined with Holstein-Primakoff transformation for spin $s = \frac{1}{2}$,

$$\begin{aligned}
\hat{\tilde{c}}^{\dagger}_{i\uparrow} &= \hat{P}_i \hat{h}_i, & \hat{\tilde{c}}_{i\uparrow} &= \hat{h}^{\dagger}_i \hat{P}_i, \\
\hat{\tilde{c}}^{\dagger}_{i\downarrow} &= \hat{a}^{\dagger}_i \hat{P}_i \hat{h}_i, & \hat{\tilde{c}}_{i\downarrow} &= \hat{h}^{\dagger}_i \hat{P}_i \hat{a}_i, \\
\hat{S}^{+}_i &= \hat{h}_i \hat{h}^{\dagger}_i \hat{P}_i \hat{a}_i, & \hat{S}^{z}_i &= \left(\frac{1}{2} - \hat{a}^{\dagger}_i \hat{a}_i\right) \hat{h}_i \hat{h}^{\dagger}_i, \\
\hat{S}^{-}_i &= \hat{a}^{\dagger}_i \hat{P}_i \hat{h}_i \hat{h}^{\dagger}_i, & \hat{\tilde{n}}_i &= 1 - \hat{h}^{\dagger}_i \hat{h}_i = \hat{h}_i \hat{h}^{\dagger}_i.
\end{aligned} \tag{1.12}$$

Above, the operator $\hat{h}^{\dagger}_i$ creates a holon (spinless fermion) at site i, while $\hat{a}^{\dagger}_i$ creates a magnon at site i. The operator $\hat{P}_i = \sqrt{1 - \hat{a}^{\dagger}_i \hat{a}_i}$ is a projector with eigenvalue 1 if site i does not contain any magnon and eigenvalue 0 when it is occupied by one magnon. It makes sure one stays in a subspace of a Hilbert space with up to one magnon per site. Effectively, spin up ($\uparrow$) is mapped onto a vacuum for magnons and spin down ($\downarrow$) is mapped onto a single magnon. Moreover, $\hat{h}_i$ commutes with $\hat{a}_i$ (and thus with $\hat{P}_i$). Denoting the transformation to the magnon-holon basis as $\mathcal{M}$ we can for example write,

$$\begin{aligned}
\mathcal{M}\mathcal{R}_A|{\downarrow\uparrow} \circ {\uparrow\downarrow\uparrow} \ldots\rangle &= \mathcal{M}|{\uparrow\uparrow} \circ {\uparrow\uparrow\uparrow} \ldots\rangle = |\circ\bullet\circ\circ \ldots\rangle, \\
\mathcal{M}\mathcal{R}_A|{\uparrow\downarrow} \circ {\downarrow\uparrow\downarrow} \ldots\rangle &= \mathcal{M}|{\downarrow\downarrow} \circ {\downarrow\downarrow\downarrow} \ldots\rangle = |\bullet\bullet\bullet\bullet \ldots\rangle,
\end{aligned} \tag{1.13}$$

where $\circ$ represents empty site, $\bullet$ stands for the site occupied by a single magnon and $\bullet$ stands for the site occupied by a hole.

Following the slave-fermion transformation, it becomes clear that electron annihilation never leads to the creation of both the hole and the magnon in the same site. Thus each site can be in one of three states, either empty, occupied by a single magnon or occupied by a single hole. This exactly corresponds to the three states in the original formulation where each site could be either occupied by an electron with spin up or by an electron with spin down or be an empty site. Importantly, the proper commutation relations are fulfilled by the operators expressed in the magnon-holon basis (1.12) as long as we act on states within the physically relevant subspace where each site can be either empty, occupied by a single magnon or occupied by a single hole. Therefore, the introduced here transformation to magnon-holon basis is exact within this subspace.

1.5.2. Simplification of the projection operator

Before applying the above-described transformations to the model Hamiltonian, let us discuss the projection $\hat{P}_i$. The fact, that it contains a square root makes it rather unpleasing to deal with. It might be tempting to use a Taylor series expansion to get rid of the square root. But the power of this kind of expansion lies in the ability to capture the value and the derivatives around a single point. Since values of $\hat{a}^{\dagger}_i \hat{a}_i$ are discrete we do not care about any derivatives. At the same time, it would take an infinite number of terms in the Taylor series expansion to converge at the two values, 0 and 1, that we care about in the end. Thus instead of the Taylor series, it is better to use the Newton series expansion [66]. The latter gives the exact value at more than a single point with a finite number of terms. Incorporating this expansion, one can write,

$$\hat{P}_i = \sqrt{1 - \hat{a}^{\dagger}_i \hat{a}_i} = 1 - \hat{a}^{\dagger}_i \hat{a}_i + O\left((\hat{a}^{\dagger}_i \hat{a}_i)^2\right), \tag{1.14}$$

where for the physically relevant subspace of 0 or 1 magnon per site, the equality becomes,

$$\hat{P}_i = 1 - \hat{a}_i^\dagger \hat{a}_i, \tag{1.15}$$

allowing us to omit all the square roots in the introduced transformations.

1.5.3. Hamiltonian of the t–J model in the magnon-holon basis

Altogether, one can apply the transformation to the magnon-holon basis (of Sec. 1.5.1) to obtain the t–J Hamiltonian in the polaronic language,

$$\hat{\mathcal{H}}_{t\text{–}J} = \hat{\mathcal{H}}_t + \hat{\mathcal{H}}_{xy} + \hat{\mathcal{H}}_z, \tag{1.16}$$

where

$$\hat{\mathcal{H}}_t = t \sum_{\langle i,j \rangle} \hat{P}_i \left(\hat{h}_i^\dagger \hat{h}_j \hat{a}_i + \hat{h}_i^\dagger \hat{h}_j \hat{a}_j^\dagger \right) \hat{P}_j + \text{H.c.}, \tag{1.17}$$

$$\hat{\mathcal{H}}_{xy} = \frac{J}{2} \sum_{\langle i,j \rangle} \hat{h}_i \hat{h}_i^\dagger \left(\hat{P}_i \hat{P}_j \hat{a}_i \hat{a}_j + \text{H.c.} \right) \hat{h}_j \hat{h}_j^\dagger, \tag{1.18}$$

$$\hat{\mathcal{H}}_z = \frac{J}{2} \sum_{\langle i,j \rangle} \hat{h}_i \hat{h}_i^\dagger \left(\hat{a}_i^\dagger \hat{a}_i + \hat{a}_j^\dagger \hat{a}_j - 2 \hat{a}_i^\dagger \hat{a}_i \hat{a}_j^\dagger \hat{a}_j - 1 \right) \hat{h}_j \hat{h}_j^\dagger. \tag{1.19}$$

In the polaronic description, the t–J Hamiltonian consists of three parts. The $\hat{\mathcal{H}}_t$ represents the polaronic coupling between the hole and magnetic degrees of freedom in the system. The moving hole will either excite or annihilate magnons along its path. The $\hat{\mathcal{H}}_{xy}$ represents spin flips which are now translated to the creation and annihilation of pairs of magnons on neighboring sites. The $\hat{\mathcal{H}}_z$ originates from Ising interaction between spins and is now translated to the energetic cost of having magnons in the system and energetic gain from the attractive interaction between neighboring magnons.

1.6. Beyond the t–J model: scalable magnon-magnon interactions

The focus of this work is to a great extent directed at studying and understanding how the magnon-magnon interactions affect the physics of a hole in a Mott insulator (see Sec. 1.4.3). This is achieved by going beyond the t–J model and introducing the scaling parameter λ for the magnon-magnon interaction,

$$\hat{a}_i^\dagger \hat{a}_i \hat{a}_j^\dagger \hat{a}_j \to \lambda \hat{a}_i^\dagger \hat{a}_i \hat{a}_j^\dagger \hat{a}_j. \tag{1.20}$$

This affects only the diagonal terms $\hat{\mathcal{H}}_z$ of the t–J Hamiltonian (1.16),

$$\hat{\mathcal{H}}_z(\lambda) = \frac{J}{2} \sum_{\langle i,j \rangle} \hat{h}_i \hat{h}_i^\dagger \left(\hat{a}_i^\dagger \hat{a}_i + \hat{a}_j^\dagger \hat{a}_j - 2\lambda \hat{a}_i^\dagger \hat{a}_i \hat{a}_j^\dagger \hat{a}_j - 1 \right) \hat{h}_j \hat{h}_j^\dagger, \tag{1.21}$$

Altogether, we obtain the t–J model with scalable magnon-magnon interactions,

$$\hat{\mathcal{H}}_{t\text{–}J}(\lambda) = \hat{\mathcal{H}}_t + \hat{\mathcal{H}}_{xy} + \hat{\mathcal{H}}_z(\lambda). \tag{1.22}$$

Note that for $\lambda = 1$ the above Eq. (1.22) yields the same Hamiltonian as $\hat{\mathcal{H}}_{t\text{–}J}$ given in Eq. (1.16).

1.6.1. Scaling magnon-magnon interactions in a spin language

One may wonder how the scaling of the magnon-magnon interaction can be introduced through the spin operators. It is not only perfectly valid but also a reasonable question to ask. It allows for gaining some of the initial intuition about the role of those interactions. Reversing the transformations to polaronic language, one obtains,

$$\hat{a}_i^\dagger \hat{a}_i \hat{a}_j^\dagger \hat{a}_j = -\hat{S}_i^z \hat{S}_j^z + \frac{1}{4}\hat{\tilde{n}}_i \hat{\tilde{n}}_j - \frac{1}{2}\left(\xi_i \hat{S}_i^z \ + \xi_j \hat{S}_j^z\right) \hat{\tilde{n}}_i \hat{\tilde{n}}_j, \tag{1.23}$$

where the value of $\xi_i \in \{-1, 1\}$ is dependent on whether i belongs to the sublattice that has been rotated or not (the choice of the sign is arbitrary). Eventually, $\hat{\mathcal{H}}_z(\lambda)$ part of the Hamiltonian with scalable magnon-magnon interactions (1.22) reads,

$$\hat{H}_z(\lambda) = J \sum_{\langle i,j \rangle} \left\{ \hat{\mathbf{S}}_i \hat{\mathbf{S}}_j - \frac{1}{4}\hat{\tilde{n}}_i \hat{\tilde{n}}_j + (\lambda - 1)\left[\hat{S}_i^z \hat{S}_j^z - \frac{1}{4}\hat{\tilde{n}}_i \hat{\tilde{n}}_j + \frac{1}{2}\left(\xi_i \hat{S}_i^z \ + \xi_j \hat{S}_j^z\right) \hat{\tilde{n}}_i \hat{\tilde{n}}_j \right] \right\}. \tag{1.24}$$

The notable thing about the above equation is the appearance of the staggered magnetic field term $\xi_i \hat{S}_i^z \ + \xi_j \hat{S}_j^z$. This term can be connected to the effective staggered field in the *quasi*-1D cuprates coming from the small interchain coupling (see Sec. 5.3). Later, it will be shown this has important consequences for the interpretation of the experiments on real materials.

1.7. Beyond the t–J model: t–J^z model

A strongly anisotropic limit of the t–J model, where only z component of neighboring spins may interact, is also an interesting and insightful model to study [55, 67–70]. This Ising limit of the t–J model is called a t–J^z model. Its Hamiltonian in magnon-holon basis (1.12) is given by

$$\hat{\mathcal{H}}_{t\text{–}J^z} = \hat{\mathcal{H}}_t + \hat{\mathcal{H}}_z, \tag{1.25}$$

with $\hat{\mathcal{H}}_t$ and $\hat{\mathcal{H}}_z$ given in Eq. (1.17) and Eq. (1.19) respectively. A lack of spin fluctuations [no $\hat{\mathcal{H}}_{xy}$ given by Eq. (1.18)] in this model makes it much easier to study both in 1D and 2D than the t–J model of Eq. (1.16). We can also extend this model by introducing scalable magnon-magnon interactions,

$$\hat{\mathcal{H}}_{t\text{–}J^z}(\lambda) = \hat{\mathcal{H}}_t + \hat{\mathcal{H}}_z(\lambda), \tag{1.26}$$

with $\hat{\mathcal{H}}_z(\lambda)$ given in Eq. (1.21). Investigating the t–J^z model using the same polaronic description for 1D and 2D could give us some initial intuition and possibly shine some light on the problem of a single hole in an antiferromagnet and on the role the magnon-magnon interactions play in the formation of the spin polaron.

The t–J^z model with a single hole in an otherwise half-filled band was previously studied both in 1D and on the 2D square lattice. In both cases, the ground state without the hole is simply an Ising antiferromagnet. But similarly to the t–J model, the understanding of a single hole depends on the dimension one considers. In 1D, the introduced hole may propagate through the lattice creating a single pair of ferromagnetically aligned spins [cf. Fig. 1.2.(a-c)]. But due to the lack of spin fluctuations this magnetic excitation is immobile. The spectral function $A(k, \omega)$ becomes momentum independent. It can be calculated analytically to find out that it consists of a delta-like

peak at the single-hole ground state energy split from an incoherent spectrum formed by the excited states of the system [71]. This differs from the 1D t–J model case, where only a continuum of states exists. Despite the differences, the t–J^z model is typically also understood as a system exhibiting spin-charge separation, as apart from the first move, the hole does not spoil the antiferromagnetic order in the system.

When we move to 2D, then each time the hole moves away from the position where it was created, a magnon is excited. The lack of spin fluctuations then leaves the hole subject to a linear-like discrete potential. This in return renders the hole localized in space [52]. The presence of the linear-like potential gives rise to the spectral function consisting of a set of delta-like peaks [72] with the gaps between the peaks scaling proportional to $(J/t)^{2/3}$. The power of $2/3$ is reminiscent of the linear potential growth as in the problem of a single particle in the triangular quantum well. On top of the ladder-like spectrum, the hole motion in a loop may liberate the hole from the linear potential growth. But from the exact diagonalization studies, it seems that the effect on the ground state is negligible. Altogether, the hole in the 2D t–J^z model is understood in terms of a rather immobile spin polaron. This stays in contrast to the dispersive spin polaron of the 2D case.

1.8. Goals and plan of this thesis

The main goal of this thesis is to resolve issues presented in Sec. 1.4. This includes studies of similarities and differences in the spectral properties of the hole introduced to 1D and 2D antiferromagnet (Sec. 1.4.1); revealing to what degree the spin-charge separation versus spin polaron is a proper description of the low energy physics of the *quasi*-1D cuprates (Sec. 1.4.2); and finally answering the question about the role of the magnon-magnon interactions in the formation of the spin polaron in an antiferromagnet with a single hole (Sec. 1.4.3). To this end, the spectral properties of the single hole introduced to an antiferromagnet are studied in great detail, especially for the t–J^z model on the 2D square lattice for which a detailed understanding of new classes of states, not discussed in previous works, is going to be provided as well.

The above issues are resolved by using the magnon-holon basis (Sec. 1.5.1). This allows us to describe the t–J Hamiltonian (Sec. 1.6) and the t–J^z Hamiltonian (Sec. 1.7) (with scalable magnon-magnon interactions) in the same language for all bipartite lattices.

Structure of the thesis:

The thesis is composed of 6 chapters: Introduction, 4 main chapters and Summary.

Chapter 1. **Introduction.** Provides introductory information about the problem of a single hole in the t–J and the t–J^z models, states the main goal of the thesis and paints a general approach to the problem.

Chapter 2. **The t–J^z model on the Bethe lattice.** Discusses the t–J^z model on the Bethe lattice with coordination $z = 2$ (1D) and $z = 4$. Spectral and ground state properties of the single hole in the t–J^z model on these two lattices are studied in magnon-holon basis. Results are discussed in connection to the cold atoms experiments on the Hubbard model.

Chapter 3. **The t–J^z model on the 2D square lattice.** Discusses the t–J^z model on the 2D square lattice. Spectral properties of the single hole in the t–J^z model are studied in magnon-holon basis. A special technique for calculating the spectral function is introduced. The importance of the magnon-magnon interactions for the proper description of the excited states in 2D is discussed.

Chapter 4. **Beyond vibrational modes in the 2D t–J^z model.** Discusses a new class of states in the t–J^z model not covered in the previous chapters. A special method of calculating the spectral properties of a single hole with non-zero angular momentum is described. A new class of so-called rotational states is introduced and their features are explained through intuitive pictures and analytical derivations.

Chapter 5. **The 1D t–J model** Discusses the t–J model on a chain. Spectral and ground state properties of the single hole are studied numerically using exact diagonalization. The role of magnon-magnon interactions is analyzed from the perspective of the robustness of the spin polaron physics in the t–J model. Detailed finite-size scalings for the quasiparticle weight and energy gap are presented. An explicit connection of the scaled magnon-magnon interactions to the physics of the *quasi*-1D cuprates is provided.

Chapter 6. **Summary.** Summarizes the new insights to the problem of a single hole in the t–J and the t–J^z models. The common knowledge about discussed models is contrasted with the main findings of this thesis.

Additionally, each main chapter is provided with a Conclusions section summarizing the main results of that chapter.

Chapter 2

The t–J^z model on the Bethe lattice

Based on Krzysztof Bieniasz, Piotr Wrzosek, Andrzej M. Oleś, Krzysztof Wohlfeld, SciPost Physics **7** *(5), 066 (2019).*

The t–J model on a square lattice and the same model on a chain are reasonable choices to study low energy physics of lightly doped cuprates (see Sec. 1.1). Moreover, some materials [73, 74] exhibit anisotropy of spin interactions which makes the Ising limit of the t–J model also an interesting candidate to study. Finally, the Ising limit of the t–J model is a simpler model to study and therefore constitutes a good starting point for this thesis, see also Sec. 1.7. Thus in this chapter, we will focus on this Ising limit of the t–J model (the so-called t–J^z model) given by the Hamiltonian (1.25) defined specifically on the Bethe lattice.

The Bethe lattice is an infinite tree—connected undirected acyclic graph characterized by the coordination number z. This coordination number defines how many edges are attached to each node of the tree. Therefore, it tells how many nearest neighbors there are for each site of the lattice. The cases of $z = 0$ and $z = 1$ describe a single site and a pair of sites respectively. The smallest z that is of our interest is $z = 2$, as it stands for a chain. The other most interesting case is $z = 4$ since it is the closest cousin of the square lattice in 2D, which also has a coordination of 4. The important difference between the Bethe lattice with $z = 4$ and the 2D square lattice is the lack of closed loops in the Bethe lattice. For the latter reason, many results concerning the t–J^z model on the Bethe lattice can be calculated analytically.

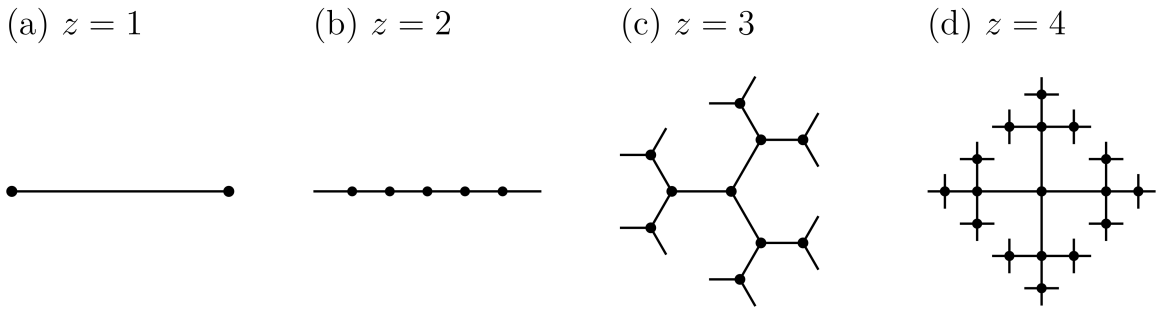

Figure 2.1: Fragments of the Bethe lattice for various coordination numbers: (a) $z = 1$, (b) $z = 2$, (c) $z = 3$, (d) $z = 4$. For $z > 1$ the lattice extends to infinity.

To obtain a better insight into the differences and similarities between the 1D and 2D t–J physics (see Sec. 1.4.1) as well as into the role of the magnon-magnon interactions in the formation of the spin polaron (see Sec. 1.4.3) we extend the model

Hamiltonian (1.25) by introducing the magnon-magnon interactions scaling λ. The resulting model is thus given by the Eq. (1.26). Let us remember that $\lambda = 1$ yields the exact transformation, while $\lambda \neq 1$ goes beyond the t–J^z model. Moreover, the lack of spin flips means magnons are immobile and can only be created or annihilated by the moving hole. Finally, considering the t–J^z model on the Bethe lattice will constitute a good introduction for later studies of the so-called rotational degrees of freedom in the t–J^z model, see Ch. 4.

Before we introduce the hole to the system it is important to understand the undoped (one electron per site) ground state. The ground state of the t–J^z Hamiltonian (1.26) with $\lambda = 1$ and $J > 0$ is an Ising antiferromagnet and it does not depend on the coordination z. The ground state subspace is doubly degenerate. The natural choice of basis for this subspace consists of two states that have neighboring spins aligned antiparallel, i.e. every second spin is pointing *up* and every other spin is pointing *down*. On the infinite lattice (or lattice with periodic boundary conditions), given one of those states, the other one can be obtained by translating all the electrons (spins) by one site. In the polaronic language, those two states correspond to a vacuum state for holes and magnons $|\varnothing\rangle$ and a state fully occupied by magnons (but vacuum for holes) $|\Omega\rangle$. The degeneracy between $|\varnothing\rangle$ and $|\Omega\rangle$ is lifted for any $\lambda \neq 1$. It is straightforward to notice that for $\lambda = 0$ state $|\Omega\rangle$ has the highest energy. On the other hand, the same state becomes the ground state for $\lambda > 1$. Yet for the physically relevant cases of $\lambda \leq 1$ the ground state is $|\varnothing\rangle$ (note that $|\Omega\rangle$ is also the ground state if $\lambda = 1$, but when calculating the observables in this case it does not matter which one we choose).

2.1. The t–J^z model on a chain ($z = 2$)

2.1.1. General formula for the spectral function

Let us start with the simplest and unique case of the t–J^z model in one dimension (i.e. Bethe lattice with $z = 2$). In particular, we want to investigate the spectral function of a single hole (1.2) in one dimension both in the absence ($\lambda = 0$) and presence ($\lambda = 1$) of the magnon-magnon interactions. In both cases, the ground state is the vacuum state for holes and magnons $|\varnothing\rangle$. When the hole is introduced to a site i then the resulting state can be denoted as $|i, i\rangle = \hat{h}_i^\dagger|\varnothing\rangle$. The first index stands for the position where the hole has been originally introduced, while the second one denotes the actual position of the hole. In general, state $|i, j\rangle$ contains $|i - j|$ magnons connecting the site i with the site j occupied by the hole. This does not cover the whole Hilbert space of the model in one dimension, since the assumption here is that the hole has been created in a vacuum state—there are no magnons before the hole is introduced. At the same time, such states allow expressing $\hat{\mathcal{H}}_{t\text{–}J^z}^n \hat{h}_i^\dagger|\varnothing\rangle$ for any non-negative integer n. And this is enough to cover all the states contributing to the spectral function of our interest.

One can observe,

$$\hat{\mathcal{H}}_t|i, j\rangle = -t\left(|i, j-1\rangle + |i, j+1\rangle\right), \tag{2.1}$$

while the translation operator would produce,

$$\hat{T}|i, j\rangle = |i+1, j+1\rangle. \tag{2.2}$$

For an infinite lattice, the first index is never affected by the Hamiltonian (1.26), thus acting with $\hat{\mathcal{H}}_t$ (or $\hat{\mathcal{H}}_{t\text{–}J^z}(\lambda)$) repeatedly can never result in a translation. For this

reason, the spectral function is momentum-independent. Thus in what follows, we will focus on the local spectral function of a single hole. Therefore, we are looking for the following expression,

$$A(\omega) = -\frac{1}{\pi} \lim_{\delta \to 0^+} \mathrm{Im}\, G(\omega + i\delta), \tag{2.3}$$

where

$$G(\omega) = \langle \varnothing | \hat{h}_i \left(\omega - \hat{\mathcal{H}}_{t\text{–}J^z}(\lambda) + E_\varnothing \right)^{-1} \hat{h}_i^\dagger | \varnothing \rangle. \tag{2.4}$$

The result does not depend on the site i where the hole is introduced, thus this index is skipped on the left-hand side of the equation. The analytical solution to the above problem has been presented in previous works [72], but for completeness let us present the solution in detail below. This way we will set a convenient starting point for further generalizations to the Bethe lattice with $z > 2$ (Sec. 2.2), self-avoiding walks approximation on the square lattice (Ch. 3) and the spectral functions with rotational degrees of freedom (Ch. 4).

The solution to the above problem can be divided into a few steps. First, we choose basis $\mathcal{B}$ for the subspace of states contributing to the spectral function. Second, we write the matrix of the Hamiltonian within that subspace. Finally, we find the recursive formula for the diagonal coefficient of the inverse of $\omega - \hat{\mathcal{H}}_{t\text{–}J^z}(\lambda) + E_\varnothing$. The position of this coefficient has to coincide with the position of the initial state $|i, i\rangle$ in basis $\mathcal{B}$.

We start with defining basis $\mathcal{B}$. Without loss of generality we can set site index $i = 0$ since Green's function $G(\omega)$ is site i independent. We introduce the following notation,

$$|0\rangle = |0, 0\rangle, \tag{2.5}$$

$$|n\rangle = \frac{1}{\sqrt{2}} \left(|0, n\rangle + |0, -n\rangle \right), \tag{2.6}$$

$$|-n\rangle = \frac{1}{\sqrt{2}} \left(|0, n\rangle - |0, -n\rangle \right), \tag{2.7}$$

where $n \in \mathbb{N}_+$. With the above, we can define,

$$\mathcal{B} = \left(|0\rangle, |1\rangle, |2\rangle, ..., |-1\rangle, |-2\rangle, ... \right). \tag{2.8}$$

The matrix of the Hamiltonian $\hat{\mathcal{H}}_{t\text{–}J^z}(\lambda)$ [Eq. (1.26)] is tridiagonal when written in basis $\mathcal{B}$ and it consists of two blocks,

$$M_{\mathcal{B}}^{\mathcal{B}}(\hat{\mathcal{H}}_{t\text{–}J^z}(\lambda) - E_\varnothing) = \left[\begin{array}{ccccc|ccccc} V_0 & t\sqrt{2} & & & & & & & & \\ t\sqrt{2} & V_1 & t & & & & & & & \\ & t & V_2 & t & & & & 0 & & \\ & & t & V_3 & \ddots & & & & & \\ & & & \ddots & \ddots & & & & & \\ \hline & & & & & V_1 & t & & & \\ & & & 0 & & t & V_2 & t & & \\ & & & & & & t & V_3 & \ddots & \\ & & & & & & & \ddots & \ddots & \end{array}\right], \tag{2.9}$$

where $V_n = \langle n|(\hat{\mathcal{H}}_{t\text{–}J^z}(\lambda) - E_\varnothing)|n\rangle$. Only states $|n\rangle$, where $n \in \mathbb{N} \cup \{0\}$, contribute to $G(\omega)$. This is due to the fact that the inverse of a block-diagonal matrix is a block-diagonal matrix of inverses of the diagonal blocks. Denoting $\mathcal{B}_+ = (|0\rangle, |1\rangle, |2\rangle, \dots)$, we can write down the matrix of the Hamiltonian for the minimal subspace of our interest,

$$M^{\mathcal{B}_+}_{\mathcal{B}_+}(\hat{\mathcal{H}}_{t\text{–}J^z}(\lambda) - E_\varnothing) = \begin{bmatrix} V_0 & t\sqrt{2} & & & \\ t\sqrt{2} & V_1 & t & & \\ & t & V_2 & t & \\ & & t & V_3 & \ddots \\ & & & \ddots & \ddots \end{bmatrix}. \tag{2.10}$$

With the last step, we will find the expression for the Green's function $G(\omega)$. All we have to do is to find the top left coefficient of the inverse of

$$M_0 \equiv M^{\mathcal{B}_+}_{\mathcal{B}_+}(\omega - \hat{\mathcal{H}}_{t\text{–}J^z}(\lambda) + E_\varnothing) = \left[\begin{array}{c|c} \omega - V_0 & B_1^T \\ \hline B_1 & M_1 \end{array}\right], \tag{2.11}$$

where M_i stands for submatrix of $M(\omega - \hat{\mathcal{H}}_{t\text{–}J^z}(\lambda) + E_\varnothing)^{\mathcal{B}_+}_{\mathcal{B}_+}$ without first i rows and columns and B_i is a one-column matrix with all the coefficient equal to 0 but the very first one, which we denote as $b_1^{(i)}$. Thus we have,

$$\left[M_0^{-1}\right]_{1,1} = \left(\omega - V_0 - B_1^T M_1^{-1} B_1\right)^{-1}. \tag{2.12}$$

Since $B_i^T M_i^{-1} B_i = (b_1^{(i)})^2 [M_i^{-1}]_{1,1}$, the generic formula for the Green's function can be written in the form of a continued fraction,

$$G(\omega) = \cfrac{1}{\omega - V_0 - \cfrac{2t^2}{\omega - V_1 - \cfrac{t^2}{\omega - V_2 - \dots}}}. \tag{2.13}$$

2.1.2. Spectral function without magnon-magnon interactions

In the previous section, we derived the generic formula (2.13) for the Green's function of a single hole added to the 1D t–J^z chain in the half-filled limit. In this section, we will have a close look at the results for the spectral function where the magnon-magnon interactions are neglected, i.e. when $\lambda = 0$. This is the easiest case since the terms quartic in bosonic operators a are absent [see Eq. (1.26)]. The important implication of $\lambda = 0$ is that hole feels almost linearly growing potential from created magnons when moving away from the site where the hole has been introduced. In this case, the coefficients V_n in Eq. (2.13) are given by,

$$V_0 = J, \tag{2.14}$$

$$V_{n>0} = \left(n + \frac{1}{2}\right) J. \tag{2.15}$$

This allows expressing the Green's function given by Eq. (2.13) through a ratio of the Bessel functions of the first kind [75] [denoted here as $\mathcal{J}_\alpha(x)$],

$$G(\omega)^{-1} = \omega - J + 2t\frac{\mathcal{J}_{\frac{1}{2}-\frac{\omega}{J}}(\frac{2t}{J})}{\mathcal{J}_{\frac{3}{2}-\frac{\omega}{J}}(\frac{2t}{J})}. \tag{2.16}$$

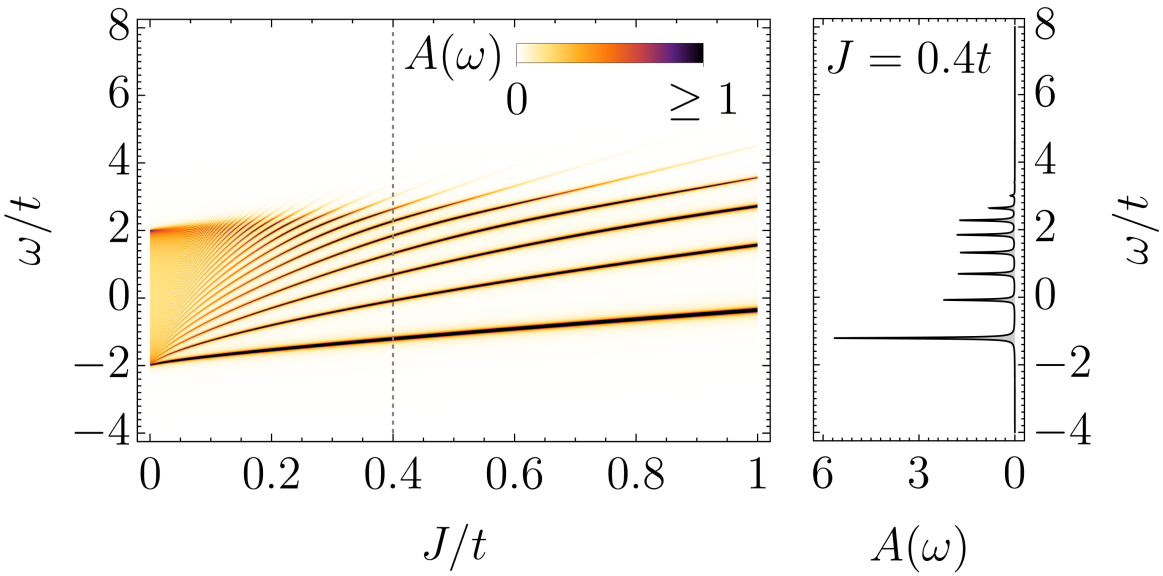

Figure 2.2: Left panel: spectral function $A(\omega)$ of a single hole created in the Ising antiferromagnet without magnon-magnon interactions ($\lambda = 0$) for values of $J/t \in [0, 1]$. Right panel: the shape of the spectral function at $J/t = 0.4$ (denoted by the dashed line in the left panel). The spectrum consists of a set of well-separated quasiparticle-like peaks for all values of coupling constant $J > 0$. For $J = 0$ peaks merge into a U-shaped continuum.

The corresponding spectral function $A(\omega)$ is shown in Fig. 2.2. The density plot in the left panel of Fig. 2.2 shows how the spectral function evolves when J/t changes. The cut through $J = 0.4t$ in the right panel of the same figure presents its actual shape for this particular value of J. The most important feature of the spectral function without the magnon-magnon interaction is the onset of quasiparticle-like well-separated peaks visible for all the finite values of the coupling constant $J > 0$. As shown in the previous studies [52, 69], the separation between the peaks scales as $(J/t)^{2/3}$. This can be simply understood. Such scaling between the energy levels naturally appears for the problem of a single particle in the triangular (or V-shaped) well. Since $V_{n>0}$ are linear in n we encounter here a similar problem, only the potential is not continuous but it changes discretely. When $J \to 0_+$ all the peaks appear at infinitesimally close distances and they merge into a U-shaped continuum centered around $\omega = 0$.

2.1.3. Exact spectral function

Although interesting, the case of $\lambda = 0$ is quite artificial for the t–J^z model on a chain. At the same time, incorporating interactions in strongly correlated systems is often a challenging task. But the t–J^z model seems to be an interesting exception to this rule, at least when it comes to calculating the spectral function of a single hole. It is enough

to notice that the ground state does not contain magnons before the hole is injected into the system. This way the only magnons that appear in the system have to be created by the moving hole. This is exactly what states $|i, j\rangle$ defined at the beginning of Sec. 2.1 are supposed to accomplish—they cover a subspace of the Hilbert space where magnons form a chain attached to the hole.

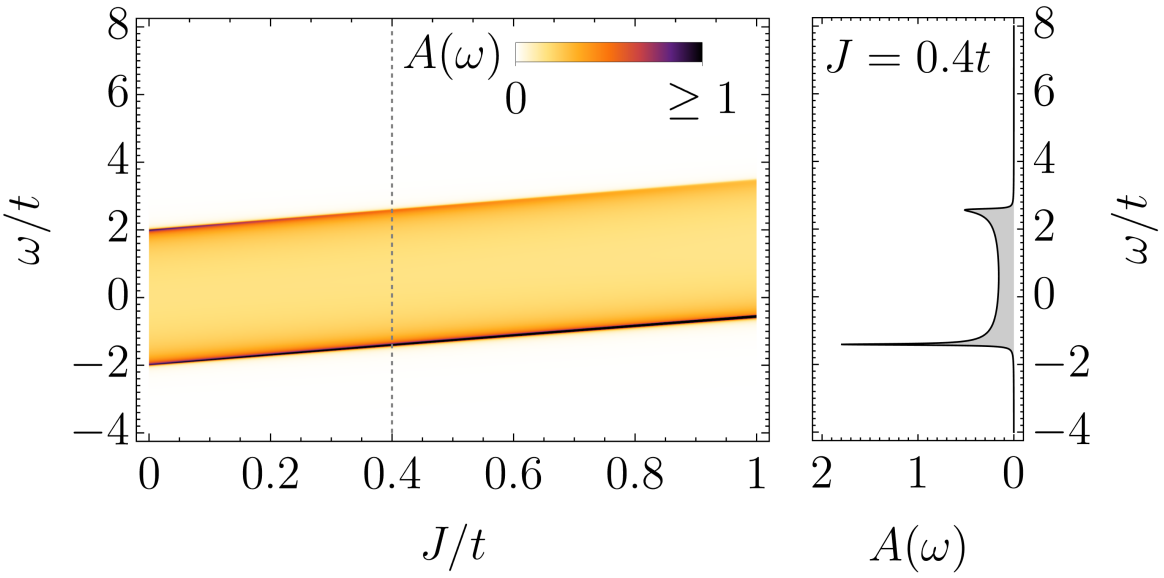

Figure 2.3: Left panel: exact ($\lambda = 1$) spectral function $A(\omega)$ of a single hole created in the Ising antiferromagnet on a chain for values of $J/t \in [0, 1]$. Right panel: the shape of the spectral function at $J/t = 0.4$ (denoted by the dashed line in the left panel). The spectrum consists of a single quasiparticle-like peak and the continuum of states above for all values of coupling constant $J > 0$. For $J = 0$ peak merges with the U-shaped continuum. The peak seems to be attached to the continuum for larger J due to broadening $\delta = 0.02t$.

When $\lambda = 1$ the cost of each magnon beyond the first one is exactly compensated by the magnon-magnon interaction with its neighbor. We will discuss it in more detail in Sec. 2.3. Effectively only the first created magnon cost energy of $\frac{J}{2}$ and other magnons are created for free. The coefficients V_n are thus given by,

$$V_0 = J, \tag{2.17}$$

$$V_{n>0} = \frac{3J}{2}, \tag{2.18}$$

and the Green's function can be written in a closed form as,

$$G(\omega)^{-1} = \frac{J}{2} \pm \sqrt{\left(\omega - \frac{3J}{2}\right)^2 - 4t^2}, \tag{2.19}$$

where the sign $\pm$ in front of the square root depends on the value of ω. It is negative $(-)$ for $\omega < \frac{3J}{2}$ and positive $(+)$ otherwise. This time the hole feels just a point potential from a single lattice site compared to the linearly growing potential for $\lambda = 0$ case presented before. This has important consequences for the shape of the spectral function, as one can observe in Fig. 2.3. Unlike in the case of no magnon-magnon

interactions ($\lambda = 0$), the exact spectral function including magnon-magnon interactions ($\lambda = 1$) cannot be described as a ladder spectrum. On the contrary, it consists of a single quasiparticle peak and a continuum of states above the peak. The key result here is that the magnon-magnon interactions are the crucial driving source of the collapse of the ladder spectrum.

In the end, let us formally describe the above-mentioned features of the spectral function. From the expression for the Green's function given in Eq. (2.19), one can easily find the solution for the position ω^* of the quasiparticle peak,

$$G(\omega^*)^{-1} = 0 \Leftrightarrow \omega^* = \frac{3J}{2} - \frac{1}{2}\sqrt{J^2 + 16t^2}. \tag{2.20}$$

When the expression under the square root in the formula for the Green's function is negative, the continuum of states appears. The region it covers is thus given by,

$$\left|\omega - \frac{3J}{2}\right| \leq 2t. \tag{2.21}$$

The bottom edge of the continuum is given by $\omega = \frac{3J}{2} - 2t$. Therefore the only point where ω^* touches the continuum is for $J = 0$, while for $J > 0$ the peak remains separated from the continuum. Nevertheless, for $J < t$ the mentioned separation is rather small compared to the width of the continuum. For this reason, one cannot clearly see the peak in Fig. 2.3 even with a relatively small broadening $\delta = 0.02t$.

2.2. The t–J^z model on a tree ($z > 2$)

In the previous sections, we discussed a spectral function of a single hole [Eq. (2.3)] in an antiferromagnetic chain [i.e. Bethe lattice with $z = 2$] with a Hamiltonian given by the t–J^z model. We will now generalize the used approach to include Bethe lattices with coordination $z > 2$. We start with the basis for the relevant subspace of states contributing to the spectral function. The spectral function is calculated for the initial state $|0\rangle = \hat{h}_i^\dagger|\varnothing\rangle$ denoting the hole introduced to the vacuum state at a certain site (it does not matter where; see discussion around Eq. (2.3)). Let us introduce the following notation,

$$|n; d_1, d_2, \ldots, d_n\rangle, \tag{2.22}$$

for the state with n magnons in a chain, where the hole has been propagated through bonds in directions $d_1, d_2, \ldots, d_n$ in the given order from the site where the hole has been introduced. Acting with the Hamiltonian (1.26) on such states we obtain,

$$\hat{\mathcal{H}}_{t\text{–}J^z}(\lambda)|0\rangle = E_0|0\rangle - t\sum_{d_1=0}^{z-1}|1; d_1\rangle, \tag{2.23}$$

while for $n > 0$ the result is,

$$\begin{aligned}\hat{\mathcal{H}}_{t\text{–}J^z}(\lambda)|n; d_1, d_2, \ldots, d_n\rangle = {} & E_n|n; d_1, d_2, \ldots, d_n\rangle \\ & - t|n-1; d_1, d_2, \ldots, d_{n-1}\rangle \\ & - t\sum_{d_{n+1}=0}^{z-2}|n+1; d_1, d_2, \ldots, d_n, d_{n+1}\rangle.\end{aligned} \tag{2.24}$$

One can notice two things about the above equation. First, the diagonal terms depend on the length of the chain of magnons but not on its shape. This comes from the fact that the Bethe lattice is a tree, therefore there are no loops and the chain of magnons cannot interact with itself—it is effectively a one-dimensional object. Second, the hopping term does not depend on the direction in which the hole moves, thus all the states with the same number of magnons appear with the same coefficient. This means the relevant subspace for calculating the spectral function can be described as follows,

$$|0\rangle = \hat{h}_i^\dagger|\varnothing\rangle, \tag{2.25}$$

$$|n\rangle = \frac{1}{\sqrt{z(z-1)^{n-1}}} \sum_{d_1=0}^{z-1} \sum_{d_2=0}^{z-2} \cdots \sum_{d_n=0}^{z-2} |n; d_1, d_2, ..., d_n\rangle \quad \text{for } n > 0. \tag{2.26}$$

where noticeably in the above sum all the phase factors in front of $|n; d_1, d_2, ..., d_n\rangle$ are equal to 1. Thus state $|n\rangle$ represents the normalized sum of all states where the hole was propagated n times without returning from site i where it was introduced. This corresponds to the so-called vibrational modes of the hole which cover the subspace contributing to the spectral function of our interest. In contrast, discussed in Ch. 4 rotational modes may incorporate phase factors that are complex roots of 1 and thus cover larger subspace, i.e. equal to the one given by $|n; d_1, d_2, ..., d_n\rangle$. But those states cannot be measured by standard ARPES technique.

Defining the basis $\mathcal{B} = (|0\rangle, |1\rangle, |2\rangle, \dots)$, we proceed to write down the matrix of the Hamiltonian (1.26),

$$M_{\mathcal{B}}^{\mathcal{B}}(\hat{\mathcal{H}}_{t\text{-}J^z}(\lambda) - E_\varnothing) = \begin{bmatrix} V_0 & t\sqrt{z} & & & \\ t\sqrt{z} & V_1 & t\sqrt{z-1} & & \\ & t\sqrt{z-1} & V_2 & t\sqrt{z-1} & \\ & & t\sqrt{z-1} & V_3 & \ddots \\ & & & \ddots & \ddots \end{bmatrix}. \tag{2.27}$$

As one can notice, the above generalization includes also the specific case of $z = 2$ [cf. Eq. (2.10)]. Following the same steps of calculating the Green's function as for $z = 2$, we arrive at the general result,

$$G(\omega) = \cfrac{1}{\omega - V_0 - \cfrac{zt^2}{\omega - V_1 - \cfrac{(z-1)t^2}{\omega - V_2 - \dots}}}. \tag{2.28}$$

Let us remember that in the considered basis $\mathcal{B}$ magnons always form a chain connecting site i where the hole was introduced with the current position of the hole n sites away from i. This together with the fact that Bethe lattice is a tree allows calculating the excitation energies V_n without troubles. A hole or a magnon costs $\frac{zJ}{2}$, i.e. $\frac{J}{2}$ for each bond. The cost of a magnon located next to a hole is reduced by $\frac{J}{2}$. And for each pair of neighboring magnons, the energy is reduced by λJ. Thus the

excitation energies can be written as follows,

$$V_0 = \frac{zJ}{2}, \tag{2.29}$$

$$V_{n>0} = [2z - 1 + (z - 2\lambda)(n - 1)]\,\frac{J}{2}. \tag{2.30}$$

Combining Eqs. (2.28)-(2.30), the Green's function for $z > 2$ can also be expressed through a ratio of the Bessel functions of the first kind. Then it reads,

$$G(\omega)^{-1} = \omega - \frac{zJ}{2} + \frac{zt}{\sqrt{z-1}}\frac{\mathcal{J}_{\Omega(\omega)}(2\xi)}{\mathcal{J}_{\Omega(\omega)-1}(2\xi)}, \tag{2.31}$$

where

$$\Omega(\omega) = \frac{2z - 1 - \frac{2\omega}{J}}{z - 2\lambda} \quad \text{and} \quad \xi = \frac{2t\sqrt{z-1}}{(z-2\lambda)J}. \tag{2.32}$$

In general, the above-defined formula works as long as $z \neq 2\lambda$, i.e. as long as $V_{n>0}$ depends linearly on n. For $z = 2\lambda$ all $V_{n>0}$ are equal and the expression for the Green's function simplifies to a quadratic relation, as in the case of $z = 2$ and $\lambda = 1$ discussed in the previous section.

2.2.1. Spectral function without magnon-magnon interactions

Now let us analyze the spectral properties of a single hole in the t–J^z model on the Bethe lattice with coordination $z = 4$. We start with the case neglecting the magnon-magnon interactions ($\lambda = 0$). The result shown in Fig. 2.4 is qualitatively the same as the corresponding result for $z = 2$ (cf. Fig. 2.2). The spectrum consists of a set

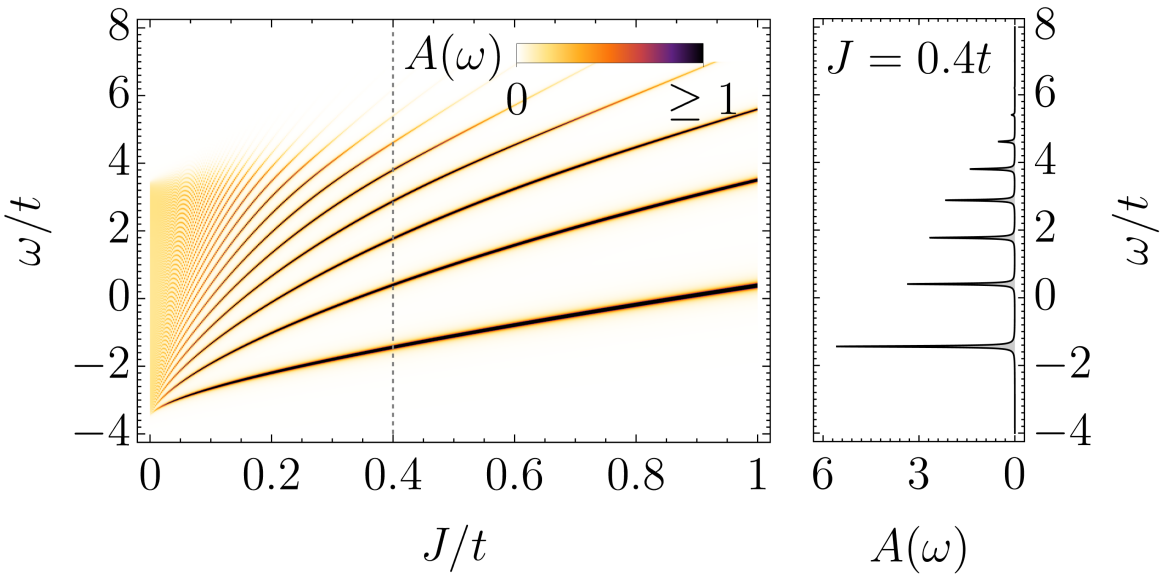

Figure 2.4: Left panel: spectral function $A(\omega)$ of a single hole created in the Ising antiferromagnet on the Bethe lattice with $z = 4$ and without magnon-magnon interactions ($\lambda = 0$) for values of $J/t \in [0, 1]$. Right panel: the shape of the spectral function at $J/t = 0.4$ (denoted by the dashed line in the left panel). The spectrum consists of a set of well-separated quasiparticle-like peaks for all values of coupling constant $J > 0$.

of well-separated quasiparticle-like peaks for all finite values of the coupling constant $J > 0$. This onset of quasiparticle peaks appears as a result of a linear potential felt by the hole—the potential that comes from the order of spins being locally spoiled when the hole moves through the antiferromagnetic background. For given J the separation between peaks is higher for $z = 4$ than for $z = 2$. This is because the cost of a magnon is proportional to z and thus the effective potential felt by the hole is steeper for higher z. In other words, a thinner potential well leads to a higher separation between energy levels. On the other hand, larger z allows the hole to delocalize more easily since there are more branches of the lattice to which the hole can propagate. As a result, the spectrum for $z = 4$ is wider than in the case of $z = 2$. The general formula for the width at $J = 0$ depends only on z and t, and it equals $4t\sqrt{z-1}$ [72].

2.2.2. Exact spectral function

Finally, let us move to the exact ($\lambda = 1$) spectral function of a single hole in the t–J^z model on the Bethe lattice with coordination $z = 4$. The result is shown in Fig. 2.5. This time, even with the magnon-magnon interactions properly included, the spec-

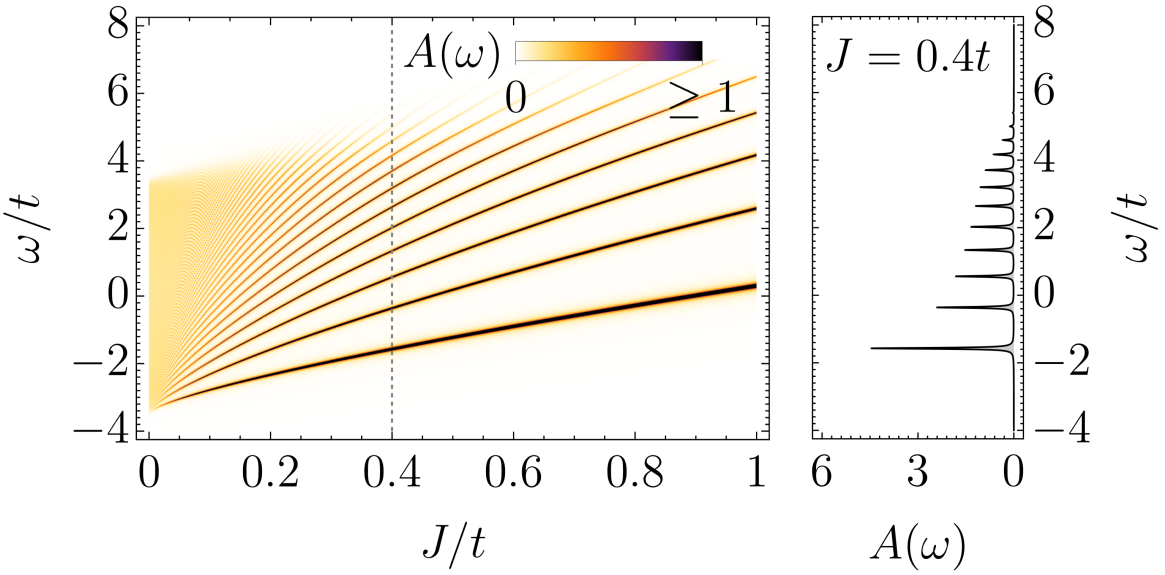

Figure 2.5: Left panel: exact ($\lambda = 1$) spectral function $A(\omega)$ of a single hole created in the Ising antiferromagnet on the Bethe lattice with $z = 4$ for values of $J/t \in [0, 1]$. Right panel: the shape of the spectral function at $J/t = 0.4$ (denoted by the dashed line in the left panel). The spectrum consists of a set of well-separated quasiparticle-like peaks for all values of coupling constant $J > 0$.

trum again is ladder-like, i.e. for any finite $J > 0$ it consists of a set of well-separated quasiparticle-like peaks. To understand this result, let us comment on the important difference between $z = 2$ and $z > 2$ cases. Let us remember that when the hole moves through an antiferromagnetic background, it shifts spins along its path spoiling the order as a result. The number of bonds connecting misaligned spins depends on the coordination number z. When $z = 2$, only one pair of spins aligned ferromagnetically can appear. But for $z > 2$ the number of such pairs scales with the distance the hole travels. Thus we can observe the magnon-magnon interactions affect the spectral function only quantitatively when $z > 2$. Effectively, the cost of each magnon becomes

smaller when magnon-magnon interactions are taken into account but it is not completely removed when $z > 2$. This stays in striking contrast with the 1D case where magnon-magnon interactions allow the creation of magnons (beyond the first one) for free leading to the collapse of the ladder spectrum.

Since magnon-magnon interactions effectively reduce the cost of creating more magnons in the system, the separation in ω for given J between the peaks is smaller once magnon-magnon interactions are included ($\lambda = 1$) than when they are switched off ($\lambda = 0$). On the other hand in both cases, the hole feels linear potential. Thus the distance between the energy levels scales like $\sim (J/t)^{2/3}$ both for $\lambda = 1$ and $\lambda = 0$.

2.2.3. Equivalence to SCBA on the square lattice

The results for the spectral function on the Bethe lattice with coordination $z = 4$ discussed in the previous sections are strongly connected to the Self-consistent Born Approximation (SCBA) of the t–J^z model on the square lattice [53, 72]. The core component of the SCBA method is a diagrammatic expansion preceded by the application of the linear spin-wave (LSW) theory which neglects magnon interactions. The set of diagrams to sum over is restricted in the SCBA to the so-called rainbow diagrams, shown in Fig 2.6.(a-c). All the rainbow diagrams are non-crossing. Thus the processes

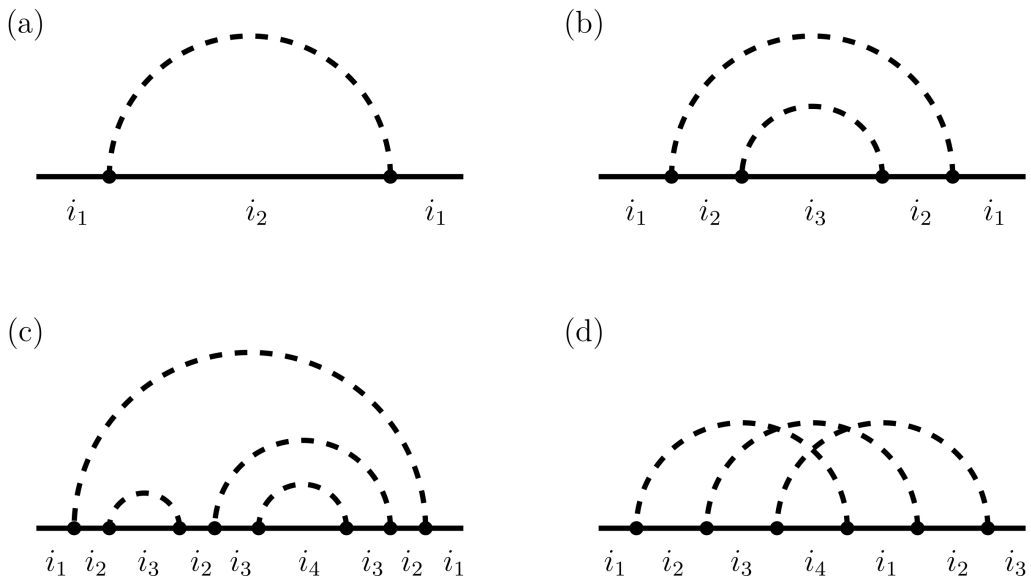

Figure 2.6: Diagrams representing the propagation of the hole introduced to the undoped antiferromagnet: (a) simplest non-crossing (rainbow) diagram representing the process of a hole moving from site i_1 to site i_2 creating a magnon (dashed line) and then going back to site i_1 to annihilate the magnon; (b-c) rainbow diagrams obtained by combining the lowest-order diagrams. Rainbow diagrams are included in the SCBA approximation; (d) a crossing diagram representing a motion of a hole in a loop. Crossing diagrams are not taken into account in the SCBA approximation.

they represent behave like a stack in a computer program, i.e. the rule first in, last out, is obeyed. In other words, the hole can only move *backward* annihilating the last created magnon or it can move *forward* creating a new magnon. This excludes all loops from the considerations. Moreover, the number of directions in which the hole

can move *forward* is also typically fixed to $d = z$. Let us discuss two ways in which one can view those processes on the lattice when $d = 4$.

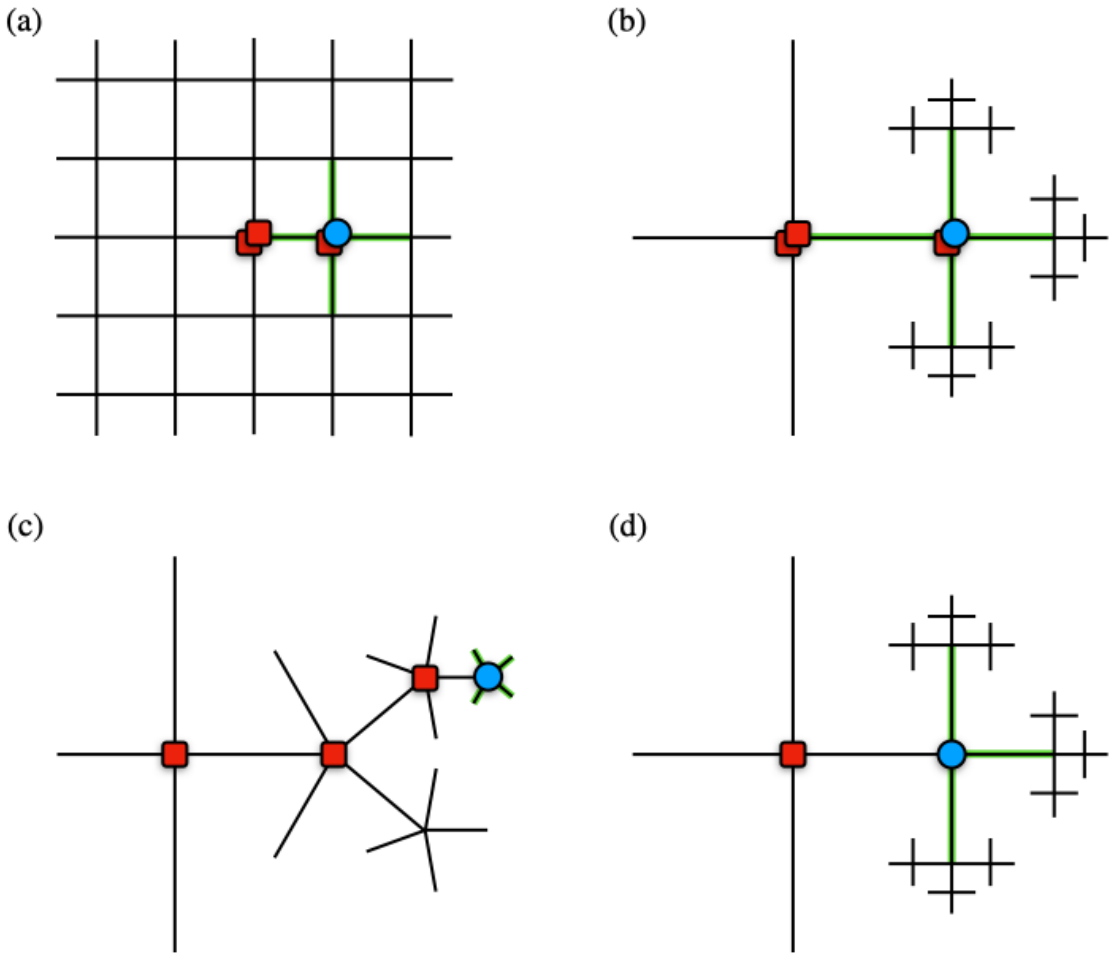

Figure 2.7: Mapping of the SCBA calculations on the square lattice onto Bethe-like lattices. The blue circle represents a hole while the red squares stand for magnons. The bonds highlighted in green show the possible direction in which the hole can propagate with the creation of a magnon. A square lattice where the hole created 3 magnons by jumping back and forth between two sites is shown in (a). Since magnons have to be annihilated in a particular order [as dictated by rainbow diagrams, see Fig. 2.6.(a-c)] loops are not important and thus the states on the square lattice can be mapped onto states on the Bethe lattice with $z = 4$ as shown in (b). Further, the fact that the magnons can only be annihilated in a given order allows for representing the non-physical states with more than one magnon per site as additional branches added to the Bethe lattice with a constraint that the number of particles in each site can be at most 1 as shown in (c). By removing the non-physical states [e.g. by means of cutting the unphysical branches in (c)] one arrives at the problem of a single hole in the t–J^z model on a Bethe lattice with $z = 4$ (discussed in Sec. 2.2) as shown in (d).

The first way is to consider a square lattice, which has $z = 4$ by definition. When the hole moves it excites magnons. From the diagrams (Fig. 2.6), there is no restriction on the number of magnons in each site. The hole can for example hop between two sites repeatedly adding a magnon with each hop, see Fig. 2.7.(a). Such states are not physical from the perspective of spin $s = \frac{1}{2}$ electrons but they are still counted

in the SCBA. Nevertheless, magnons are still ordered as if they were labeled with consecutive integers. Moreover, the energy of a given state does not depend on the labels but only on the number of magnons. This enables a one-to-one mapping of the states on the square lattice onto the states on the Bethe lattice with $z = 4$. To map between the two lattices it is enough to preserve the directions in which the hole moves [cf. Fig. 2.7.(a-b)]. One can even push this one step further to get rid of states with multiple magnon occupancies. It is enough to consider a Bethe-like lattice, which has $z = 4$ at the position where the hole is created and $z = 5$ for every other site. Now instead of moving back to the already visited site, the hole can propagate to the additional branch, see Fig. 2.7.(b-c).

One can include a small correction to the SCBA procedure and set $d = z-1$ for each move of the hole after the first one. This corresponds to forbidding the hole to move back to the last created magnon without annihilating it. Such an improved SCBA on the square lattice maps exactly onto the problem of calculating the Green's function of a single hole on the Bethe lattice with $z = 4$ as shown in Fig. 2.7.(d). The existence of this mapping means the SCBA cannot properly take into account the actual geometry of the square lattice when applied to the t–J^z model. This holds even when magnon-magnon interactions are taken into account, as can be inferred from the diagrammatic studies on t–J^z model done by Chernyshev and Leung [76]. Although the authors want to discuss the results for the square lattice they also comment that the set of diagrams they consider is still within SCBA (i.e. crossing diagrams are absent). In the end, the obtained by them expression for the Green's function coincides with the exact solution for the Bethe lattice [Eq. (2.31)] with coordination $z = 4$ and magnon-magnon included ($\lambda = 1$).

2.3. Comparison of single-hole ground state properties for $z = 2$ and $z > 2$

When looking at the spectral function of a single hole in the Ising antiferromagnet on the Bethe lattice, we can notice a low-lying quasiparticle-like peak for all $J > 0$ regardless of the coordination z of the lattice (see Figs. 2.2-2.5). This peak corresponds to the ground state of the t–J^z model in a single-hole limit. Let denote it as $|\mathrm{GS}\rangle$ to distinguish it from the ground state $|\varnothing\rangle$ without holes. Since $|\mathrm{GS}\rangle$ remains split from the rest of the states regardless of the presence of magnon-magnon interactions, one can wonder if those interactions affect $|\mathrm{GS}\rangle$ at all. Here we will derive and discuss the expressions for the expansion coefficients v_n of $|\mathrm{GS}\rangle$ in the polaronic basis $\mathcal{B}$ [77, 78]. We define P_n as a module square of those coefficients [see Eq. (2.37)]. Intuitively, such defined P_n can be understood as the probability of finding a chain of n magnons attached to the hole in the single-hole ground state $|\mathrm{GS}\rangle$ of the t–J^z model.

2.3.1. Derivation of probability P_n of finding chain of n magnons attached to the hole

The procedure for finding P_n does not depend on coordination number z (although the result does). In general, we are looking for the ground state vector $|\mathrm{GS}\rangle$. Let us denote $E_{\mathrm{GS}} = \langle \mathrm{GS}|\hat{\mathcal{H}}_{t\text{–}J^z} - E_{\varnothing}|\mathrm{GS}\rangle$. We know the analytical expression for energy E_{GS} in the case of 1D t–J^z model while for other cases (i.e. higher z or $\lambda < 1$) we can extract it

from the spectral function numerically. Therefore we need to solve the following linear equation,

$$(\hat{\mathcal{H}}_{t\text{–}J^z} - E_{\varnothing} - E_{\text{GS}})|\text{GS}\rangle = 0, \tag{2.33}$$

which after writing it basis $\mathcal{B}$ appears as,

$$\begin{bmatrix} V_0 - E_{\text{GS}} & t\sqrt{z} & & & \\ t\sqrt{z} & V_1 - E_{\text{GS}} & t\sqrt{z-1} & & \\ & t\sqrt{z-1} & V_2 - E_{\text{GS}} & t\sqrt{z-1} & \\ & & t\sqrt{z-1} & V_3 - E_{\text{GS}} & \ddots \\ & & & \ddots & \ddots \end{bmatrix} \begin{bmatrix} v_0 \\ v_1 \\ v_2 \\ v_3 \\ \vdots \end{bmatrix} = 0. \tag{2.34}$$

Coefficients V_i are given by different equations dependent on coordination z and magnon-magnon interaction λ as discussed in Sec. 2.1 and 2.2. Applying the Gaussian elimination to a finite matrix of size N and taking the limit of $N \to \infty$ the above set of equations can be reduced to the recurrence relation for consecutive coefficients v_n of the ground state vector $|\text{GS}\rangle$ in basis $\mathcal{B}$,

$$v_n = \begin{cases} v_0 & \text{if } n = 0, \\ -c_n v_{n-1} & \text{if } n > 0, \end{cases} \tag{2.35}$$

where $b_1 = t\sqrt{z}$, $b_{n>1} = t\sqrt{z-1}$ and,

$$c_n = \frac{b_n}{V_n - E_{\text{GS}} - b_{n+1}c_{n+1}}. \tag{2.36}$$

The probabilities P_n are defined as

$$P_n = |v_n|^2, \tag{2.37}$$

while $|v_0|^2$ is simply a quasiparticle residue at the ground state energy,

$$|v_0|^2 = \lim_{\omega \to E_{\text{GS}}} (\omega - E_{\text{GS}})G(\omega). \tag{2.38}$$

Therefore knowing the quasiparticle residue P_0 we can calculate $P_{n>0}$.

When we consider the case of 1D t–J^z model (i.e. $z = 2$ and $\lambda = 1$) we obtain analytical result,

$$P_n = \begin{cases} \dfrac{J}{\sqrt{J^2 + 16t^2}} & \text{if } n = 0, \\ \dfrac{2J}{\sqrt{J^2 + 16t^2}} \left(\dfrac{J - \sqrt{J^2 + 16t^2}}{4t} \right)^{2n} & \text{if } n > 0. \end{cases} \tag{2.39}$$

The above equations describe a geometric series, thus consecutive P_n decay *exponentially* as n grows,

$$\ln P_n \sim -\frac{n}{l}, \tag{2.40}$$

where $l^{-1} = 2\ln\left(\left|\frac{E_{\text{GS}} - J}{2t}\right|\right)$.

For all the other cases ($z = 2$ and $\lambda < 1$ or $z > 2$ and $\lambda \leq 1$) the hole feels a linear potential from the created magnons. We do not know the analytical expression for $|v_0|^2$ in this situation. Nevertheless, we can write a compact form of the result in terms of the Bessel functions of the first kind,

$$P_n = \begin{cases} |v_0|^2 & \text{if } n = 0, \\ 2|v_0|^2 \left(\dfrac{\mathcal{J}_{\Omega(E_{\mathrm{GS}})+n-1}(2\xi)}{\mathcal{J}_{\Omega(E_{\mathrm{GS}})-1}(2\xi)} \right)^2 & \text{if } n > 0, \end{cases} \tag{2.41}$$

where $\Omega(\omega)$ and ξ are defined accordingly to Eq. (2.32). The value of $|v_0|^2$ can be calculated numerically from the Green's function or based on the relation $\sum_{n=0}^{\infty} P_n = 1$ by taking the upper limit large since it is guaranteed that $\lim_{n\to\infty} P_n = 0$. Regardless, we can calculate the asymptotic behavior of the logarithm also in this case. For the Bessel function with small argument $0 < x < \sqrt{n+1}$ it is true that,

$$\mathcal{J}_n(2x) \simeq \frac{x^n}{\Gamma(n+1)}, \tag{2.42}$$

where Γ is a gamma function extending factorial function to complex numbers. Therefore one obtains,

$$\ln P_n \sim -2n \ln(n), \tag{2.43}$$

which yields a *superexponential* decay of P_n as n grows.

2.3.2. Intuitive physical picture

The conclusion from the above calculations is that the ground state wave function of the t–J^z model strongly depends on the presence of the magnon-magnon interactions in 1D but the difference is only quantitative in the case of $z > 2$. This result is reflected in the spectral functions discussed before where strong dependence on magnon-magnon interactions leads to a collapse of the ladder spectrum in 1D. These findings are summarized in Fig. 2.8 with simple physical pictures explaining the observed behavior. The dots in the plots correspond to analytical results for the Bethe lattice derived in the previous section (see Eqs. (2.39) and (2.41)). The solid lines are just a guide for the eye.

In the 1D t–J^z model (with magnon-magnon interactions included) the hole feels only a point potential coming from a single unsatisfied bond created with the first move of the hole. Once the first magnon is created other magnons do not cost any energy, thus the hole can move away for free, see Fig. 2.8.(a2). The cost of other magnons is removed by the magnon-magnon interactions that happen to contribute exactly the opposite amount of energy than magnons. This eventually leads to an exponential decay of P_n as shown in Fig. 2.8.(a1). We can say that in this case, the hole is "weakly" bound by the magnons.

When magnon-magnon interactions are neglected (or taken into account partially with $0 < \lambda < 1$) or when coordination number $z > 2$ then the energy cost of creating new magnons cannot be removed. The hole does not feel the point potential but a close to linear potential caused by linear growth of the number of magnons in the system due to a motion of the hole, see Fig. 2.8.(b2-d2). We will call this type of potential a string potential since it originates from string-like structures of magnons with equal non-zero energetic cost (for each magnon inside a chain). String potential leads to a superexponential decay of P_n as shown in Fig. 2.8.(b1-d1). We can say in this case the hole is "strongly" bound by the excited magnons.

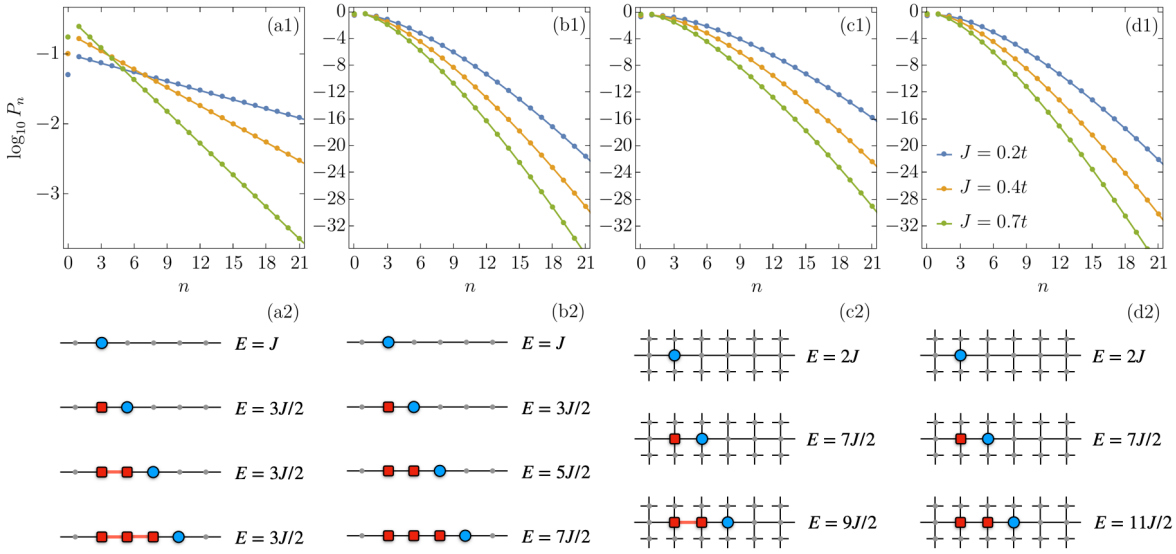

Figure 2.8: Probablity P_n of finding n magnons in a chain attached to the hole in the single-hole ground state $|\text{GS}\rangle$ of the t–J^z model. Dots represent analytical solutions for Bethe lattice for (a1) $z = 2$ and $\lambda = 1$ (i.e. 1D t–J^z model); (b1) $z = 2$ and $\lambda = 0$ (i.e. 1D t–J^z model without magnon-magnon interactions); (c1) $z = 4$ and $\lambda = 1$; (d1) $z = 4$ and $\lambda = 0$. Solid lines are included as guides for the eye. Corresponding cartoon pictures (a2-b2) of the hole motion in 1D (Bethe lattice with $z = 2$) and (c2-d2) Bethe lattice with $z = 4$ antiferromagnet are shown below each plot. The blue circle represents the hole while the red squares stand for magnons. The bonds highlighted in red represent the presence of the magnon-magnon interactions accordingly to the t–J^z model (i.e. Hamiltonian (1.26) with $\lambda = 1$). Figure based on Ref. [77].

2.3.3. Connection to cold atoms experiments

The motivation behind looking at such an observable as P_n is the possibility to measure it in the cold atoms experiments [56, 57, 79]. In those experiments, a set of atoms is trapped in a grid of electromagnetic beams forming the so-called optical lattice [see Fig. 2.9.(a)]. The interaction strength U between the atoms at the same lattice site, as well as hopping amplitudes t between neighboring lattice sites, can be controlled externally. This allows for an approximate realization of the Fermi-Hubbard model on a finite lattice.

The results in Fig. 2.9.(b) were obtained by performing the same experiment many times and taking snapshots of the propagation of holes in the system. Then the pattern recognition analysis allows counting the strings of a given length l of spins misaligned w.r.t. the antiferromagnetic background. This leads to a probability distribution $p^\delta(l)$, where δ is a doping level of holes. When a single hole is doped, this quantity is analogous to the probability P_n but calculated for a Hubbard model on a 2D square lattice. The results for $p^\delta(l)$ obtained by Christie S. Chiu *et* al. [56] suggest rather exponential than superexponential behavior. Based on our knowledge of the hole in the t–J^z model, we can conclude that holes do not feel the string potential in the Hubbard model.

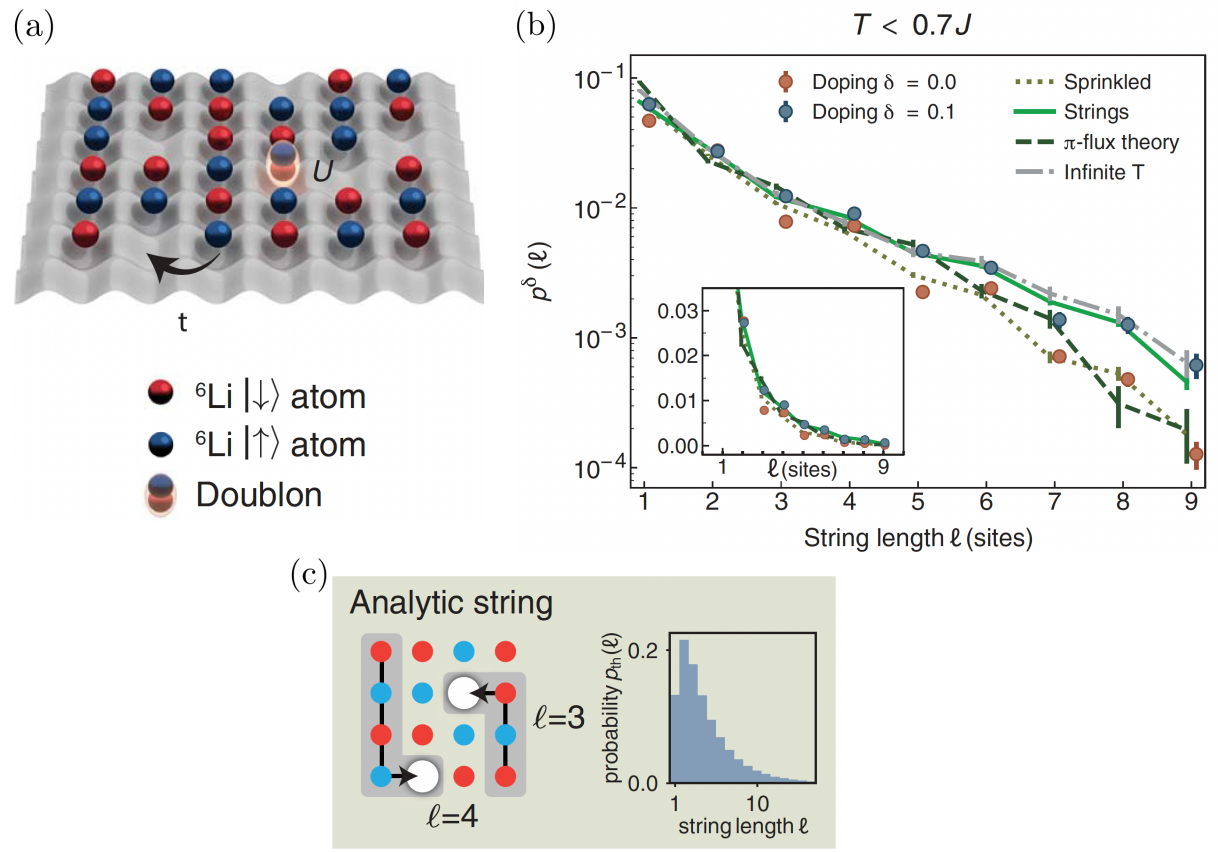

Figure 2.9: String patterns recognition in the cold atoms experiment (figures taken from Ref. [56]). (a) Optical lattice with lithium atoms simulating the physics of a Fermi-Hubbard model. (b) Experimental data was collected for half-filling and 10% hole doping. The green solid line denotes (c) theoretical predictions from artificially created snapshots of the system.

2.4. Conclusions

To better understand the underlying differences between a single hole in 1D and 2D antiferromagnet we study the t–J^z model with scalable magnon-magnon interactions (1.26) on the chain (Bethe lattice with coordination $z = 2$, see Sec. 2.1) and on the Bethe lattice with coordination $z = 4$ (see Sec. 2.2). From the analytically calculated Green's functions [Eqs. (2.19) and (2.31)] we find out that for magnon-magnon interactions $\lambda < \frac{z}{2}$ the ladder-like spectrum is obtained (see Figs. 2.2, 2.4 and 2.5) while for $\lambda = \frac{z}{2}$ the spectrum of a single hole consists of a delta-like peak at the ground state energy and the incoherent continuum of excited states split from the ground state (see Fig. 2.3) for all couplings $J/t > 0$. The latter result corresponds precisely to the case of 1D t–J^z model (1.25), where magnon-magnon interaction has critical value ($\lambda = 1$), leading to the cancellation of the energy cost for creating consecutive magnons by the moving hole [cf. Fig. 2.8.(a2-b2)]. Any λ other than 1 leads to the ladder-like spectrum, which reveals the crucial role of the magnon-magnon interactions in 1D t–J^z model.

Further, we study the effects of magnon-magnon interactions on the localization of the hole in the t–J^z model. To this end, we calculate the expansion coefficients of the ground state wave function of a single hole in magnon-holon basis. From this, we calculate the probability P_n [Eq. (2.37)] of finding the hole n sites away from the site

where the hole has been created, Eq. (2.37). When the hole is subject to the string potential from created magnons, the coefficients P_n decay superexponentially with n. But for the case of the 1D t–J^z model, the magnons effectively do not cost energy (apart from the very first one), which results in the exponential decay of P_n (see Fig. 2.8). Comparing our findings with the cold atoms experiments on the Hubbard model we conclude that the hole in the Hubbard model is not subject to the string potential (see. Sec. 2.3.3).

As a side remark, we point out that results based on the SCBA inevitably neglect the geometry of the square lattice due to a lack of crossing diagrams. We show that in the case of the SCBA for 2D t–J^z model the parent model for the obtained results (i.e. the model for which the obtained results are exact) is, in fact, the t–J^z model on the Bethe lattice (see Sec. 2.2.3).

Chapter 3

The t–J^z model on the 2D square lattice: incoherent spectrum

Based on Piotr Wrzosek and Krzysztof Wohlfeld, Physical Review B ***103*** *(3), 035113 (2021).*

The discussed in the previous chapter t–J^z model on the Bethe lattice does not fully capture the geometry of the square lattice. At least two kinds of processes, originating from the existence of loops on the square lattice, are not present in the Hilbert space of the problem on the Bethe lattice (due to the lack of loops in the latter one). Moreover, these processes are not taken into account in the SCBA since they are represented by crossing diagrams. In this chapter, we develop a special way of numerically calculating the spectral function of a single hole in the t–J^z model on the 2D square lattice that allows us to differentiate between the two processes to investigate their importance for the spectral properties of the hole.

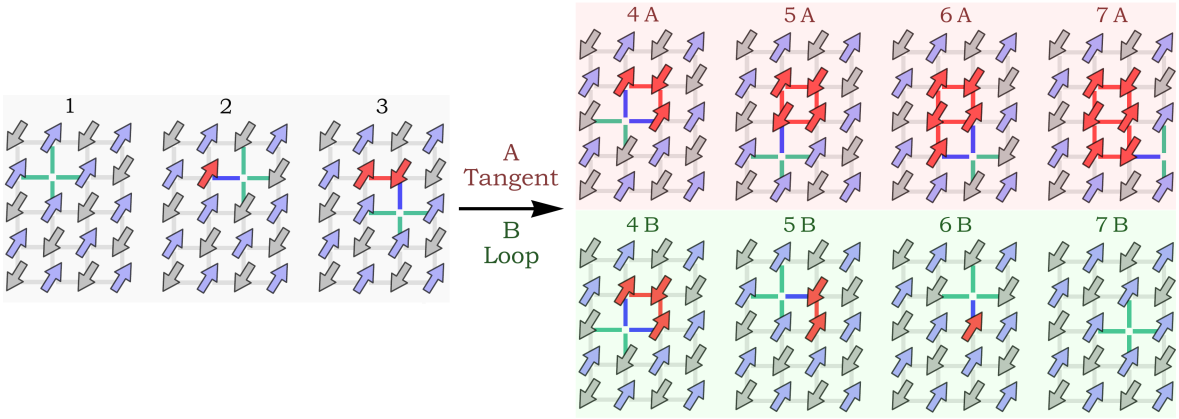

Figure 3.1: Examples of a hole motion in a 2D antiferromagnet including processes not present on the Bethe lattice. Initially, the hole motion does not differ from the movement on the Bethe lattice (1-3) but later the geometry of the 2D square lattice allows the hole to move along a tangential path (4A-7A) or a Trugman loop (4B-7B). Bonds highlighted in green denote directions of the propagation of the hole resulting in a shift of a spin out of the initial AF order. Bonds highlighted in blue denote directions which allow the hole to repair the created AF disorder (spins highlighted in red). Figure based on Ref. [80].

The *first* process is a simple motion of the hole in a loop. Moving one and a half

times in a loop, the hole on the square lattice can move between opposing corners of the loop in a process similar to tunneling over a potential barrier. Although the contribution to the ground state from these so-called Trugman loops is insignificant for experimentally relevant values of $J =\sim 0.4t$, they lead to a small momentum dependence in the system.

The *second* process is when the hole moves almost in a loop such that the set of created magnons cannot be described as a one-dimensional object. We will call this type of path of the hole a tangential path. Formally a requirement for a path to be tangential is to contain a pair of two neighboring (i.e. connected by a bond) sites that have been visited by the hole but the hole did not travel through the bond connecting the two sites. An example of these two processes is presented in Fig. 3.1.

3.1. Coherent versus incoherent spectrum: comparison between exact diagonalization on Bethe lattice versus square lattice

The typical understanding of the hole in the 2D antiferromagnet comes from the SCBA approximation or considering the Bethe lattice instead of a 2D one. In this case, the spectrum of a single hole consists of a set of quasiparticle peaks as a result of a hole being subject to the string potential, see Fig. 2.5. But the exact diagonalization (ED, own Lanczos code) results on a 2D square lattice provide us with a completely different picture of the spectral function $A(k, \omega)$ in Eq. (1.2), as shown in Fig. 3.2.

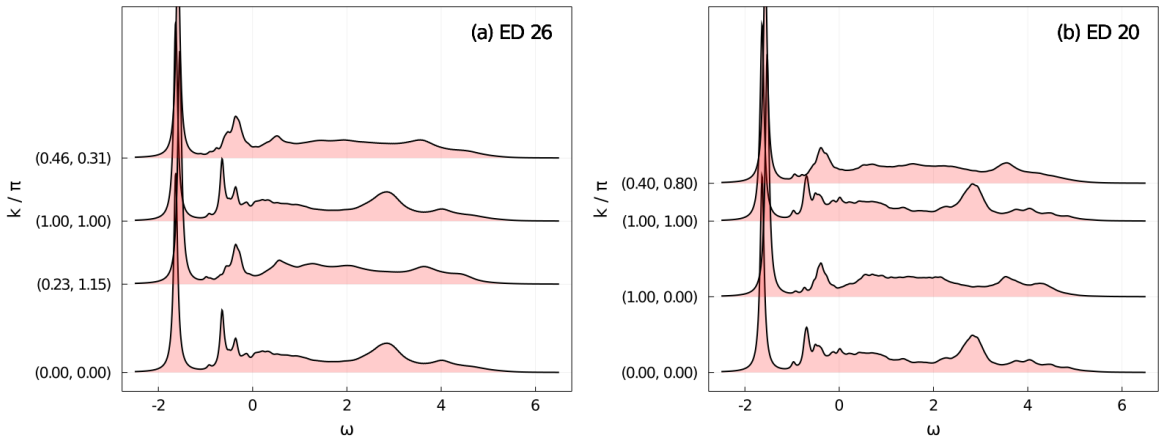

Figure 3.2: Spectral function $A(k, \omega)$ of a single hole in the t–J^z model on a 2D square lattice. ED was performed for (a) 26 sites on the left panel and (b) 20 sites on the right panel. Each panel consists of 4 spectra for different values of the introduced hole momentum k. Values of k for the corresponding spectra on the left and the right panel were chosen as the closest possible. Spectra calculated for the standard value of the coupling constant $J = 0.4t$. Figure taken from Ref. [80].

Although we can see a low energy peak, the rest of the spectrum above consists of a broad continuum (so-called incoherent spectrum). The continuum of states appears for any value of momentum k of the introduced hole. Importantly, this continuum of states is not merely a result of numerical broadening. In Fig. 3.2, in both panels, the coupling constant is taken as $J = 0.4t$, which is a standard value for cuprate

compounds. Moreover, from the comparison of the results for 20 and 26 sites, we can conclude the finite size effects are small and the incoherent part of the spectrum is a genuine result.

It turns out the spectrum of a hole in the 2D Ising antiferromagnet of Fig. 3.2 somewhat resembles the 1D case where magnons effectively do not cost energy ($\lambda = 1$), see Fig. 2.3. This stands in contradiction to the hole being subject to the string potential at finite J in 2D. To understand this result carefully, we will proceed by developing a special method of calculating a Green's function and thus also a spectral function of a single hole introduced into the 2D Ising antiferromagnet that goes beyond the standard approaches. The design of the method will allow us to investigate the role the magnon-magnon interactions play in the observed physics of the single hole in 2D t–J^z model in the presence of the so-called tangential paths (see below).

3.2. Beyond the Bethe lattice: self-avoiding walks (SAW) approximation

On the Bethe lattice, we could easily take the magnon-magnon interactions into account since all the magnons were interacting only along the path of the hole, see Fig. 2.8.(c2). As one can notice in Fig. 3.1, for a tangential path this assumption does not hold. Apart from the interactions between magnons along the path of the hole, magnons can also interact along the bonds where the path of the hole becomes tangential. While the bonds along the path are naturally parallel to the path of the hole, on the square lattice the bonds where the path becomes tangential are perpendicular to the path. Parallel bonds can be easily taken into account when calculating the spectral function, while the perpendicular bonds need us to go beyond the SCBA or Bethe lattice approximations. Including the physics along perpendicular bonds properly can be understood as including crossing diagrams in the diagrammatic expansion of the Green's function.

From Fig. 3.2 we know the ground state of the system in a single-hole limit is barely dependent on the momentum (at least for the studied in this thesis typical limit of $J \geq 0.4t$). The general feature of the spectrum in higher energies—incoherence—also does not depend on the momentum. Moreover, the respective size of the subset of the Hilbert space consisting of the Trugman loops vanishes with the system size [81]. Altogether, neglecting the Trugman loops should not substantially affect the spectral function nor the physics of the single hole for $J \geq 0.4t$. Of course, this would leave the spectrum momentum independent and thus the local spectral function would contain the same information as the momentum-resolved one.

With all the above pieces of information, the direction we want to take is to calculate the local spectral function of a single hole within the *self-avoiding walks* (SAW) approximation. The idea behind this approximation is to remove the self-consistency from the expression for Green's function by neglecting the paths of the hole that contain loops. Thus the resulting equations will at most be recursive. This in turn should allow us to include the magnon-magnon interactions exactly (both along parallel and perpendicular bonds) while keeping still decent system sizes (i.e. ~ 800 lattice sites). To this end, we will follow the original description of the method [80]. Moreover, we will provide some insight into the optimizations of the code for the calculations, which we have spared in [80]. In the end, we will briefly discuss how this idea can be generalized

to any operator (i.e. not only the Hamiltonian of the t–J^z model).

Let us start by writing the Hamiltonian (1.26) of the t–J^z model with scalable magnon-magnon interactions in the polaronic language in the expanded form, where terms responsible for the proximity effect (hole-magnon interaction) are explicitly written out. This is a purely cosmetic adaptation to fit the original formulation of the problem [80]. Later it will turn out that the proximity interaction has a negligible effect on the spectral properties (at least in the single-hole limit). The model reads, $\hat{\mathcal{H}}_{t\text{–}J^z}(\lambda) = \hat{\mathcal{H}}_t + \hat{\mathcal{H}}_z(\lambda)$ where after rewriting $\hat{\mathcal{H}}_z(\lambda)$ can be expressed as,

$$\hat{\mathcal{H}}_z(\lambda) - E_\varnothing = \frac{J}{2}\sum_{\langle i,j\rangle}\left(\hat{a}_i^\dagger\hat{a}_i + \hat{a}_j^\dagger\hat{a}_j - 2\lambda\hat{a}_i^\dagger\hat{a}_i\hat{a}_j^\dagger\hat{a}_j\right) \tag{3.1}$$

$$+ \frac{J}{2}\sum_{\langle i,j\rangle}\left(\hat{h}_i^\dagger\hat{h}_i + \hat{h}_j^\dagger\hat{h}_j - \hat{h}_i^\dagger\hat{h}_i\hat{h}_j^\dagger\hat{h}_j\right) \tag{3.2}$$

$$- \frac{J}{2}\sum_{\langle i,j\rangle}\left(\hat{a}_i^\dagger\hat{a}_i\hat{h}_j^\dagger\hat{h}_j + \hat{h}_i^\dagger\hat{h}_i\hat{a}_j^\dagger\hat{a}_j\right). \tag{3.3}$$

To understand what different terms in the model are responsible for, let us have a look at the cartoons of the hole propagation on a square lattice—but this time we will pay close attention to the geometry of a square lattice.

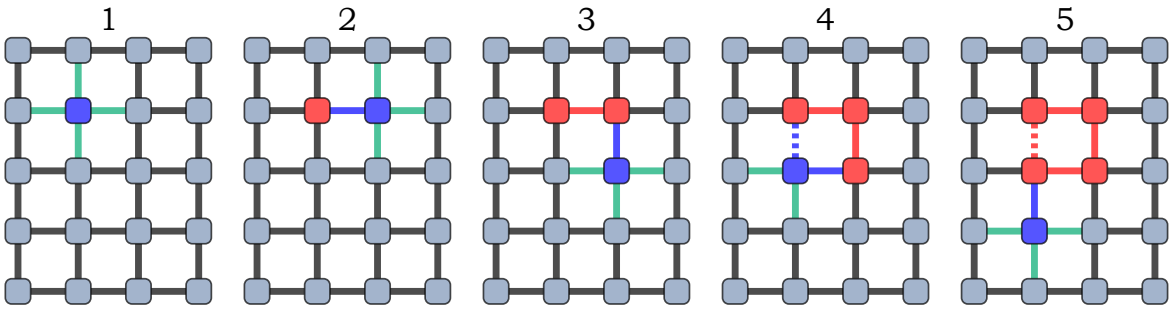

Figure 3.3: Propagation of the hole in the square lattice in the polaronic description. Within the SAW approximation, the hole (blue square) can only move through the bonds denoted by solid green or blue lines. The propagation through the dashed bonds is forbidden as it would result in the hole crossing its path (i.e. the hole would move in a loop). Propagation through one of the green bonds results in the creation of a magnon (red square) while propagation through the blue bond always results in the annihilation of the most recently created magnon. Magnon-magnon interactions are denoted at bonds highlighted in red (both solid and dashed), while the proximity effect happens at blue bonds (solid or dashed). Figure taken from Ref. [80].

In Fig. 3.3 the hole moves along the same bonds as in Fig. 3.1.(1-3,4A,5A). Each important term in the Hamiltonian has been denoted either by colored squares representing the occupation of a given site or colored bonds for two-particle interaction on nearest neighbor sites. The site occupied by a hole ($\hat{h}_i^\dagger\hat{h}_i$) is denoted by a blue square. The site occupied by a magnon ($\hat{a}_i^\dagger\hat{a}_i$) is denoted by a red square. The hole can move along solid green bonds creating a magnon ($\hat{h}_i^\dagger\hat{h}_j\hat{a}_j^\dagger$) or through the solid blue bond annihilating the most recently created magnon ($\hat{h}_i^\dagger\hat{h}_j\hat{a}_i$). Within the SAW approximation, the propagation of the hole through bonds denoted with dashed lines is forbidden. Note that the positions of the dashed bonds are path-dependent. On

the other hand, $\hat{\mathcal{H}}_{t-J^z}$ is taken into account without approximations. Each blue bond (dashed or not) corresponds to the proximity effect ($\hat{h}_i^\dagger \hat{h}_i \hat{a}_j^\dagger \hat{a}_j$). Similarly, each red bond (solid or dashed) denotes the magnon-magnon interaction ($\hat{a}_i^\dagger \hat{a}_i \hat{a}_j^\dagger \hat{a}_j$). The hole-hole interaction term ($\hat{h}_i^\dagger \hat{h}_i \hat{h}_j^\dagger \hat{h}_j$) never contributes since we always deal with at most one hole in the system. The corresponding hole motion on the Bethe lattice is shown in Fig. 3.4. Notice how the walk becomes self-avoiding on the Bethe lattice due to a lack of loop. In general, a non-returning path in a tree graph is always self-avoiding.

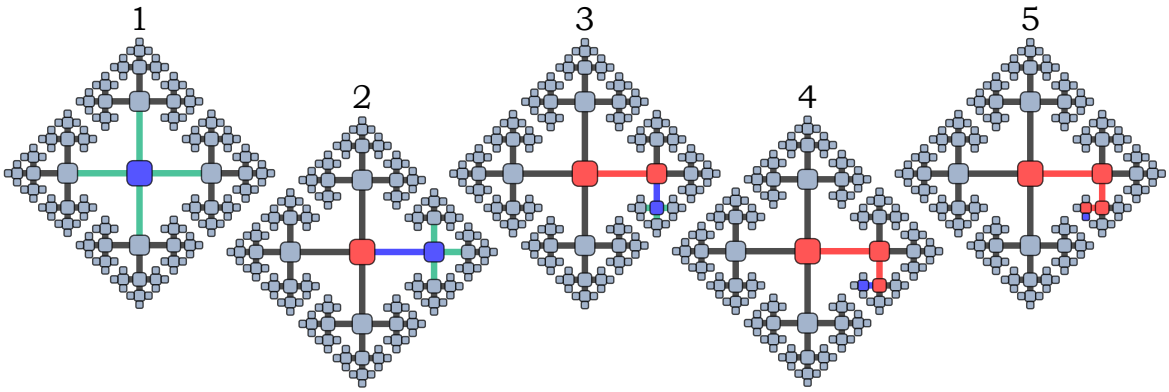

Figure 3.4: Propagation of the hole in the bathe lattice in the polaronic description. The hole moves in the *same* directions the same as in Fig. 3.3. Since Bethe lattice is a tree, thus every walk is self-avoiding—notice the lack of dashed bonds. The hole (blue square) can move through the bonds denoted by green or blue lines. Propagation through one of the green bonds results in the creation of a magnon (red square) while propagation through the blue bond always results in the annihilation of the most recently created magnon. Magnon-magnon interactions are denoted at bonds highlighted in red, while the proximity effect happens at the blue bond. Figure taken from Ref. [80].

3.2.1. Definitions and derivation of the Green's function

Let $\mathcal{S}$ stand for the subspace of the Hilbert space consisting of all states where the path of the hole is a self-avoiding walk. To generate subspace $\mathcal{S}$, we define a spanning operator,

$$\mathcal{A}^\dagger|\psi\rangle = \bigcup_{\langle i,j\rangle} \left\{ \left(\hat{h}_i^\dagger \hat{h}_j \hat{a}_j^\dagger \hat{P}_i + \hat{h}_j^\dagger \hat{h}_i \hat{a}_i^\dagger \hat{P}_j \right) |\psi\rangle \right\} \setminus \{0\}. \tag{3.4}$$

Consistently with the notation for the Bethe lattice, let $|0\rangle = \hat{h}_i^\dagger|\varnothing\rangle$ be the initial state with the hole introduced to the vacuum state at site i of the lattice (our local Green's function does not depend on the label i). This state is naturally a part of $\mathcal{S}$. Let us define $\mathcal{S} \supset \mathcal{S}_0 = \{|0\rangle\}$ and for $n > 0$,

$$\mathcal{S}_n = \bigcup_{|\psi\rangle \in \mathcal{S}_{n-1}} \mathcal{A}^\dagger|\psi\rangle. \tag{3.5}$$

From this point, we proceed to prove that the above-defined recurrence relation can successfully generate $\mathcal{S}$.

Let us assume $\mathcal{S}_{n-1}$ contains all the self-avoiding walks with $n-1$ magnons in a path (where the path starts at site i). The projector $\hat{P}_i$ in the spanning operator $\mathcal{A}^\dagger$

forbids the hole to hop to a site occupied by a magnon. Thus, if paths in $\mathcal{S}_{n-1}$ are self-avoiding, then also paths in $\mathcal{S}_n$ are self-avoiding. Moreover, every time the hole travels to an unoccupied site, one magnon is created thanks to $\hat{a}_i^\dagger$ terms in $\mathcal{A}^\dagger$. Therefore any state in $\mathcal{S}_n$ have n magnons. The completeness of the $\mathcal{S}_n$ comes from the fact that we sum over all self-avoiding paths with $n-1$ magnons and all bonds in the lattice. Thus the hole will necessarily be propagated through all the possible bonds that do not lead to a crossing path. Therefore from the assumption on $\mathcal{S}_{n-1}$ it follows that $\mathcal{S}_n$ will contain all the possible self-avoiding walks (starting at i) with n magnons. Of course, $\mathcal{S}_0$ contains all the self-avoiding walks (starting at site i) with 0 magnons. Thus by induction,

$$\mathcal{S} = \bigcup_n \mathcal{S}_n. \tag{3.6}$$

In practice, we shall restrict $\mathcal{S}$ to a set of walks that are not larger than a certain length based on the convergence of the results for the spectral function.

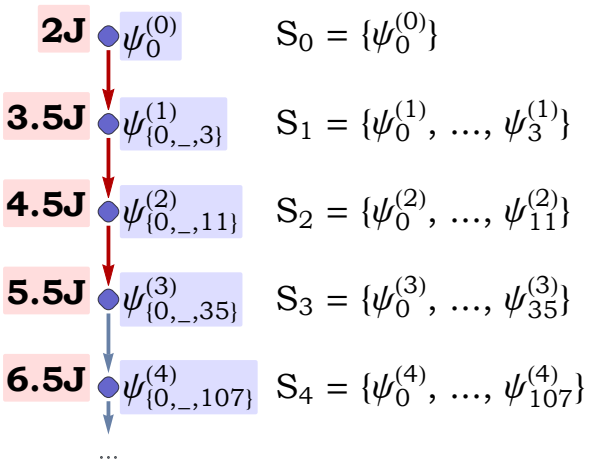

Figure 3.5: Graph of the structure of subspaces contributing to Green's function of a single hole doped to the half-filled limit of the t–J^z model on the Bethe lattice. Each node represents a set of states (denoted by blue labels) with the same energy V_n (red labels). Corresponding subspaces $\mathcal{S}_n$ of states with the same number of magnons are listed next to the graph. Each arrow denotes the propagation of the hole leading to a creation of a magnon. Arrows highlighted in red correspond to e.g. the propagation of the hole shown in Fig. 3.4.(1-4). The linear structure of the graph reflects the continued fraction form of the solution for Green's function on the Bethe lattice given in Eq. (2.28). Figure taken from Ref. [80].

This approach can also be applied to a Bethe lattice. In fact, calculating Green's function in subspace S defined on the Bethe lattice is simpler than on the square lattice, which is of primary interest here. Therefore let us start with the former case. If the sum in the definition of $\mathcal{A}^\dagger$ runs over the sites of a Bethe lattice, then set $\mathcal{S}$ is exactly equal to to the full subspace of states reachable by the hole from state $|0\rangle$ on the Bethe lattice, i.e. states defined in Eq. (2.22). We can also write,

$$|n\rangle = \frac{1}{\sqrt{||\mathcal{S}_n||}} \sum_{|\psi\rangle \in \mathcal{S}_n} |\psi\rangle \quad \text{for } n \geq 0, \tag{3.7}$$

which exactly covers Eq. (2.26). Let $|\psi_{i\in I_n}^{(n)}\rangle \in \mathcal{S}_n$ where I_n is an index set of $\mathcal{S}_n$. On

the Bethe lattice, it is true that,

$$\langle \psi^{(n)}_{i\in I_n} | \hat{\mathcal{H}}_z(\lambda) | \psi^{(n)}_{i\in I_n} \rangle = V_n, \tag{3.8}$$

regardless of i (i.e. regardless of the actual path of the hole). Thus states defined in Eq. (3.7) are also eigenstates of $\hat{\mathcal{H}}_z(\lambda)$ with the same eigenvalue V_n. We could observe that this leads to a solution for the Green's function in a form of a continued fraction [see e.g. Eq. (2.28)]. We can represent the structure of this Green's function by a simple diagram, see Fig. 3.5.

When we consider the 2D square lattice, the existence of tangential paths which allows for the additional magnon-magnon and hole-magnon interactions to happen invalidates Eq. (3.8). Thus we cannot simply introduce the basis that tridiagonalizes the Hamiltonian. While the linear structure of the graph representing Green's function on the Bethe lattice corresponds to a continued fraction, a tree graph for the reachable subspaces on the 2D square lattice, shown in Fig. 3.6, reflects the tree-like structure of Green's function on the square lattice. For example, the red arrows in Fig. 3.6 track the motion of the hole shown in Fig. 3.3.(1-4). Notice how they arrive at the states with energy $5J$ although other states with the same number of magnons have energy $5.5J$—this is the effect of a tangential path. The additional interaction of the hole with a magnon reduces the energy by $J/2$. This tree-like structure can be obtained

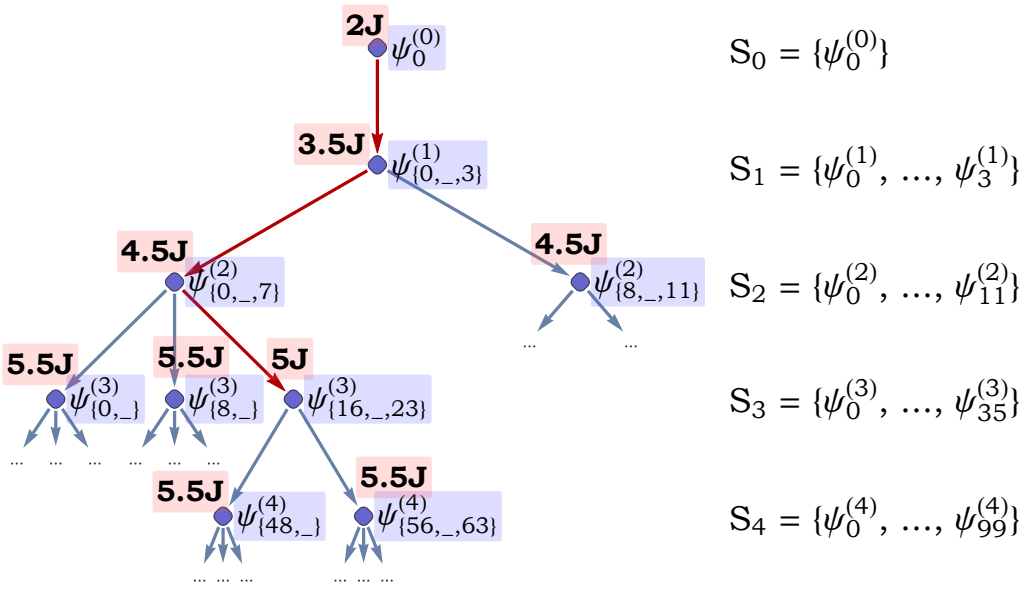

Figure 3.6: Graph of the structure of subspaces contributing to Green's function of a single hole doped to the half-filled limit of the t–J^z model on the square lattice within SAW approximation. Each node represents a set of states (denoted by blue labels) with the same energy V_n (red labels). Corresponding subspaces $\mathcal{S}_n$ of states with the same number of magnons are listed next to the graph. Each arrow denotes the propagation of the hole leading to a creation of a magnon. Arrows highlighted in red correspond to e.g. the propagation of the hole shown in Fig. 3.3.(1-4). The linear structure of the graph reflects the continued fraction form of the solution for Green's function on the Bethe lattice given in Eq. (3.9). Figure taken from Ref. [80].

algebraically by considering the matrix of the Hamiltonian written in basis of states given by $\mathcal{S}$ on the square lattice. Although such a matrix is not tridiagonal, a procedure

analogous to that described in Eq. (2.12) allows us to express our Green's function of interest in a recursive form. It is given by,

$$G(\omega)^{-1} = G_0(\omega)^{-1} - \Sigma_{\psi_0^{(0)}}(\omega), \tag{3.9}$$

where the bare Green's function $G_0(\omega) = (\omega - \omega_{\psi_0^{(0)}})^{-1}$. The self-energy $\Sigma_{\psi_0^{(0)}}(\omega)$ can be obtained from the recurrence relation,

$$\Sigma_\psi(\omega) = \sum_{|\phi\rangle \in \mathcal{A}^\dagger|\psi\rangle} \frac{t^2}{\omega - \omega_\phi - \Sigma_\phi(\omega)}, \tag{3.10}$$

with $\omega_\psi = \langle\psi|\hat{\mathcal{H}}_J|\psi\rangle$.

A typical procedure of calculating the above-defined Green's function requires us to generate the graph shown in Fig. 3.6 up to a given depth L. Let N stand for the number of nodes in the graph. The only symmetries that we take into account to shrink the graph are the fourfold symmetry C_4 around the origin and mirror symmetries M_x and M_y. This is why there is only a single arrow from the first node (instead of four) and two arrows from the second one (instead of three). Therefore, the maximum degeneracy of each node (i.e. number of states it corresponds to) is 8. This means N scales linearly with the size of the considered Hilbert subspace.

The pessimistic time complexity for generating the graph is $O(N \log N)$—logarithm comes from checking whether the path is self-avoiding. Hash maps allow achieving the average complexity of $O(N)$. The same applies to memory complexity, it is $O(N)$ to store the graph. This is much better than the exact diagonalization that needs $O(N^3)$ time and $O(N^2)$ memory (or $O(N)$ memory if sparse matrix representation can be used) to calculate eigenvalues and eigenvectors. For the same task, Arnoldi (Lanczos) procedure typically needs $O(K \cdot N^2)$ time and $O(N^2)$ memory (or $O(K \cdot N)$ time and $O(N)$ memory if the problem is sparse), where K is the size of the Krylov subspace (typically few to several hundred).

Once the graph is created, to calculate $G(\omega)$ for given $\omega \in \mathbb{C}$ it is enough to visit each node once. Thus the complexity of calculating $G(\omega)$ at M distinct points is $O(M \cdot N)$. The memory needed to store $G(\omega)$ can be typically completely neglected ($M \ll N$). Moreover, all the calculations of different omega points can be run in parallel. One shared graph can be used for all the processes (no locking is needed since read memory access does not raise a race condition). Parallelization is possible since the calculations are completely independent, unlike in self-consistent approaches.

3.3. Spectral function within SAW approximation

In the previous section, we have learned how to efficiently calculate the Green's function of a single hole in the t–J^z model on the square lattice within SAW approximation. Now, let us focus on the corresponding local spectral function $A(\omega)$. All the results using SAW are calculated for up to 20 magnons in a chain—this is more than $1.4 \cdot 10^9$ basis states or over 800 lattice sites and gives converged spectra for $J/t > 0.3$. In addition, we will compare the SAW results to exact diagonalization calculations performed on the square lattice with 26 sites. Results from both methods are shown in Fig. 3.7.

First, let us describe the general features of both SAW and ED spectra shown in Fig. 3.7. The local spectral function $A(\omega)$ for the canonical value of the coupling

constant $J/t = 0.4$ consists of a sharp peak at low energies. This peak is separated from the continuum of excitations above. Those are the same qualities the momentum-resolved spectra possess (cf. Fig. 3.2). For larger couplings J the spectrum becomes more coherent. While the continuum in higher energies is still present, the shape of the spectrum resembles more the one of the hole on the Bethe lattice—a ladder-like spectrum. We would like to point out here, although in the presented figures the broadening is quite large ($\delta = 0.05t$), the continuum did not disappear even with broadenings as small as $\delta = 10^{-6}t$.

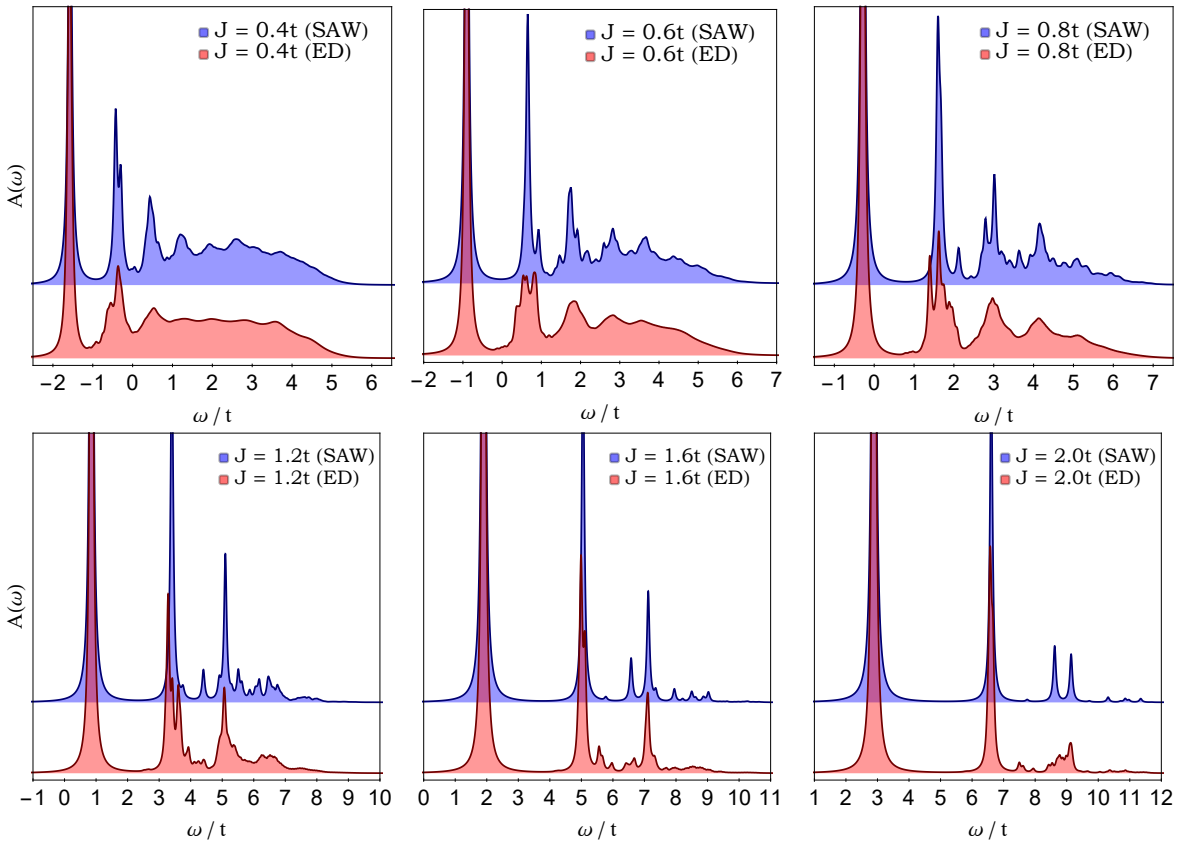

Figure 3.7: Spectral function of a single hole in the t–J^z model on a 2D square lattice. ED (red data) was calculated for 26 sites cluster. SAW (blue data) calculations were performed for up to 20 magnons in a chain. Spectra were calculated for the standard value of the coupling constant $J = 0.4t$ as well as higher couplings as labeled in the figures. Broadening $\delta = 0.05t$. Figure taken from Ref. [80].

3.3.1. Agreement with exact diagonalization

The overall shape of the spectrum obtained within the SAW approximation (Fig. 3.7, blue data) matches very well the shape of the local spectral function calculated in ED (Fig. 3.7, red data) for all values of the coupling constant J. We quantitatively confirm this claim, by calculating the overlap between the two spectra. The following correlation function,

$$\xi(A,B) = \frac{\int_{-\infty}^{\infty} A(\omega)B(\omega)\,d\omega}{\sqrt{\int_{-\infty}^{\infty} |A(\omega)|^2 d\omega \int_{-\infty}^{\infty} |B(\omega)|^2 d\omega}}, \tag{3.11}$$

calculates the overlap between functions A and B. In addition, we also calculate the same quantity for the Bethe lattice against ED. Both results are shown in Fig. 3.8. In

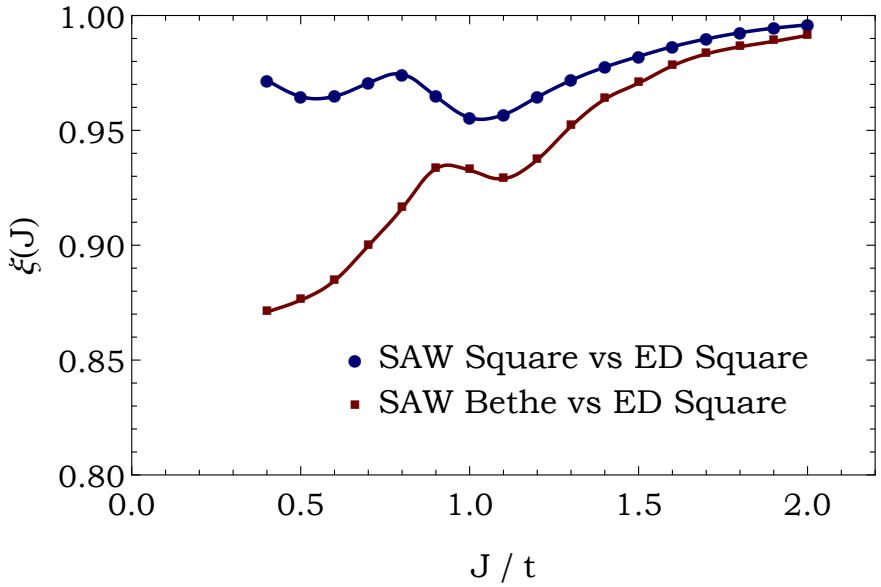

Figure 3.8: Correlation ξ [Eq. (3.11)] between exact diagonalization result on a square lattice and SAW approximation on a square lattice (blue circles) or exact result (equivalent to SAW) on the Bethe lattice (red squares). Lines were added as a guide for the eye. ED was performed on a square lattice with 26 sites. SAW on the square lattice included up to 20 magnons in a chain. All results were obtained with the same broadening $\delta = 0.05t$. Figure taken from Ref. [80].

general, the agreement of SAW with ED is substantially better than the agreement of the Bethe lattice approximation with ED. Especially for the coupling constant $J = 0.4t$ where the error made by SAW is a few times smaller than the one from the Bethe lattice calculations.

Visible in Fig. 3.7 spectral features on top of the continuum are more pronounced in SAW than in ED but all those peak-like structures are centered around similar energies in both methods. Especially the energy of the ground state matches almost perfectly. Overall, the obtained results strongly suggest that neglecting the loops for $J/t \geq 0.4$ does not affect the physics of the hole in the t–J^z model substantially. The drastic decrease in the importance of loops for higher J values and progressing convergence of the SAW on the square lattice and the Bethe lattice results toward ED visible in Fig. 3.8 for $J/t > 1$ can be relatively easily explained. This comes from the fact that the contribution to the self-energy from the lowest order loops scales as t^6/J^5 [54]. Higher order loops decay even faster with growing J. While for small couplings, e.g. $J/t < 0.1$, the contribution of the loops may become significant in determining the spectral function, the spectra for intermediate values ($J/t \in [0.4, 1.0]$) still seem to be most affected by some other processes in the system, e.g. the magnon-magnon interactions.

3.3.2. Crucial role of magnon-magnon interactions

The observations made in the previous section bring us to the role of the magnon-magnon interactions in the investigated system. First, let us address the difference

between the ladder-like spectrum from Bethe lattice calculations and the spectrum within SAW approximation on the 2D square lattice. The results are shown in Fig. 3.9. In both cases, the hole cannot move in a loop, for this is not possible on the Bethe lattice or forbidden in the SAW approximation on the square lattice. Both spectra were calculated with magnon-magnon interactions included ($\lambda = 1$). Thus the only difference can come from the existence of tangential paths on the square lattice.

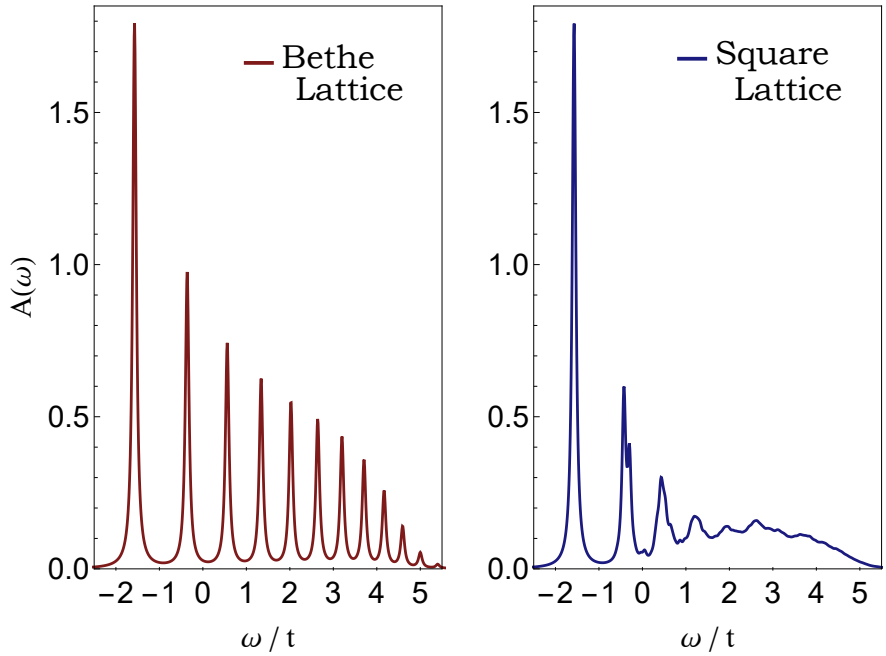

Figure 3.9: Specral function of a single hole in the t–J^z model on the Bethe lattice (left panel) and the square lattice within SAW approximation (right panel). Data were obtained for the canonical value of the coupling constant $J = 0.4t$. Both spectra were calculated with magnon-magnon interactions (and proximity effect) included ($\lambda = 1$). Figure taken from Ref. [80].

There are a few cases to explore. First, we can ask if the incoherent spectrum appears also without interactions on the square lattice. As shown in Fig. 3.10, this is not the case. Although the square lattice geometry leads to the appearance of new small peaks, those do not merge into a continuum. There needs to be a medium in the system that would *feel* this geometry. It turns out that the proximity effect (hole-magnon interaction) only quantitatively affects the spectrum—see the small difference between light and darker lines in Fig. 3.10. This is because a single hole may only interact with a relatively small number (up to 4) of magnons. (Though the contribution from hole-magnon interaction could become relevant for finite dopings.) However, in our case, we can see the incoherence is induced by the magnon-magnon interactions (see Fig. 3.10, blue data). In the end, we can conclude the combination of square lattice geometry with the magnon-magnon interactions leads to the appearance of the incoherent continuum in the spectral function of a single hole in the 2D t–J^z model. In other words, the mere interactions along the path of the hole would not be sufficient to produce the continuum and the interactions perpendicular to the path also need to be included.

Last but not least, let us comment on the intuitive understanding of the onset of the continuum in the investigated model. First, let us understand what makes the spectrum

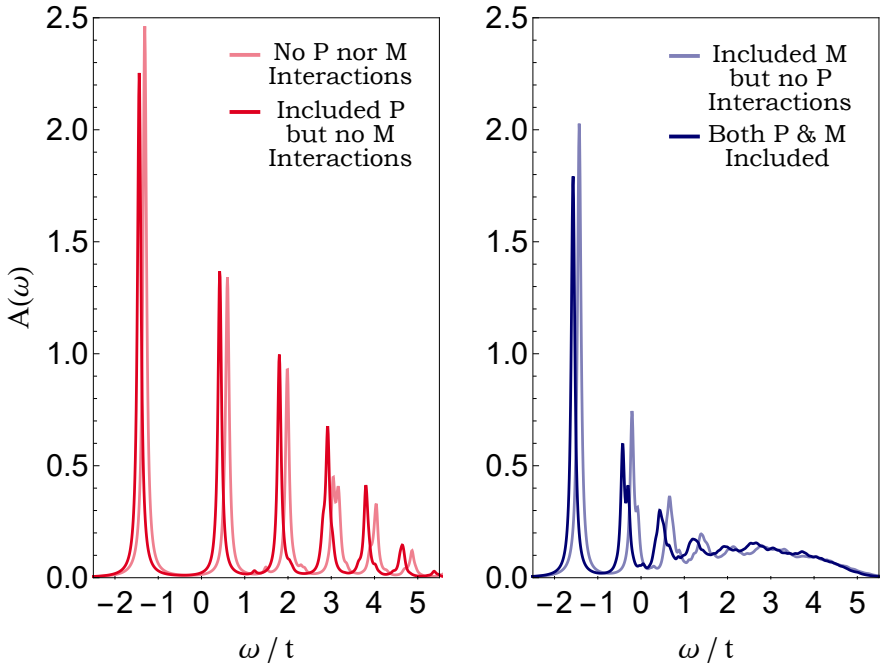

Figure 3.10: Specral function of a single hole in the t–J^z model on the square lattice within SAW approximation calculated for different combinations of proximity (P) and magnon-magnon (M) interactions. The left panel (red lines) shows results without magnon-magnon interactions, right panel (blue lines) shows spectra with magnon-magnon interactions included. Notice the qualitative difference between the shape of the spectra on the left panel versus the right panel. Data without the proximity effect is shown with lighter lines while the ones that include the proximity effect are darker in color. Figure taken from Ref. [80].

so coherent in the case of the Bethe lattice. The reason behind such coherence is the incredibly high symmetry of the problem. We stated in Eq. (3.8) that on the Bethe lattice, all the states with the same number of magnons have the same energy (in a sense of the expectation value of $\hat{\mathcal{H}}_J$). For this reason, the states with the same number of magnons are indistinguishable on the Bethe lattice (see Fig. 3.5) and thus contribute to the same quasiparticle peaks (i.e. at the same energies). This symmetry is broken on the 2D square lattice. When magnons (or the hole) can interact perpendicularly to the path of the hole (i.e. when the path becomes tangential, see Fig. 3.3) the states with the same number of magnons become distinguishable—they may have different energies (see Fig. 3.6). The number of bonds where the path can become tangential grows with the length of the path. This leads to a massive splitting of the peaks in the spectrum. In this sense, although we call the observed incoherence a continuum, the continuum may formally appear only in the thermodynamic limit.

3.4. Conclusions

The spectral function of a single hole in the t–J^z model on a 2D square lattice contains a broad incoherent part and thus qualitatively differs from the ladder-like spectral function obtained for the Bethe lattice (or using SCBA, cf. Fig. 2.5 and 3.2). We develop a self-avoiding walks approximation (see Sec. 3.2.1) that can capture the geometry of the square lattice while allowing us to rule out the motion of the hole in a loop. The

spectral function $A(\omega)$ of a single hole within the SAW approximation agrees very well with the exact diagonalization results for all studied couplings $J/t \geq 0.4$, see Fig. 3.7. This *a posteriori* justifies the neglection of the Trugman loops in the SAW approximation.

We show that the magnon-magnon interactions are responsible for the collapse of the ladder spectrum when going from the Bethe lattice to the 2D square lattice for $J/t \geq 0.4$, see Fig. 3.9 and 3.10. This is because the discrete linear potential the hole is subject to on the Bethe lattice is substantially warped (cf. Fig. 3.5 and 3.6) when magnons can interact along tangential bonds of the path of the hole on the square lattice, see Fig. 3.3. Such interaction, on the other hand, cannot be realized on the Bethe lattice, cf. Fig 3.4. This shows that often neglected magnon-magnon interactions can play an important role also in 2D systems.

Chapter 4

Beyond vibrational modes in the 2D t–J^z model

Based on Piotr Wrzosek, Krzysztof Wohlfeld, Eugene Demler, Annabelle Bohrdt, Fabian Grusdt, [in preparation].

In the previous chapters, we discussed in detail the spectral properties of a single hole introduced to either Bethe or square lattice with the energy of the system described by the t–J^z model. Up to this point, we only probed the subspace of the Hilbert space where the hole does not acquire any phase when propagating through the system. This follows from the fact that in the Hamiltonian of the t–J^z model, the hopping term does not depend on the direction of the propagation. But at the same time, it may lead to a situation where only a certain subspace of the Hilbert space can be measured by the spectral function while many eigenstates of the system remain invisible. In this chapter, we want to address this concern and show that indeed apart from the continuum of states formed due to the magnon-magnon interactions, one can expect to find the so-called vibrational and rotational modes of the hole in t–J^z model. While the vibrational modes are the well-known class of states with the distance between energy levels scaling as $(J/t)^{2/3}$ [52], the lowest rotational excitations possess an approximately linear behavior in J/t [55, 68].

We will explain the origin of this linear behavior by introducing a simple yet realistic toy model which connects some of the aspects of the physics of the t–J^z model on the Bethe and square lattices. Further, we will observe and explain why the vibrational and rotational modes live in the orthogonal subspaces on the Bethe lattice though they hybridize on the square lattice. Note that rotational modes are present in the spectral functions shown in the previous Ch. 3. But they carry a relatively small portion of the spectral weight and are mostly hidden in the continuum of states from the magnon-magnon interactions which makes them difficult to resolve and study directly.

4.1. Evolution of the spectral function $A(\omega)$ upon changing the coupling strength J/t

In the beginning, let us observe how varying the coupling constant J influences the spectra of a single hole in the t–J^z model on the square lattice and on the Bethe lattice. The results (including magnon-magnon interactions) are shown in Fig. 4.1. Noticeably, in the square lattice case [Fig. 4.1.(a)] one can observe the broad continuum covering

details of the spectrum at higher energies (see Ch. 3 for details). Nevertheless, some of the fundamental excitations that can be seen in the Bethe lattice result [Fig. 4.1.(b)] are still well visible when the square lattice is considered. These excitations are characterized by the well-known scaling behavior of $(J/t)^{2/3}$ [52]. This type of scaling naturally appears for the problem of a single particle in the triangular well—which is the continuum limit of the single hole in the t–J^z model on the Bethe lattice [69, 82]. This comes from the fact that the hole moving on the Bethe lattice excites magnons that cost constant energy. This in return leads to the formation of an effective discrete linear potential acting on the hole. Since those $\sim (J/t)^{2/3}$ excitations correspond to the vibrations of the spin polaron we call them vibrational modes [55, 68].

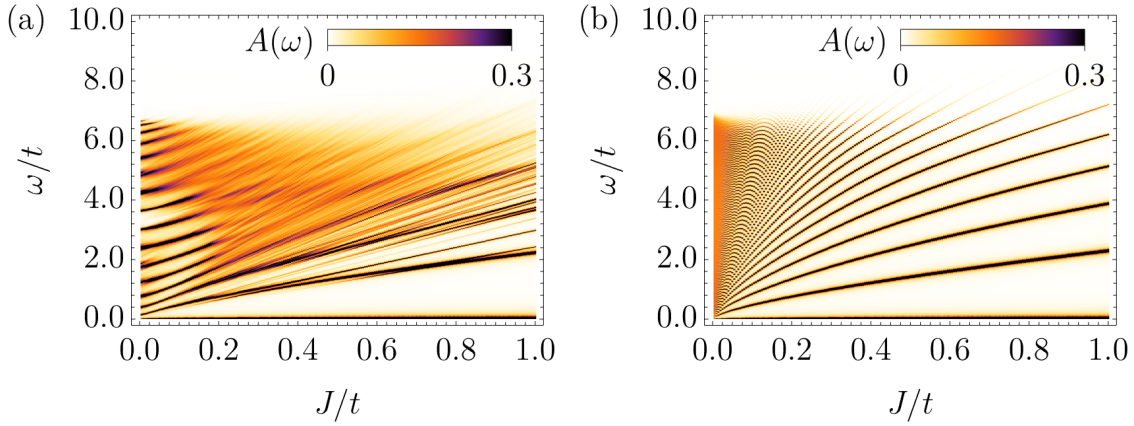

Figure 4.1: Evolution of the spectral function $A(\omega)$ [Eq. (2.3)] of a single hole in the t–J^z model (1.25) upon changing J/t: (a) on a square lattice and (b) on the Bethe lattice. All results for the "genuine" t–J^z model, i.e. magnon-magnon interactions are included. Square lattice results are obtained within self-avoiding walks approximation (see Ch. 3) while Bethe lattice results are exact analytical calculations (see Sec. 2.2). The $\omega = 0$ energy level is chosen as the ground state of the system for every respective value of coupling constant J. Results for $J/t < 0.2$ on the square lattice are not fully converged (especially for higher energies ω/t).

Apart from the continuum of states and the vibrational modes, in the square lattice case, in Fig. 4.1.(a) we can notice the existence of some other states that do not seem to follow the $\sim (J/t)^{2/3}$ scaling behavior. Encouraged by such a possibility we decide to remove the magnon-magnon interactions from the considerations to see if there are indeed states with different behavior whose origin is not connected to the magnon-magnon interactions. The results are shown in Fig. 4.2. This time we can explicitly see that the spectrum of a single hole on the square lattice consists of more than just vibrational modes. The set of peaks with apparently linear scaling with J/t is clearly visible in Fig. 4.2.(a). At the same time, in the Bethe lattice case [Fig. 4.2.(b)] only the vibrational excitations $\sim (J/t)^{2/3}$ can be observed.

A closer look at the spectral function on the square lattice leaves us with yet another information. The vibrational modes and the new linear peaks do not cross. Instead, they hybridize when energy is sufficiently close leading to an anticrossing behavior. The crossing of the energy level would on the other hand require the two types of states to reside in orthogonal subspaces. In such case the picture would look like in the Bethe case result with only one type of peaks visible. This could also mean that the new linear states are also present on the Bethe lattice, we just cannot probe them with

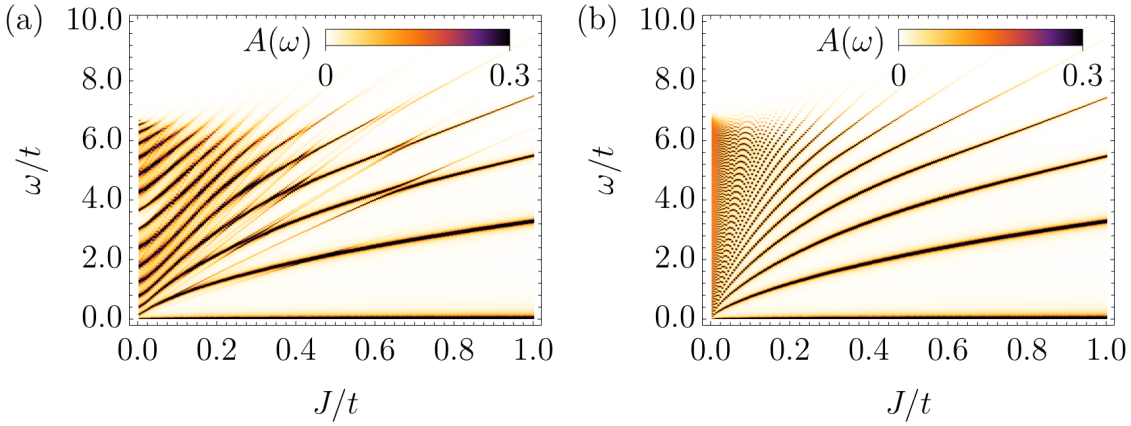

Figure 4.2: Evolution of the spectral function $A(\omega)$ [Eq. (2.3)] of a single hole in the t–J^z model (1.26) without magnon-magnon interactions (i.e. $\lambda = 0$) upon changing J/t: (a) on a square lattice and (b) on the Bethe lattice. Square lattice results are obtained within self-avoiding walks approximation (see Ch. 3) while Bethe lattice results are exact analytical calculations (see Sec. 2.2). The $\omega = 0$ energy level is chosen as the ground state of the system for every respective value of coupling constant J. Results for $J/t < 0.2$ on the square lattice are not fully converged (especially for higher energies ω/t).

the standard spectral function $A(\omega)$ of a single hole. And indeed, as shown before [68], there exist rotational excitations that can be probed by introducing the hole with non-zero angular momentum to the system. Some of them can be characterized by linear-like energy scaling with J/t. Those rotational modes on the Bethe lattice seem to be the key to understanding the onset of linear peaks in the spectral function $A(\omega)$ of a single hole on the square lattice.

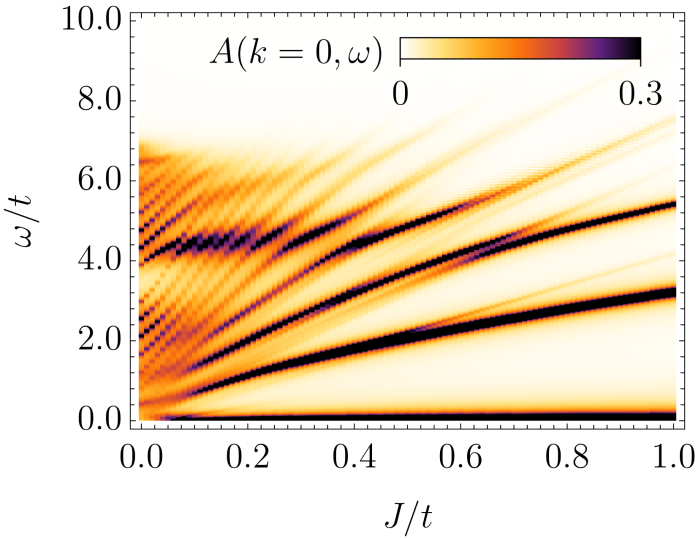

Figure 4.3: Evolution of the spectral function $A(k = 0, \omega)$ [Eq. (1.2)] of a single hole in the t–J^z model (1.26) on the square lattice without magnon-magnon interactions (i.e. $\lambda = 0$) upon changing the coupling constant J/t. Results were obtained using exact diagonalization for the square lattice with 20 sites.

To even further confirm the presence of the linear-like states in the spectral function $A(\omega)$ [Eq. (2.3)] of a single hole in the t–J^z model on a square lattice we perform an exact diagonalization study on a small lattice. Here we neglect the magnon-magnon interaction, otherwise, the continuum of states would cover the part of physics we are interested in. The result is shown in Fig. 4.3. The spectrum (Fig. 4.3) qualitatively agrees with our finding based on the SAW approximation (Fig. 4.2) confirming that the vibrational and rotational modes of a hole hybridize on the square lattice—as reflected by visible anticrossing between states of the $(J/t)^{2/3}$ and (J/t) behavior.

4.2. Green's function with rotational degrees of freedom

In this and the following Sec. 4.3 we will slightly divert from the original question. We will first introduce the Green's function with rotational degrees of freedom and study spectral functions of the single hole with non-zero angular momentum in the t–J^z model on a square lattice and on the Bethe lattice. This will give us a useful notation for later discussion as well as it will provide us with an initial intuition about the rotational modes of the hole. Only then we will come back to the original question concerning linear energy scaling of the rotational modes and mixing of the rotational and vibrational excitations on the square lattice.

To understand the nature of rotational excitations we start by generalizing the single-particle Green's function $G(\omega)$ to the single-particle Green's function with rotational degrees of freedom. We will refer to this new function as *rotational* Green's (or spectral) function $G_{M_n}(\omega)$. Using the polaronic language it may be defined as,

$$G_{M_n}(\omega) = \langle \varnothing | \hat{R}_{M_n} \hat{G}(\omega) \hat{R}^\dagger_{M_n} | \varnothing \rangle, \tag{4.1}$$

with the Green's operator defined in a standard way $\hat{G}(\omega) = \left(\omega - \hat{\mathcal{H}}_{t\text{–}J^z} + E_\varnothing\right)^{-1}$. Note that here we used $\hat{\mathcal{H}}_{t\text{–}J^z}$ [Eq. (1.25)] in the definition of the Green's operator $\hat{G}(\omega)$, but all the following deriviations are valid also for $\hat{\mathcal{H}}_{t\text{–}J^z}(\lambda)$ [Eq. (1.26)]. Within the self-avoiding walks approximation the operator

$$\hat{R}^\dagger_{M_n} = \frac{1}{\sqrt{|\mathcal{S}(n)|}} \sum_{\eta \in \mathcal{S}(n)} \mathcal{P}^\eta_{M_n} \hat{a}^\dagger_{\eta(0)} \hat{a}^\dagger_{\eta(1)} \dots \hat{a}^\dagger_{\eta(n-1)} \hat{h}^\dagger_{\eta(n)}, \tag{4.2}$$

creates a normalized linear combination of states where the hole is introduced to the lattice at a certain site $\eta(0)$ (exact position is not important) and then propagated n times without returning through all possible self-avoiding paths $\eta \in \mathcal{S}(n)$. When $n = 0$ the above-defined expression for $G_{M_n}(\omega)$ reduces to the (standard) Green's function $G(\omega)$ of a single hole discussed in the previous chapters.

Here $M_n = [m^{(1)}, m^{(2)}, \dots, m^{(n)}]$ such that with k^{th} hop the hole acquires an angular momentum proportional to $M_n(k)$. The product of phase factors $\mathcal{P}^\eta_{M_n}$ is given by,

$$\mathcal{P}^\eta_{M_n} = \prod_{k=1}^{n} \exp\left(-i\phi^{(k)}_\eta m^{(k)}\right), \tag{4.3}$$

where phase $\phi^{(k)}_\eta$ depends on the number of possible self-avoiding paths from position $\eta(k-1)$ as well as on the direction of the propagation d_k at k^{th} step. For $z = 4$ lattices

a convenient rule is to set $d_{k>1}$ such that it is 0 if the hole does not turn with respect to the previous move, 1 when the hole turns left, and 2 when the hole turns right, see Fig. 4.4. Formally, we can write,

$$\phi_\eta^{(k)} = \frac{2\pi}{|\mathcal{A}(\eta_{k-1})|} d_k, \tag{4.4}$$

where η_{k-1} is a subpath of $\eta \equiv \eta_n$ consisting of $k-1$ first moves of the hole and $\mathcal{A}(\eta_{k-1})$ returns a set of self-avoiding paths $\eta_k = (\eta_{k-1}, d_k)$ which are superpaths of η_{k-1} extended by the move in direction d_k. Note that not all directions d_k may be possible within SAW approximation and only one of them will lead to η_k which is a subpath of η. We will also set $\eta_0 = 0$ such that $|\eta_0\rangle \equiv |0\rangle$ is the initial state—consistently with the notation in the previous chapters.

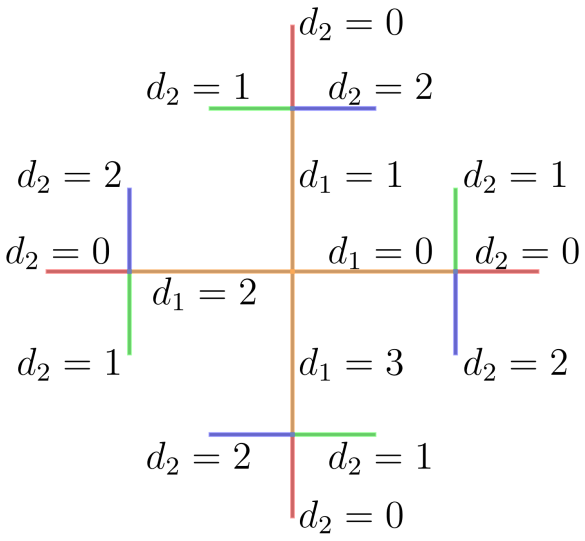

Figure 4.4: Part of a $z = 4$ lattice (square or Bethe) with denoted coefficients d_k for each path of the hole that determines the contributions to angular momentum for calculations of the rotational Green's function, see the text for further details.

4.2.1. An explicit expression for the rotational Green's function

Now when the rotational Green's function $G_{M_n}(\omega)$ is defined we want to find the general expression for it within the assumed self-avoiding walks approximation (which is going to yield the exact result for the Bethe lattice case). As we know from the previous chapter it is quite straightforward to calculate the diagonal coefficients of the single-particle Green's function (even on the square lattice). There we just needed the top-left one, but by simply reordering the basis any diagonal coefficient can be found with ease. Here, on the other hand, the operator $\hat{R}^\dagger_{M_n}$ performs a sum over all paths $\eta \in \mathcal{S}(n)$, thus we need to be able to include also the off-diagonal coefficients. With some careful consideration, even this can be done leading to a quite complicated but very beautiful recursive formula, Eq. (4.17).

We start by denoting,

$$|\eta \equiv \eta_n\rangle = \hat{a}^\dagger_{\eta(0)} \hat{a}^\dagger_{\eta(1)} \dots \hat{a}^\dagger_{\eta(n-1)} \hat{h}^\dagger_{\eta(n)} |\varnothing\rangle. \tag{4.5}$$

This way we can rewrite (4.1) as,

$$G_{M_n}(\omega) = \frac{1}{|\mathcal{S}(n)|} \sum_{\eta',\eta \in \mathcal{S}(n)} \mathcal{P}_{M_n}^{\eta',\eta} G_{\eta',\eta}(\omega), \tag{4.6}$$

where $\mathcal{P}_{M_n}^{\eta',\eta} = \mathcal{P}_{M_n}^{\eta'*} \cdot \mathcal{P}_{M_n}^{\eta}$ and the coefficients that we need to find expression for are given by,

$$G_{\eta',\eta}(\omega) = \langle \eta' | \hat{G}(\omega) | \eta \rangle. \tag{4.7}$$

Let $\mathcal{B}$ stand for the basis of all possible states $|\eta\rangle$ within self-avoiding walks approximation. With the cofactor matrix method [83] of calculating determinants, the above coefficient $G_{\eta',\eta}(\omega)$ can be expressed as a particular entry of the matrix,

$$M(\hat{G}(\omega))_{\mathcal{B}}^{\mathcal{B}} = \frac{C^T(\omega)}{\det M(\hat{H}(\omega))_{\mathcal{B}}^{\mathcal{B}}}, \tag{4.8}$$

where C^T is adjugate [83] of $M(\hat{G}(\omega))_{\mathcal{B}}^{\mathcal{B}}$ and,

$$\hat{H}(\omega) = \hat{G}(\omega)^{-1} = \omega - \hat{\mathcal{H}}_{t\text{-}J^z} + E_{\varnothing}. \tag{4.9}$$

Let us now proceed to present a general scheme for deriving the final formula. From the above, we see that a single coefficient $G_{\eta',\eta}(\omega)$ is a ratio of two determinants. The determinant in the numerator is almost the same as the one in the denominator but with the row corresponding to state η and column corresponding to state η' removed. Since we consider either Bethe lattice or square lattice with self-avoiding walks approximation the structure of matrix $M(\hat{H}(\omega))_{\mathcal{B}}^{\mathcal{B}}$ can be described as block recursive—two distinct blocks are coupled to a top-left component of a superblock they belong to. To better grasp how such a matrix may look like have a look at the Eq. (4.10).

$$\det \mathcal{M}(\hat{H}(\omega))_{\mathcal{B}}^{\mathcal{B}} = \det H^{(0)}(\omega) =$$

$$\left|\begin{array}{c|c|c|c|c} \omega - 2J & t \;\; 0 \;\; \cdots & t \;\; 0 \;\; \cdots & t \;\; 0 \;\; \cdots & t \;\; 0 \;\; \cdots \\ \hline \begin{array}{c} t \\ 0 \\ \vdots \end{array} & H^{(1)}(\omega) & 0 & 0 & 0 \\ \hline \begin{array}{c} t \\ 0 \\ \vdots \end{array} & 0 & H^{(1)}(\omega) & 0 & 0 \\ \hline \begin{array}{c} t \\ 0 \\ \vdots \end{array} & 0 & 0 & H^{(1)}(\omega) & 0 \\ \hline \begin{array}{c} t \\ 0 \\ \vdots \end{array} & 0 & 0 & 0 & H^{(1)}(\omega) \end{array}\right| . \tag{4.10}$$

In general, the matrix $H^{(k-1)}(\omega)$ is a block recursive and composed of 4 or fewer matrices $H^{(k)}_{\eta_k}(\omega)$ (which do not have to be the same, hence dependence on path η_k) connected by the off-diagonal coefficients in the top row / left-most column. Such structure is a natural consequence of the lack of loops in either the Bethe lattice or self-avoiding walks approximation on the square lattice.

$$\det H^{(0)}(\omega) =$$

$$\begin{vmatrix} G_0(\omega)^{-1} - \Sigma(\omega) & 0 & 0 & 0 & 0 \\ \hline t \\ 0 \\ \vdots & T^{(1)}_{(0,0)}(\omega) & 0 & 0 & 0 \\ \hline t \\ 0 \\ \vdots & 0 & T^{(1)}_{(0,1)}(\omega) & 0 & 0 \\ \hline t \\ 0 \\ \vdots & 0 & 0 & T^{(1)}_{(0,2)}(\omega) & 0 \\ \hline t \\ 0 \\ \vdots & 0 & 0 & 0 & T^{(1)}_{(0,3)}(\omega) \end{vmatrix} . \tag{4.11}$$

Importantly, we can notice that if matrix $H^{(1)}(\omega)$ was in lower (or upper) triangular form, we could easily bring the matrix $H^{(0)}(\omega)$ to the triangular form as well. The same applies in general to matrix $H^{(k)}(\omega)$. By fixing the maximum depth of the lattice as n we see that the matrix $H^{(n)}(\omega)$ is a 1×1 matrix, which is triangular. Thus we can recursively bring the whole matrix $H^{(0)}(\omega)$ to a triangular form and read out the determinant as the product of the diagonal elements. In the end, by taking the limit of $n \to \infty$ one obtains Eq. (4.11). Note that, all four matrices $T^{(1)}_{\eta_1}(\omega)$ are the same due to the 4-fold rotational symmetry around the origin of the lattice (i.e. where we introduce the hole). We can also shortly write,

$$\det M(\hat{H}(\omega))^{\mathcal{B}}_{\mathcal{B}} = \left(G_0(\omega)^{-1} - \sum_{\eta_1 \in \mathcal{A}(0)} \Sigma_{\eta_1}(\omega) \right) \prod_{\eta_1 \in \mathcal{A}(0)} \det T^{(1)}_{\eta_1}(\omega), \tag{4.12}$$

where for $k > 0$,

$$\det T^{(k)}_{\eta_k}(\omega) = \left(G_{\eta_k}(\omega)^{-1} - \sum_{\eta_{k+1} \in \mathcal{A}(\eta_k)} \Sigma_{\eta_{k+1}}(\omega) \right) \prod_{\eta_{k+1} \in \mathcal{A}(\eta_k)} \det T^{(k+1)}_{\eta_{k+1}}(\omega). \tag{4.13}$$

An abbreviation for the diagonal coefficient corresponding to path η_k is simply,

$$G_{\eta_k}(\omega)^{-1} = \langle \eta_k | (\omega - \hat{\mathcal{H}}_z) | \eta_k \rangle, \tag{4.14}$$

and the self-energy of the subsystem of superpaths of path η_k is given by the following recurrence relation,

$$t^2\Sigma_{\eta_k}(\omega)^{-1} = G_{\eta_k}(\omega)^{-1} - \sum_{\eta_{k+1}\in\mathcal{A}(\eta_k)} \Sigma_{\eta_{k+1}}(\omega). \tag{4.15}$$

Additionally, let us define,

$$\Gamma^{\Delta}_{\eta_k}(\omega) = G_{\eta_k}(\omega)^{-1} - \sum_{\eta_{k+1}\in\Delta} \Sigma_{\eta_{k+1}}(\omega), \tag{4.16}$$

where $\Delta \subset \mathcal{A}(\eta_k)$.

The last part is to calculate the coefficient of C^T which is the determinant of the $M(\hat{H}(\omega))^{\mathcal{B}}_{\mathcal{B}}$ with row and column corresponding to states η and η' removed. If $\eta \neq \eta'$ then the resulting matrix is in imbalanced form, where some of the previously diagonal terms are now located outside the diagonal. First, we bring them back to the diagonal by simply shifting sequentially the column corresponding to the removed row until it is located in the first column and then the row corresponding to the removed column to the first row (remembering about the sign change of the determinant when transposing rows or columns). Then we follow the scheme analogous to the described above for the matrix $M(\hat{H}(\omega))^{\mathcal{B}}_{\mathcal{B}}$. In the end, we divide the two results to simply find out that almost all terms $\det T^{(k)}_{\eta_k}(\omega)$ reduce yielding a final formula. Given path $\eta' = \eta'_l$ of length l and path $\eta = \eta_r$ of length r it reads,

$$G_{\eta'_l,\eta_r}(\omega) = (-t)^{r+l-2c} \cdot \frac{\prod_{k=0}^{c-1}\left(\Gamma^{\mathcal{A}(\eta_k)\setminus\{\eta_{k+1}\}}_{\eta_k} - \underset{n=k+1}{\overset{c-1}{\mathcal{K}}} \frac{t^2}{\Gamma^{\mathcal{A}(\eta_n)\setminus\{\eta_{n+1}\}}_{\eta_n}}\right)}{\left(\prod_{k=0}^{c}\Gamma^{\mathcal{A}(\eta_k)}_{\eta_k}\right)\left(\prod_{k=c+1}^{r}\Gamma^{\mathcal{A}(\eta_k)}_{\eta_k}\right)\left(\prod_{k=c+1}^{l}\Gamma^{\mathcal{A}(\eta'_k)}_{\eta'_k}\right)}, \tag{4.17}$$

where for all $j < c$ subpaths are identical, $\eta'_j = \eta_j$, and either one path is the subpath of the other, $\min(l, r) = c$, or they diverge after c steps, $\eta'_{c+1} \neq \eta_{c+1}$. Here $\mathcal{K}$ denotes a continued fraction expansion. To shorten the notation, the dependence of the Γ functions on ω is not written explicitly.

An important thing to notice is that Eq. (4.17) is fully determined by the diagonal terms of the model Hamiltonian and the geometry of the lattice since together they determine Eqs. (4.15) and (4.16). After small modifications, one can calculate Eqs. (4.15) and (4.16) numerically using the same idea as for calculating the standard Green's function of a single hole within SAW approximation on a square lattice described in the previous Ch. 3. Then the result can be used to evaluate Eq. (4.17). The only difficulty here is that the number of $G_{\eta',\eta}$ terms one needs to calculate to obtain the rotational spectral function $G_{M_n}(\omega)$ grows exponentially with n, thus it is advisable to take advantage of the geometric symmetries of the system.

4.2.2. Graph representation

At the first sight, Eq. (4.17) for $G_{\eta',\eta}(\omega)$ may look quite complicated. But there is a comprehensive way to represent this equation in terms of simple diagrams. In order to do it, one needs to follow a set of simple rules for creating such diagrams. We list them below.

1. Each node represents a given state $|\eta_k\rangle$ of the system and it is labeled with its corresponding weight $\Gamma_{\eta_k}^{\mathcal{A}(\eta_k)}$.

2. If there is more than a single node in the diagram then each node has to be connected to some other node either with a single or a double edge.

3. Each edge ends with an arrow denoting the direction of the hole motion (i.e. the order in which the hole traveled through bonds in directions $d_1, d_2, \ldots$) in state $|\eta'\rangle$ or $|\eta\rangle$.

4. Single edges denote subpaths distincts in states $|\eta'\rangle$ and $|\eta\rangle$. Each shall be labeled with weight $-t$ as it adds a factor of $-t$ to the whole solution.

5. Double edges stand for the common parts of the path in states $|\eta'\rangle$ and $|\eta\rangle$. Double edge starting from the node denoted with $\Gamma_{\eta_k}^{\mathcal{A}(\eta_k)}$ is denoted with $\Gamma_{\eta_k}^{\mathcal{A}(\eta_k)\setminus\{(\eta_k,d_{k+1})\}}$ where d_{k+1} is chosen such that (η_k, d_{k+1}) is a subpath of η (and η').

To see how the above works in practice, let us relate the expressions for some particular coefficients $G_{\eta',\eta}(\omega)$ to their respective diagrams. First, the standard local Green's function can be written as,

$$G(\omega) = G_{0,0}(\omega) = \frac{1}{\Gamma_0^{\mathcal{A}(0)}(\omega)}, \tag{4.18}$$

or expressed through the simplest diagram.

Taking $d_1 = 0 = d_2$ and $\eta = ((0, d_1), d_2)$ one obtains a path where the hole moved twice to the east, see Fig. 4.4. Then for coefficient $G_{\eta,\eta}$ the diagram is as follows,

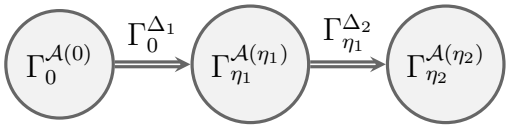

where $\Delta_1 = \mathcal{A}(0) \setminus \{\eta_1\}$ and $\Delta_2 = \mathcal{A}(\eta_1) \setminus \{\eta_2\}$. From this, we can read out the expression,

$$G_{\eta,\eta}(\omega) = \frac{\left(\Gamma_0^{\Delta_1} - \frac{t^2}{\Gamma_{\eta_1}^{\Delta_2}}\right)\Gamma_{\eta_1}^{\Delta_2}}{\Gamma_0^{\mathcal{A}(0)}\Gamma_{\eta_1}^{\mathcal{A}(\eta_1)}\Gamma_{\eta_2}^{\mathcal{A}(\eta_2)}}. \tag{4.19}$$

Similarly for $G_{\eta',\eta}$, where $\eta' = ((0,0),1)$ and η as before,

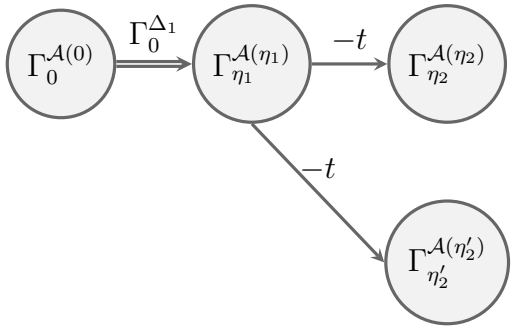

the formula obtained from the diagram reads,

$$G_{\eta',\eta}(\omega) = \frac{t^2 \Gamma_0^{\Delta_1}}{\Gamma_0^{\mathcal{A}(0)} \Gamma_{\eta_1}^{\mathcal{A}(\eta_1)} \Gamma_{\eta_2}^{\mathcal{A}(\eta_2)} \Gamma_{\eta_2'}^{\mathcal{A}(\eta_2')}}. \tag{4.20}$$

By comparing the above formulae with Eq. (4.17) one can see that the node weights are simply multiplied in the denominator. For every single edge, one multiplies the solution by $-t$. And the double edges give rise to a product of continued fractions of diminishing depths in the numerator.

4.3. Rotational spectral function $A_{M_n}(\omega)$

With the method we developed, we can now calculate and plot rotational spectral functions for the t–J^z model (1.26) (with or without magnon-magnon interactions),

$$A_{M_n}(\omega) = -\frac{1}{\pi} \mathrm{Im}\, G_{M_n}(\omega + i0^+), \tag{4.21}$$

for different rotational degrees of freedom. Here we will investigate $n \leq 2$, i.e. spectra with up to two independent rotational degrees of freedom encoded by M_n. The corresponding initial state for such calculation is shown in Fig. 4.5. Since $n = 0$ corresponds

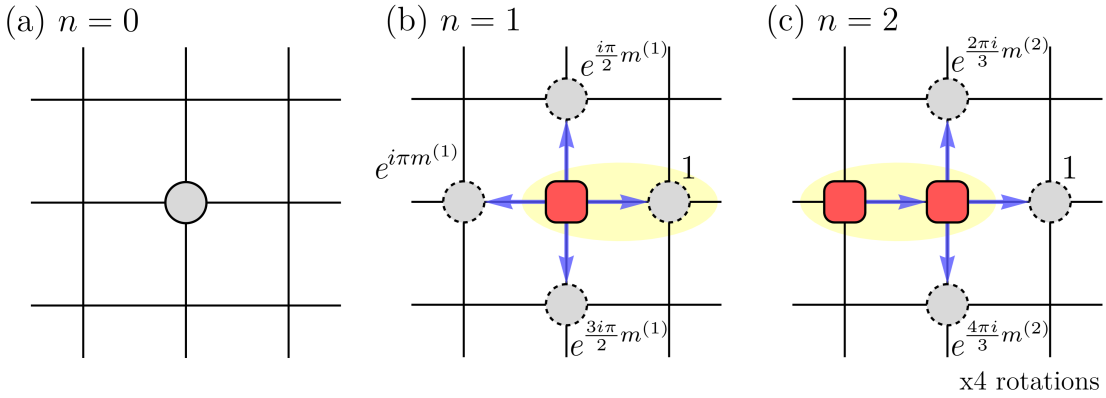

Figure 4.5: Cartoon picture of an initial state with (a) $n = 0$, (b) $n = 1$, and (c) $n = 2$ rotational excitations. The gray circle represents a hole while the red square (with rounded corners) stands for a magnon (string). The hole delocalized on multiple sites is denoted with dashed edges—it also means a sum over multiple configurations of the hole and magnons on the lattice: (b) 4 configurations and (c) 12 configurations. The yellow area covers the corresponding sites in panels (b) and (c). In panel (c) only one of four rotations around the origin is shown.

to the standard spectral function $A(\omega)$ shown in Fig. 4.1 (Fig. 4.2) with (without) magnon-magnon interactions respectively, we start by considering $n = 1$.

4.3.1. Spectral function with one rotational parameter (n = 1)

For $n = 1$ we have one rotational parameter, $M_1 = [m^{(1)}]$. The 4 possible values of $m^{(1)} \in \{0, 1, 2, 3\}$ come from 4 possible directions of the propagation of the hole from the initial site (see Fig. 4.4). For this reason, we will use the notation $m_4 \equiv m^{(1)}$

which makes the 4-fold rotation more transparent. Eq. (4.3) implies that $m_4 = 1$ and $m_4 = 3$ lead to the same solution. Moreover, within the SAW approximation (or on the Bethe lattice), the same applies to $m_4 = 2$ (it would not be the case if loops were allowed). Thus in Fig. 4.6 and Fig. 4.7 we present spectra that cover cases $m_4 = 0$ and $m_4 = 1, 2, 3$ respectively within SAW approximation.

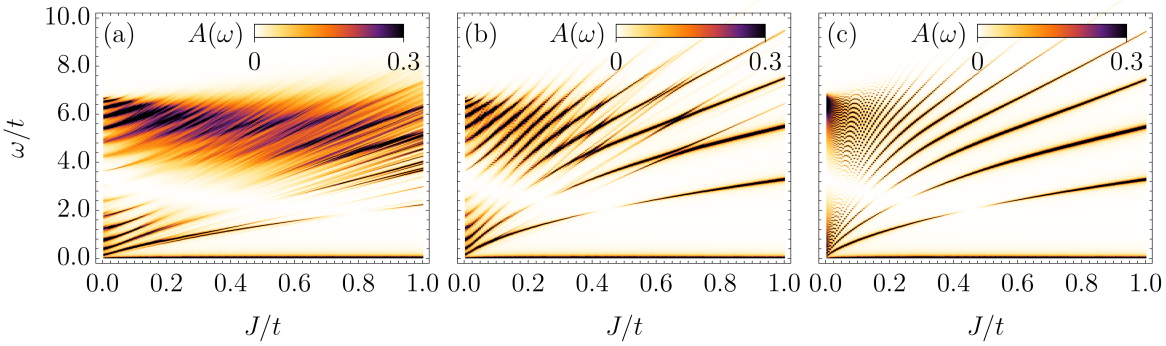

Figure 4.6: Case $m_4 = 0$. Evolution of the spectral function $A_{[m_4]}(\omega)$ of a single hole in the t–J^z model upon changing J/t: (a) on the square lattice with magnon-magnon interactions included, (b) on the square lattice without the magnon-magnon interactions, and (c) on the Bethe lattice also without the magnon-magnon interactions. The spectra are aligned such that the ground state of the system is located at $\omega = 0$ for every value of coupling constant J.

The case of $m_4 = 0$ shown in Fig. 4.6 qualitatively corresponds to the spectral function without rotational degrees of freedom (cf. Fig. 4.1 and 4.2). Since we did not introduce any angular momentum here ($m_4 = 0$), the initial state with the hole delocalized in four sites around the central site is achievable by acting once with the Hamiltonian on a state where the hole is put in the central site. For this reason, both the standard one and the rotational spectral function with $m_4 = 0$ probe the same subspace of the Hilbert space yielding the same set of peaks (see Fig. 4.1 and 4.2). Precisely, we can observe the continuum of states when magnon-magnon interactions are included on the square lattice [Fig. 4.6.(a)]; and even when magnon-magnon interactions are gone [Fig. 4.6.(b)] the spectrum contains states linear in J/t what stays in contrast to the Bethe lattice result [Fig. 4.6.(c)] where only vibrational $(J/t)^{2/3}$ modes can be observed.

The only visible difference between Fig. 4.6 and Figs. 4.1-4.2 is the distribution of the weight—rotational spectra in Fig. 4.6 have vanishing weight for certain energies ω. The exact position depends on the J/t ratio and the presence of the magnon-magnon interactions. But this is not a feature of the investigated model but rather a side-effect coming from destructive interference between the holes put in different sites around the origin of the lattice.

When $m_4 \neq 0$, as in Fig. 4.7, at first sight, it may look like not much has changed. But in fact, there is a significant difference here compared to the previous spectra (e.g. to Fig. 4.6). In Fig. 4.7 the lowest visible rotational excitation (lowest peak in the spectrum) visibly stems from the $(J/t)^{2/3}$ behavior and instead seems to be linear in J/t. Its slope (or derivative) appears to be roughly proportional to the cost of creating a magnon in the system. This is a crucial point here and we will investigate it closely in Sec. 4.4. But before this happens, let us also look at the spectral functions with more than two rotational degrees of freedom to gain even more intuition.

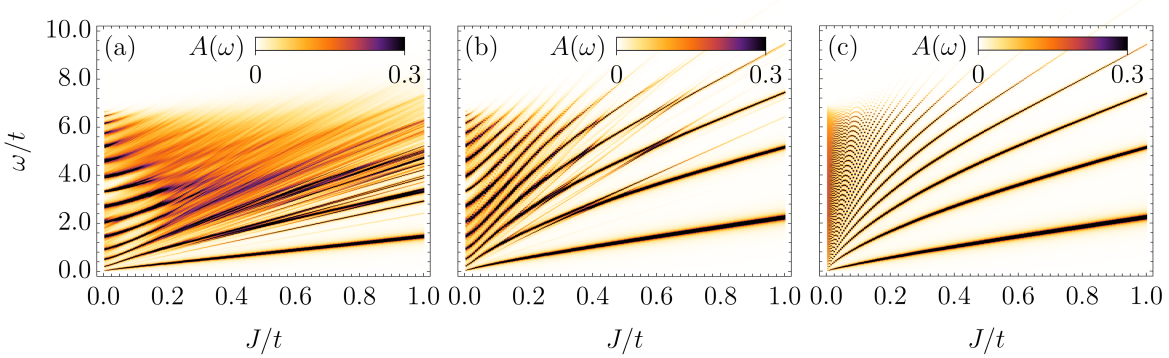

Figure 4.7: Case $m_4 = 1, 2$ or 3. Evolution of the spectral function $A_{[m_4]}(\omega)$ of a single hole in the t–J^z model upon changing J/t: (a) on the square lattice with magnon-magnon interactions included, (b) on the square lattice without the magnon-magnon interactions, and (c) on the Bethe lattice also without the magnon-magnon interactions. Alignment is the same as in Fig. 4.6.

4.3.2. Spectral function with two rotational parameters (n = 2)

For $n = 2$ we have two rotational parameters, $M_1 = [m^{(1)}, m^{(2)}]$. Since $m^{(2)} \in \{0, 1, 2\}$, we will use the notation $m_3 \equiv m^{(2)}$ from now on. Similarly to m_4, now $m_3 = 1$ and $m_4 = 2$ will lead to the same solution, as they correspond to rotations about the same angle but in opposite directions. Combining this with possible values of m_4 we see there are up to 4 distinct spectra we can obtain within SAW approximation. Again, taking both $m_4 = 0 = m_3$ does not differ from the standard spectral function qualitatively. By the same logic, $m_4 \neq 0 = m_3$ yields the result corresponding to the previous single rotation spectrum (Fig. 4.7) with $m_4 \neq 0$. And since spectra for $m_3 \neq 0$ are almost identical regardless of m_4, we show only the case of $m_4 = 1 = m_3$ in Fig. 4.8.

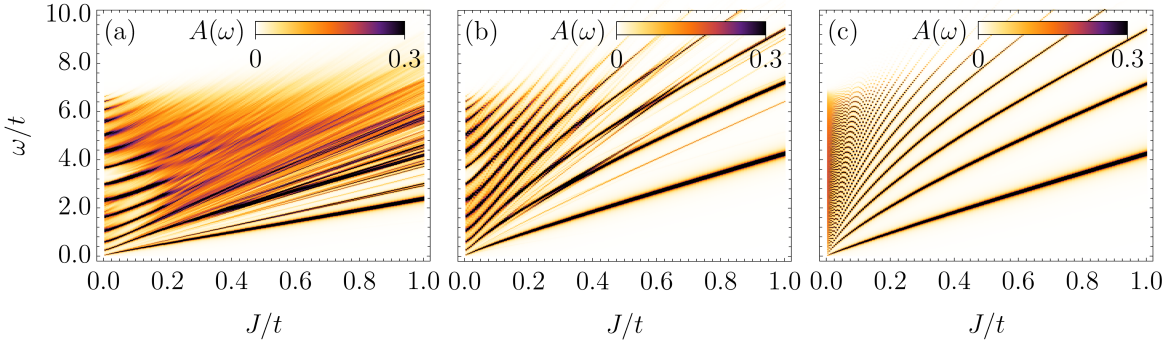

Figure 4.8: Case $m_4 = 1 = m_3$. Evolution of the spectral function $A_{[m_4,m_3]}(\omega)$ of a single hole in the t–J^z model upon changing J/t: (a) on the square lattice with magnon-magnon interactions included, (b) on the square lattice without the magnon-magnon interactions, and (c) on the Bethe lattice also without the magnon-magnon interactions. Alignment is the same as in Fig. 4.6.

In Fig. 4.8 we can see the lowest rotational excitation (lowest peak in the spectrum) also scales proportionally to J/t rather than $(J/t)^{2/3}$. Compared to the rotational spectral function $A_{[m_4=1]}(\omega)$ in Fig. 4.7, the slope (or derivative) is larger and it seems to be roughly equal to the cost of creating 2 magnons in the system. The most important notice is that this linear state coincides with a faint linear-like feature visible in the

standard spectral function that crosses the lowest vibrational excitation (see Fig. 4.2). Combining this with the fact that other linear features visible in Fig. 4.2 seem to be close in energy to $2, 3, 4$, etc. number of magnons we can conclude that these are most likely the lowest rotational modes of consecutively higher order rotational spectra.

4.4. Understanding of the onset of rotational states in the spectral function $A(\omega)$

As discussed so far, the lowest rotational excitations for different numbers of rotational parameters form a new class of states linear in J/t, and thus different from the well-known vibrational modes with $(J/t)^{2/3}$ scaling. Moreover, those excitations can be observed on the square lattice even without introducing rotational parameters, i.e. in the standard Green's function $A(\omega)$ [see e.g. Fig 4.2.(a)]. But for this to be possible the rotational and vibrational modes would have to hybridize on the square lattice. In this section, we will provide a comprehensive understanding of both, the linear energy scaling of those rotational modes and why they hybridize with vibrational modes on the square lattice but not on the Bethe lattice.

To this end, we will introduce a new basis of states—rotational basis—which will allow us to track rotational degrees of freedom more easily. This basis is defined for the Bethe lattice. We start by connecting the position notation introduced in Sec. 2.2 for the t–J^z model on a Bethe lattice defined in Eq. (2.22) with the path notation of this section defined in Eq. (4.5). Given a path $\eta \equiv \eta_n = ((...((0, d_1), d_2), ...), d_n)$ of length n, we can write

$$|\eta_n\rangle = |n; d_1, d_2, ..., d_n\rangle. \tag{4.22}$$

Then, we can introduce the rotational basis as defined below,

$$|n;\, m^{(1)}, m^{(2)}, ..., m^{(n)}\rangle_r = \frac{1}{\sqrt{4 \cdot 3^{n-1}}} \sum_{d_1=0}^{3} \sum_{d_2=0}^{2} \cdots \sum_{d_n=0}^{2} \exp\left(\frac{2\pi i}{4} d_1 m^{(1)}\right) \cdot ... \cdot \exp\left(\frac{2\pi i}{3} d_n m^{(n)}\right) |n; d_1, ..., d_n\rangle. \tag{4.23}$$

Since the possible values of $m^{(k)}$ and d_k parameters are the same, we add an index r to the states written in rotational basis to distinguish them from position basis. As one can see, the above is a one-to-one transformation from position to the rotational basis where Fourier transform with parameter $m^{(k)}$ has been performed for k-th hop of the hole. With the above notation, the initial states in Fig. 4.5 can be expressed simply as: (a) $|0\rangle_r$, (b) $|1; m^{(1)}\rangle_r$ and (c) $|2; m^{(1)}, m^{(2)}\rangle_r$. Also notice that $|0\rangle_r \equiv |0\rangle$.

4.4.1. Energy scaling $\propto J/t$ for the single hole in the t–J^z model on a square lattice

To understand why the lowest rotational excitations follow approximately $2nJ/t$ lines where $n = 1, 2, 3, ...$, let us see how the t–J^z model Hamiltonian on the Bethe lattice acts on two states: state with zero angular momentum $|n; 0, ..., 0, 0\rangle_r$ and state with non-zero angular momentum $|n; 0, ..., 0, 1\rangle_r$,

$$\begin{aligned} \hat{\mathcal{H}}_{t\text{–}J^z}|n; 0, ..., 0, 0\rangle_r &= E_n|n; 0, ..., 0, 0\rangle_r - t\sqrt{3}\left(|n-1; 0, ..., 0\rangle_r + |n+1; 0, ..., 0, 0, 0\rangle_r\right), \\ \hat{\mathcal{H}}_{t\text{–}J^z}|n; 0, ..., 0, 1\rangle_r &= E_n|n; 0, ..., 0, 1\rangle_r - t\sqrt{3}|n+1; 0, ..., 0, 1, 0\rangle_r. \end{aligned} \tag{4.24}$$

There is a significant difference between the two scenarios presented in Eq. (4.24). It turns out that non-zero $m^{(k)}$ makes it impossible to arrive at a state with a magnon count smaller than k. The reason is simple. When acting on the initial state with $m^{(k)} \neq 0$ (e.g. $|n;0,...,0,1\rangle_r$) with the Hamiltonian, the Fourier coefficients from the transformation to the rotational basis sum up to 0 for the hole moving in the direction of the k-th magnon if $m^{(k)} \neq 0$. Thus the k-th magnon effectively cannot be annihilated. It also makes the hole restricted to move only in a particular branch of the Bethe lattice (cf. Fig. 4.9).

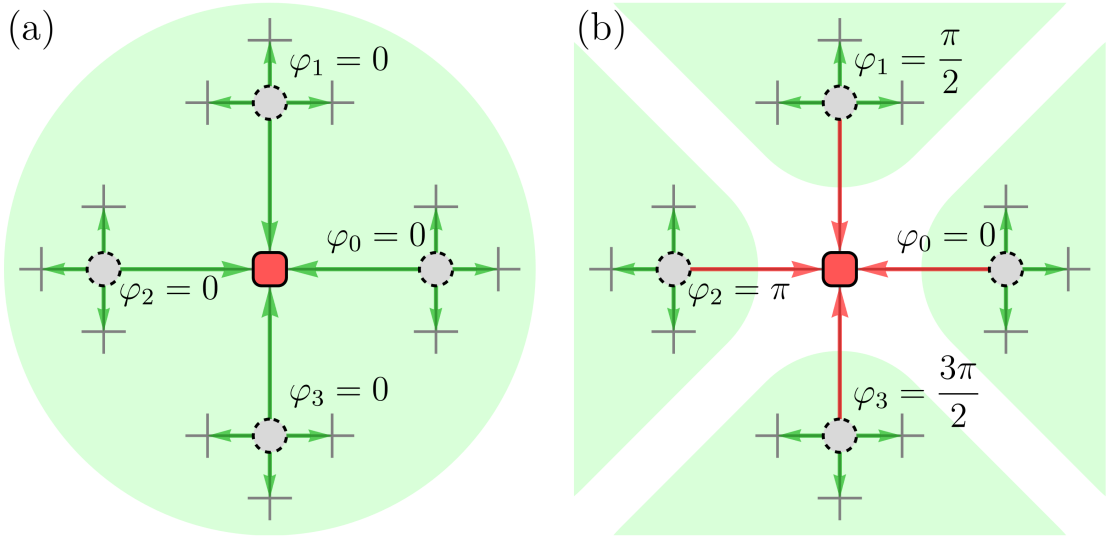

Figure 4.9: Cartoon picture of a single hole propagating through the Bethe lattice with energy described by the t–J^z model. The hole (gray circle) is initially introduced into the empty lattice and propagated once to the four nearest sites leaving behind a single magnon (red square with rounded corners): (a) without an angular momentum ($m_4 = 0 \Rightarrow \varphi_{d_1} = 0$), and (b) gaining an angular momentum ($m_4 = 1 \Rightarrow \varphi_{d_1} = \frac{\pi d_1}{2}$). This results in the initial states $|1;0\rangle_r$ and $|1;1\rangle_r$ presented in panels (a) and (b) respectively. The green background covers the sites which can be then reached by the hole while acting with the model Hamiltonian showing that non-zero angular momentum locks the hole in one of the branches of the Bethe lattice. Green arrows show the possible directions of the hole propagation while the red arrows in panel (b) show the moves that are effectively impossible due to the cancellation of the Fourier coefficients $\sum_{d_1=0}^{3} \exp(-i\varphi_{d_1}) = 0$, when $m_4 \neq 0$.

Let us now explicitly show how such an unremovable magnon leads to the approximately linear dependence of the energy of the lowest rotational excitation. We do it by expressing the rotational Green's function $G_{[1]}(\omega) \equiv {}_r\langle 1;1|\hat{G}(\omega)|1;1\rangle_r$ in terms of the standard Green's function of a single hole $G(\omega) = \langle 0|\hat{G}(\omega)|0\rangle$. To simplify the considerations, we neglect the magnon-magnon interactions. We can therefore write,

$$G(\omega)^{-1} = G_0(\omega)^{-1} - \Sigma(\omega), \tag{4.25}$$

where $G_0(\omega)^{-1} = \omega - 2J$ and,

$$\Sigma(\omega) = \frac{4t^2}{\omega - 4J - \frac{3}{4}\Sigma(\omega - 2J)}. \tag{4.26}$$

At the same time, we can use Eq. (4.17) to find out,

$$G_{[1]}(\omega)^{-1} = G_0(\omega - 2J)^{-1} - \frac{3}{4}\Sigma(\omega - 2J) = G(\omega - 2J)^{-1} + \frac{1}{4}\Sigma(\omega - 2J). \tag{4.27}$$

Moreover, if we modify the Bethe lattice such that at the origin the coordination number $z_0 = 3$ instead of 4 (let us keep the magnon energy untouched since its exact value is qualitatively not important), we would obtain,

$$G_{[1]}^{z_0=3}(\omega)^{-1} = G(\omega - 2J)^{-1}. \tag{4.28}$$

This way the rotational Green's function $G_{[1]}^{z_0=3}(\omega)^{-1}$ is equivalent to the standard one $G(\omega)$ but shifted in energy by the energy cost of one magnon, i.e. $2J$.

When the coordination number $z = 4$ everywhere, then the hole at the origin of the lattice has 4 possible paths to create a magnon, while for latter sites there are only 3 such possibilities—this introduces a small imbalance in the kinetic energy between the initial site and the other sites. In the end, this results in a small discrepancy from the exact linear dependence of the lowest rotational excitation [see Eq. (4.27) and Fig. 4.10]. Nevertheless, we can say that the major difference between the two Green's functions in Eq. (4.25) and Eq. (4.27) is the linear shift due to the cost of unremovable magnons. This also generalizes to higher rotational spectra, i.e. each approximately linear peak appears to be equivalent to the ground state of the system shifted by the cost of a certain number of unremovable magnons.

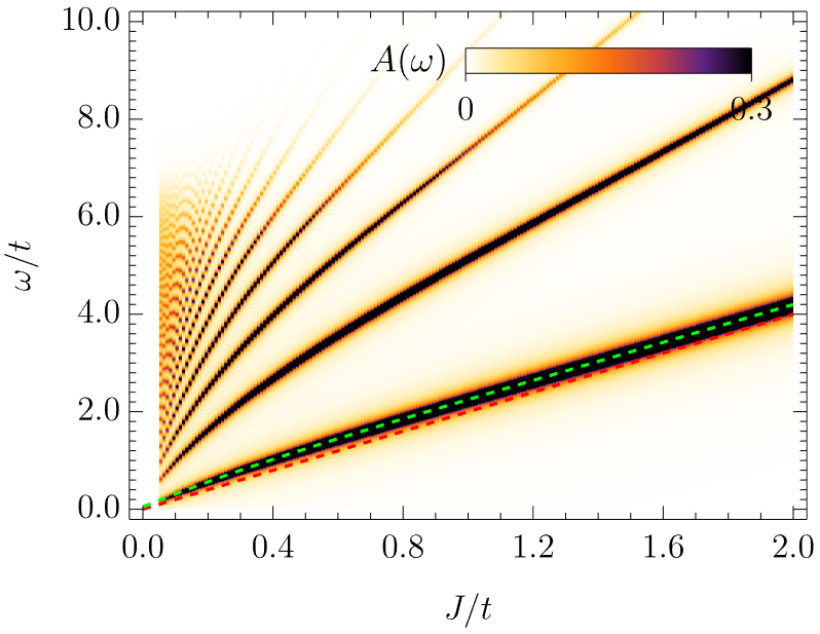

Figure 4.10: Evolution of the spectral function $A_{[1]}(\omega) = -\frac{1}{\pi}G_{[1]}(\omega + i0^+)$ upon changing J/t. Spectra are aligned such that the ground state of the t–J^z model with a single hole on a Bethe lattice (with $z = 4$ everywhere) is at $\omega = 0$ for each J. The dashed red line is $\omega(J) = 2J$, while the dashed green line follows the maximum of the lowest rotational excitation.

For the Bethe lattice, the above behavior is understandable. Bethe lattice is a self-similar tree meaning that the ground state of the subsystem consisting of a subtree

of the Bethe lattice is qualitatively the same as the ground state of the whole system (if we disregard small discrepancies due to the different number of paths to delocalize from the central site). More precisely speaking, if we alter the coordination at the center such that $z_0 = 3$, then it is transparent that the expansion coefficients c_i of the ground state wave function in e.g. the position basis for the whole Bethe lattice and the hole locked in a subtree with k unremovable magnons are the same. They will just multiply states that differ exactly by this k magnons,

$$|\mathrm{GS}\rangle_0^{z_0=3} = c_0|0\rangle + c_1 \sum_{d_1=1}^{3} |1; d_1\rangle + c_2 \sum_{d_1,d_2=1}^{3} |2; d_1, d_2\rangle + \ldots, \tag{4.29}$$

$$\begin{aligned} |\mathrm{GS}\rangle_k^{z_0=3} = c_0|k; d_1, ..., d_k\rangle + c_1 \sum_{d_{k+1}=1}^{3} |k+1; d_1, ..., d_k, d_{k+1}\rangle + \\ + c_2 \sum_{d_{k+1},d_{k+2}=1}^{3} |k+2; d_1, ..., d_k, d_{k+1}, d_{k+2}\rangle + \ldots. \end{aligned} \tag{4.30}$$

But the state with the additional k magnons will be shifted in energy by $2kJ$. It turns out that even if this perfect balance is not conserved, e.g. $z_0 = 4$ as it should be, or when we consider the square lattice the discrepancy from perfect linear behavior is relatively small compared to model parameters (see Fig. 4.10). This is exactly why we see the linear-like scaling in J/t in the rotational spectra with non-zero angular momentum.

4.4.2. Mixing of vibrational and rotational modes on a square lattice

Now let us also understand why on the square lattice the linear rotational modes can be observed even when the hole does not possess any angular momentum—though the same is not true for the Bethe lattice. Let us again consider the t–J^z model on the Bethe lattice. In this case, the Hamiltonian conserves angular momentum,

$${}_r\langle n+1; m^{(1)}, ..., m^{(n)}, m^{(n+1)}|\hat{\mathcal{H}}_{t\text{–}J^z}|n; m^{(1)}, ..., m^{(n)}\rangle_r = \delta_{m^{(n+1)},0}. \tag{4.31}$$

At the same time, the eigenstates that are probed by the Green's function (standard or rotational) with $m^{(k)} = 0$ for every k live in a subspace of states that contribute to the following linear combination,

$$\hat{\mathcal{H}}_{t\text{–}J^z}^n|0\rangle, \tag{4.32}$$

for some value of $n = 0, 1, 2, 3, \ldots$. Altogether, states with non-zero angular momentum, i.e. $m^{(k)} \neq 0$ for at least one k, live in the orthogonal subspace to the one spanned from state $|0\rangle$ with the Hamiltonian $\hat{\mathcal{H}}_{t\text{–}J^z}$. The same holds for states that differ in the highest value of k for which $m^{(k)} \neq 0$. Those also belong to orthogonal subspaces. Thus there is no mixing between vibrational and rotational states (nor even between different kinds of rotational states) on the Bethe lattice.

To show that opposite happens on the square lattice, we introduce a simple toy model. This model is defined on the Bethe lattice but it effectively alters the symmetry of the problem such that it resembles the square lattice to some extent. To this end, we take the t–J^z model Hamiltonian $\hat{\mathcal{H}}_{t\text{–}J^z}$ on the Bethe lattice and introduce a

perturbation centered at the lattice where we introduce a hole to the system. This perturbation reads,

$$\hat{H}' = t \sum_{d_1=0}^{3} \sum_{l=1}^{2} (|3; d_1, l, l\rangle\langle 4; d_1, l, l, l| + |4; d_1, l, l, l\rangle\langle 3; d_1, l, l|). \tag{4.33}$$

The way the above-defined perturbation $\hat{H}'$ affects the motion of the hole on the Bethe lattice can be represented by the cartoons shown in Fig. 4.11. The perturbation affects only 8 paths of the hole by introducing a hopping term that cancels out with the equivalent terms present in the Hamiltonian. One of those 8 symmetrically equivalent paths is shown in Fig. 4.11.(a). Cancelation of the hopping terms effectively reduces the number of possible paths the hole can propagate to. Fig. 4.11.(b) [Fig. 4.11.(c)] shows the possible paths the hole takes without (with) the perturbation $\hat{H}'$ respectively.

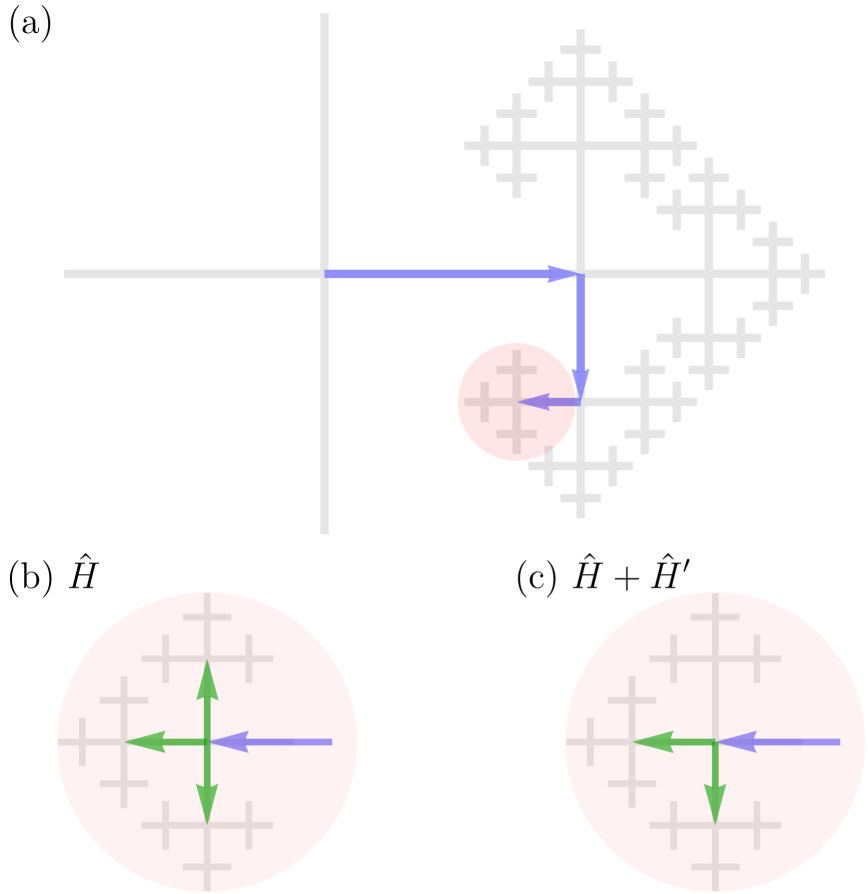

Figure 4.11: Cartoon picture of a hole moving along one of the branches of the Bethe lattice. Details of other branches are not included for better readability. Example path is shown in panel (a) where the hole moves in directions $d_1 = 0, d_2 = 2, d_3 = 2$ respectively. The resulting state has local C_3 symmetry at the position of the hole—as shown in panel (b) the hole can propagate forward in one of three equivalent directions. (c) This local C_3 symmetry is broken when $\hat{H}'$ is included—one of three paths is blocked for the motion of the hole.

Such perturbation breaks the C_3 symmetry for the set of possible bonds the hole can propagate along with the creation of a magnon. The motivation behind introducing

such seemingly artificial but in fact quite realistic perturbation comes from the fact that the C_3 symmetry is broken in a similar way on the square lattice. Notice that the path blocked by $\hat{H}'$ in Fig. 4.11.(c) corresponds to the smallest possible loop on the square lattice. Thus on one hand this path is blocked within the SAW approximation, where loops are by definition forbidden. On the other hand, the C_3 symmetry is broken also without SAW approximation, since the propagation in two directions would lead to the creation of the magnon but the third one would require the annihilation of a magnon. This of course leads to states with different total numbers of magnons and thus the C_3 symmetry is broken.

The perturbation $\hat{H}'$ can be easily incorporated into the calculations of the Green's function of a single hole on the Bethe lattice exactly. Since the magnon-magnon interactions do not matter on the Bethe lattice for coordination $z > 2$ let us exclude them. Then the corresponding exact expression for the Green's function of the single hole in the toy model $\hat{\mathcal{H}}_{t\text{-}J^z} + \hat{H}'$ on the Bethe lattice reads,

$$G_{\mathrm{toy}}(\omega)^{-1} = G_0(\omega)^{-1} - \Sigma_{\mathrm{toy}}(\omega), \tag{4.34}$$

$$\Sigma_{\mathrm{toy}}(\omega) = \cfrac{4t^2}{\omega - 4J - \frac{1}{3}\tilde{\Sigma}(\omega - 6J) - \cfrac{2t^2}{\omega - 6J - \frac{2}{3}\tilde{\Sigma}(\omega - 8J) - \cfrac{t^2}{\omega - 8J - \frac{2}{3}\tilde{\Sigma}(\omega - 10J)}}}, \tag{4.35}$$

$$\tilde{\Sigma}(\omega) = \frac{3t^2}{\omega - \tilde{\Sigma}(\omega - 2J)} = -t\sqrt{3}\frac{\mathcal{J}_{-\frac{\omega}{2J}}(\frac{t\sqrt{3}}{J})}{\mathcal{J}_{-\frac{\omega}{2J}-1}(\frac{t\sqrt{3}}{J})}, \tag{4.36}$$

where $\mathcal{J}_\alpha(z)$ is the Bessel function of the first kind and $G_0(\omega)^{-1} = \omega - 2J$.

In Fig. 4.12 we plot the evolution of the corresponging spectral function $A(\omega) = -\frac{1}{\pi}\mathrm{Im}G_{\mathrm{toy}}(\omega + i0^+)$ with coupling constant J. This way we can clearly see that breaking the C_3 for just the path corresponding to the smallest possible loop on the square lattice already leads to the hybridization of certain rotational ($\sim J/t$) and vibrational ($\sim (J/t)^{2/3}$) excitations. Comparing this result with the spectrum of the single hole on the square lattice (see Fig. 4.2.(a) or Fig. 4.3), we see a qualitatively good agreement. Of course, it is not exactly the same, since on the square lattice there are higher order processes (longer loops) possible which also break the C_3 symmetry. But at this point, we can already tell, that the hybridization on the square lattice originates from the C_3 symmetry breaking.

Let us now formally prove that breaking the C_3 symmetry leads to the hybridization of the rotational and vibrational modes. Let us consider a state $|3;0,0,0\rangle_r$ in rotational basis (i.e. on the Bethe lattice) which belongs to the subspace probed by the standard Green's function of the single hole. The unperturbed Hamiltonian clearly conserves the angular momentum,

$$\hat{\mathcal{H}}_{t\text{-}J^z}|3;0,0,0\rangle_r = E_3|3;0,0,0\rangle_r - t\sqrt{3}|2;0,0\rangle_r - t\sqrt{3}|4;0,0,0,0\rangle_r. \tag{4.37}$$

Now, let us observe what the $\hat{H}'$ does with the same state,

$$\begin{aligned}\hat{H}'|3;0,0,0\rangle_r &= t\sum_{d_1=0}^{3}\sum_{l=1}^{2}|4;d_1,l,l,l\rangle\langle 3;d_1,l,l|3;0,0,0\rangle_r \\ &= t\sum_{d_1=0}^{3}\sum_{l=1}^{2}|4;d_1,l,l,l\rangle\frac{1}{\sqrt{4\cdot 3^2}}.\end{aligned} \tag{4.38}$$

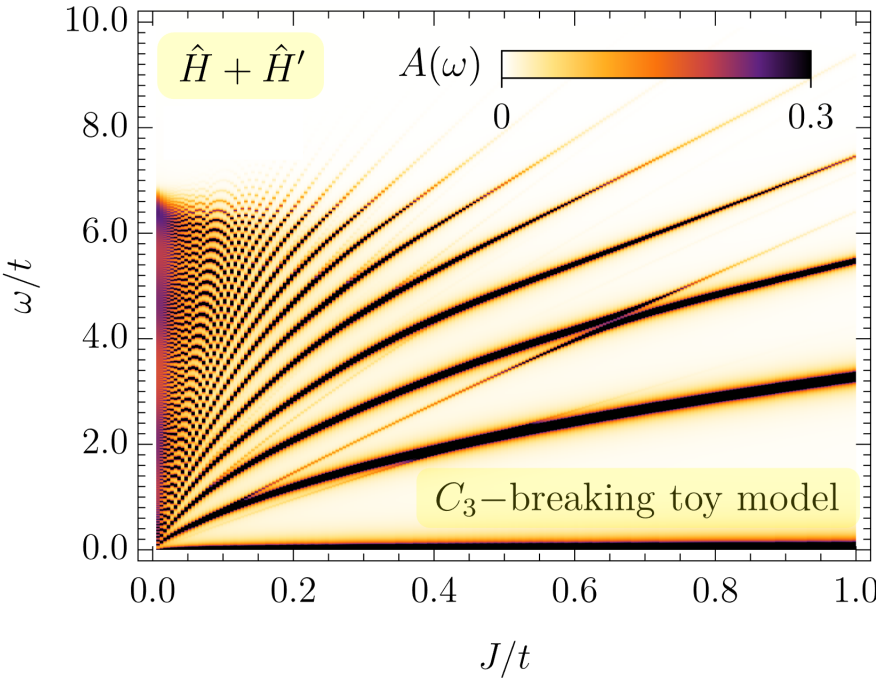

Figure 4.12: Single hole in a Bethe lattice Ising antiferromagnet: evolution of the spectral function $A(\omega)$ for the toy-model (modified t–J^z model, $\hat{\mathcal{H}}_{t\text{–}J^z}+\hat{H}'$, and without magnon-magnon interactions) upon changing J/t. The coupling to states with non-zero angular momentum is reflected in the mixing of zero- and non-zero-like degrees of freedom appearing as the energy level repulsion visible in the plot.

Expressing the above back in the rotational basis we obtain,

$$t\sum_{d_1=0}^{3}\sum_{l=1}^{2}|4;d_1,l,l,l\rangle\frac{1}{\sqrt{4\cdot 3^2}}= \\ =\frac{t}{9\sqrt{3}}\sum_{l=1}^{2}\prod_{k=2}^{4}\left(\sum_{m_3^{(k)}=0}^{2}\exp\left(-\frac{2\pi i}{3}lm_3^{(k)}\right)\right)|4;0,m_3^{(2)},m_3^{(3)},m_3^{(4)}\rangle. \tag{4.39}$$

From the above, we conclude that states described by $m_3^{(k)}\neq 0$ for $k>1$ appear in the result, and thus the perturbation $\hat{H}'$ will induce the coupling to subspaces with non-zero angular momenta.

In the end, let us point out that, although the loops enable the hybridization of the rotational and vibrational modes on the square lattice, the hybridization does not originate from loops but from more fundamental C_3 symmetry breaking. This has been shown quite explicitly by considering the C_3 symmetry breaking model on the Bethe lattice (which does not have loops) and the SAW approximation on the square lattice which (excludes loops)—in both cases we could observe the hybridization of rotational and vibrational modes.

The last remark to the investigated new class of rotational states goes beyond the studied model. One could notice, that the whole procedure described here is not unique to the t–J^z model. On the contrary, it is quite general, and thus it should be expected that the rotational and vibrational modes couple also in the t–J and Hubbard model

on the square or hexagonal lattices.

4.5. Conclusions

We study the evolution of the spectral function $A(\omega)$ of a single hole in the t–J^z model on a 2D square lattice upon changing J/t. Obtained results within SAW approximation as well as using numerical exact diagonalization provide evidence for the existence of excitations with energy scaling $\propto J/t$ apart from well-known vibrational excitations with energy scaling $\sim (J/t)^{2/3}$, see Fig. 4.1. This new class of states originates from the so-called rotational states (or modes) studied by Grusdt et *al.* [55] on the Bethe lattice. We show that the linear scaling of energy with J/t is a natural consequence of the rotational degrees of freedom available for the hole in either the Bethe or the 2D square lattice, see Sec. 4.4.1. On the Bethe lattice, the symmetry of rotational states of the hole effectively renders the hole confined in a subbranch of the lattice, see Fig. 4.9. Effectively magnons that do not belong to any of the branches available for the hole cannot be annihilated driving the linear energy shift for rotational modes. Approximately, similar reasoning is also valid for the square lattice explaining the origin of the linear behavior.

Within SAW approximation we derive the general recursive formula, Eq. (4.17), for the Green's function $G_{M_n}(\omega)$, Eq. (4.1), of a single hole with non-zero angular momentum in the t–J^z model on the 2D square and the Bethe lattices. By comparing the spectral function with and without rotational parameters we conclude that the vibrational and rotational modes of the hole hybridize on the square lattice but not on the Bethe lattice. To explain this phenomenon, we introduce a toy model defined on the Bethe lattice, see Sec. 4.4.2. The toy model allows us to break the C_3 symmetry [see Eq. (4.38)] for the hole propagation on the Bethe lattice, see Fig. 4.11. We analytically calculate the expression for the spectral function of a single hole in the toy model [see Eq. (4.34)] to show that breaking of the C_3 symmetry induces the hybridization of rotational and vibrational modes of the hole, see Fig. 4.12. Importantly, such C_3 symmetry breaking naturally appears on the 2D square lattice but not on the Bethe lattice. This explains why the rotational modes of the hole can be observed in the (standard) spectral function $A(\omega)$ of the single hole on the 2D square lattice.

Together with results from Ch. 3 we can conclude that the spectral function $A(\omega)$ of a single hole in the t–J^z model consists of 3 kinds of states: (a) the well-known vibrational modes with energy scaling $\sim (J/t)^{2/3}$; (b) rotational modes with energy scaling $\sim J/t$; and (c) densely packed states forming an incoherent spectrum as a result of magnon-magnon interactions on the 2D square lattice.

Chapter 5

1D t–J model

Based on Piotr Wrzosek, Adam Kłosiński, Yao Wang, Mona Berciu, Cliò E. Agrapidis, Krzysztof Wohlfeld, arXiv:2203.01846.

One of the fundamental results in condensed matter physics is the affinity of the hole injected into the 2D antiferromagnet to dress in magnons and to form a stable quasiparticle—a spin polaron [52–59, 84]. On the other hand, in the 1D antiferromagent the hole is not expected to form a spin polaron, but to split into two independent parts—a holon and a spinon [28, 35, 44–49]. The latter process is called spin-charge separation for the holon carries a charge $+e$ and the spinon carries a spin $s = \frac{1}{2}$. In this chapter, we will show that although theoretically possible, the spin-charge separation in real 1D materials is most likely unstable to the collapse into a spin polaron. To this end, we will start with the t–J model and investigate the influence of the magnon-magnon interactions on the stability of a quasiparticle ground state in 1D t–J model with a single hole. Moreover, using the same language for the 1D t–J model as for its 2D counterpart we can understand the differences between the 1D and 2D cases.

The significant difference between the t–J model and its Ising limit (t–J^z model) studied in previous chapters is the lack of the spin exchange processes in the latter one (see Fig. 1.2 and 1.4). When the spin exchange is present the number of magnons fluctuates on its own. Thus, the creation or annihilation of a magnon due to the motion of the hole intuitively appears less important in the t–J model than in its Ising limit. The ground state in the half-filling is no longer an Ising state. Instead, it will contain a certain number of magnons even before the hole is introduced to the system. The motion of the introduced hole is also affected. The hole in the t–J^z model in 1D is at least 'weakly' confined (see Sec. 2.3.2). But exchange processes in t–J model may repair excitations created due to the motion of the hole and thus the hole does not necessarily have to be confined.

The Hamiltonian $\hat{\mathcal{H}}_{t\text{–}J}(\lambda)$ of the t–J model in the magnon-holon basis with scaling parameter λ for the strength of the magnon-magnon interactions is given in Eq. (1.22). We will be interested in the values of $\lambda \in [0, 1]$ where $\lambda = 1$ yields the exact t–J model. The approach we take is based on the implementation of the Krylov subspace methods (e.g. Arnoldi/Lanczos iteration) and the exact diagonalization procedure of the model (1.22) in the polaronic language, see Sec. 5.4 (we decide to move the details of numerical calculations to the end as they are not important to understand the results of this chapter).

5.1. Spectral function of the single hole

We choose the exact method since we want to tackle a subtle problem of quasiparticle decay. The only concern here may come from the finite-size effects, but those turn out to be small enough to find conclusive answers for the existence of the quasiparticle ground state. Let us lead with the spectral properties of the hole introduced to the undoped t–J chain. The spectral function $A(k,\omega)$ defined in Eq. (1.2) is calculated in the polaronic language from the below Green's function,

$$G(k,\omega) = \langle\psi_{\mathrm{GS}}|\hat{\tilde{c}}_k^\dagger \frac{1}{\omega - \hat{\mathcal{H}}_{t\text{–}J}(\lambda) + E_{\mathrm{GS}}} \hat{\tilde{c}}_k|\psi_{\mathrm{GS}}\rangle, \tag{5.1}$$

where $\hat{\tilde{c}}_k = (\hat{\tilde{c}}_{k\uparrow} + \hat{\tilde{c}}_{k\downarrow})/\sqrt{2}$. State $|\psi_{GS}\rangle$ is the ground state of the undoped t–J model (Heisenberg model). Note that the above-defined Green's function is equal to the one defined in Eq. (1.3) when $\lambda = 1$. Replacing $\hat{\tilde{c}}_k \to \hat{\tilde{c}}_{k\sigma}$ does not affect the result thanks to two facts: (i) the Hamiltonian conserves the magnetization, (ii) the electron is not removed locally. Thus the result does not depend on the sign of the removed spin. When reexpressed in polaronic language, the above-defined Green's function appears as,

$$G(k,\omega) = \frac{1}{2N}\sum_{i,j} \mathrm{e}^{-ik(r_i - r_j)} \langle\tilde{\psi}_{\mathrm{GS}}|(1+\hat{a}_j^\dagger)\hat{P}_j\hat{h}_j \frac{1}{\omega - \hat{\mathcal{H}} + E_{\mathrm{GS}}} \hat{h}_i^\dagger \hat{P}_i(1+\hat{a}_i)|\tilde{\psi}_{\mathrm{GS}}\rangle, \tag{5.2}$$

where $|\tilde{\psi}_{\mathrm{GS}}\rangle = \mathcal{M}\mathcal{R}_A|\psi_{\mathrm{GS}}\rangle$ is the ground state in magnon-holon basis. For more details, have a look at Sec. 5.4.

The results of the calculations of the spectral function $A(k,\omega)$ with and without magnon-magnon interactions included are shown in Fig. 5.1. The exact spectral function of the single hole in the t–J model is shown in panel (a) ($\lambda = 1$) of Fig. 5.1. It fully matches the previous exact diagonalization studies on this front [45, 85] and fits the well-known Ansatz for the holon dispersion and the edge of the spinon-holon continuum [86, 87] plotted on top of the density data. The two panels of Fig. 5.1, showing the spectra with ($\lambda = 1$) and without (λ) magnon-magnon interactions present seemingly similar but qualitatively completely different scenarios. Let us address both the similarities and the differences between the two presented spectra in the next two sections.

5.1.1. Similarities between $\lambda = 1$ and $\lambda = 0$

Looking at the momentum-resolved spectral functions $A(k,\omega)$ calculated with and without the magnon-magnon interactions, it is difficult to miss the resemblance in the overall shape between the two [cf. Fig. 5.1 panel (a) $\lambda = 1$ and (b) $\lambda = 0$]. Quantitatively we can measure how similar the two functions are by calculating n-th moments of $A(k,\omega)$ with respect to energy ω,

$$I_n(k) = \int_{-\infty}^{\infty} A(k,\omega)\omega^n \, d\omega. \tag{5.3}$$

From the calculations of the first and the second moments (see Fig. 5.2) we see that the average energy of the spectrum, as well as the envelope, are indeed quite congruent. This does not seem like an important result until we notice that the resolution of ARPES experiments on cuprates is typically quite low. It is therefore challenging to

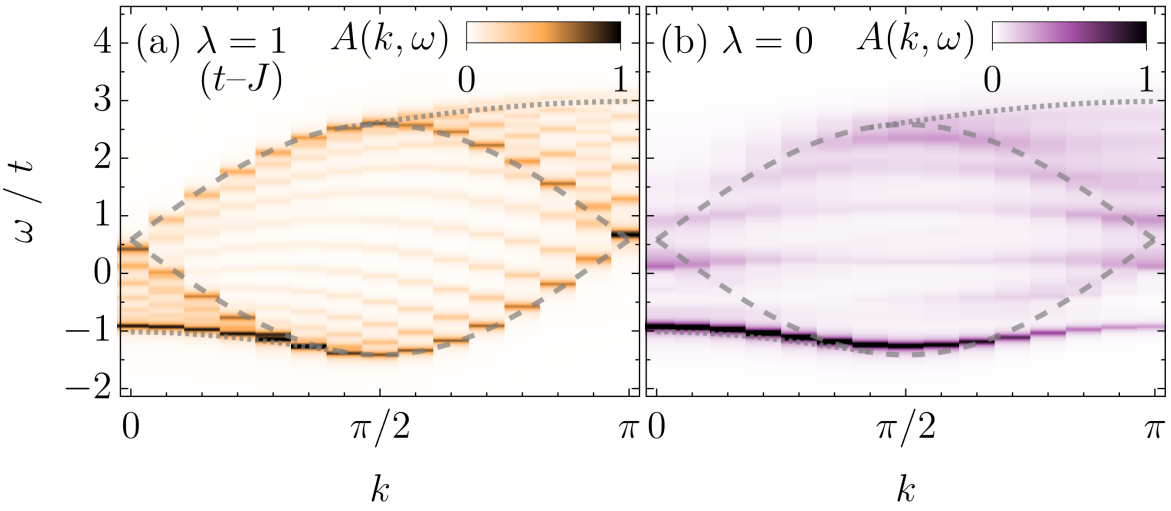

Figure 5.1: Spectral function $A(k,\omega)$ of a single hole in the t–J model on the periodic chain with 28 sites (a) with and (b) without magnon-magnon interactions included. The gray dashed line corresponds to the dispersion of a free holon, and the gray dotted line stands for the edge of the spinon-holon continuum accordingly to the spin-charge separation Ansatz [86, 87]. Data were obtained for the standard value of the coupling constant $J = 0.4t$ using the Lanczos method. Figure taken from Ref. [88].

distinguish the two presented cases in experimental data. But what if behind these two seemingly close spectra hides a completely different physical picture of the problem? We will answer this question below.

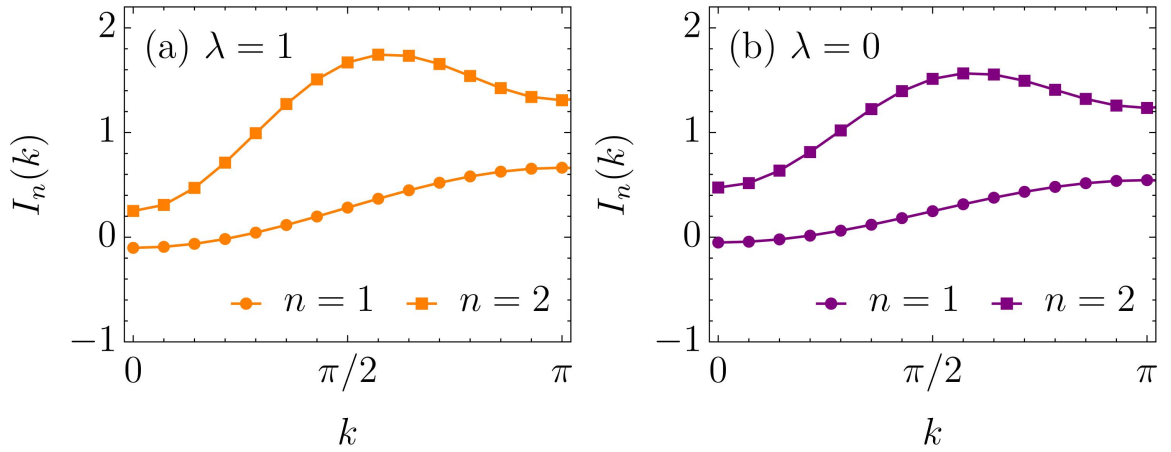

Figure 5.2: The first and second moments $I_n(k) = \int_{-\infty}^{\infty} A(k,\omega)\omega^n \mathrm{d}\omega$ of the spectral function of a single hole in the t–J model (1.26) (a) with and (b) without magnon-magnon interactions included. Data were obtained for a periodic chain with 28 sites and $J = 0.4t$ using the Lanczos method. Figure taken from Ref. [88].

5.1.2. Differences: existence of a quasiparticle for $\lambda < 1$

The observant eye could already notice an important difference between the case with and without the magnon-magnon interactions in Fig. 5.1. There is visibly an additional

branch at lowest energies at momenta k between $\frac{\pi}{2}$ and π for $\lambda = 0$ case, while this branch is absent for $\lambda = 1$. In fact, for $\frac{\pi}{2} < k \leq \pi$ states with energies smaller than the energy of the free holon give zero contribution to the spectral function at $\lambda = 1$. Nevertheless, such states still exist as eigenstates of the problem—they just cannot be observed in the spectral function of a single hole.

The second difference, although even more important, cannot be easily seen in Fig. 5.1. It is well-known that for the t–J model (i.e. $\lambda = 1$) the spectrum of a single hole in one dimension consists of the continuum of states for all momenta. But when magnon-magnon interactions are rescaled from the exact value of $\lambda = 1$ the picture changes drastically—a single peak splits from the continuum at the ground state energy at every momentum k. Using exact diagonalization in magnon-holon basis, for each *rotating* momentum (for details see Sec. 5.4) subspace p we calculate the lowest lying energies of the model with and without the magnon-magnon interactions. Note that the spectral function $A(k, \omega)$ contains only partial information about the eigenvalues, but it is true that the only contribution for the hole with momentum k comes from $p = k$. Several lowest states for each subspace p calculated for a chain with 28 sites are shown in Fig. 5.3. For the t–J model ($\lambda = 1$) the ground state indeed, as expected, is not visibly split from the rest of the states [see Fig. 5.3.(a)]. At the same time, when the magnon-magnon interactions are switched off ($\lambda = 0$), the ground state becomes a dispersive quasiparticle split from the continuum of the excited states at higher energies.

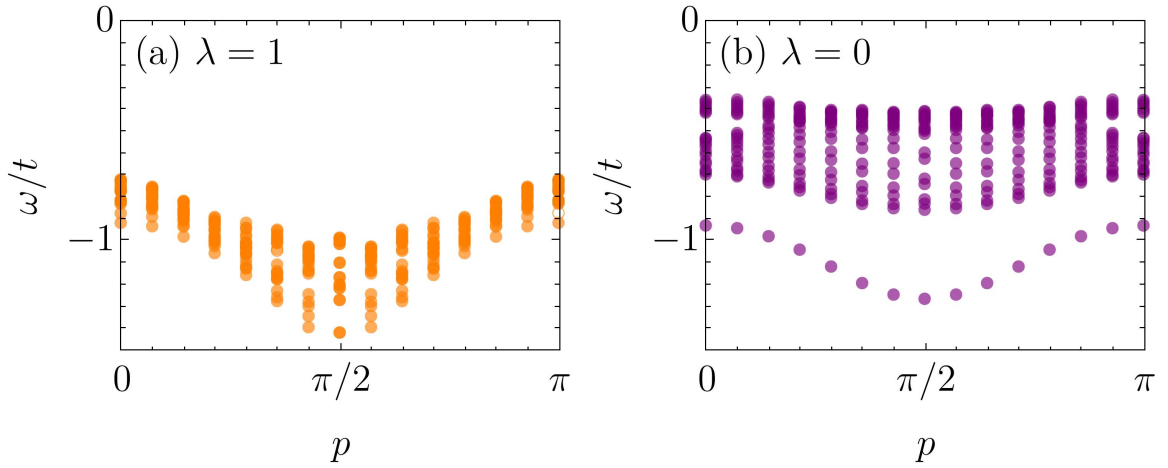

Figure 5.3: Tower of states for the t–J model (1.26) with one hole added to the half-filled system (a) with magnon-magnon interactions and (b) without magnon-magnon interactions included. Only the several lowest energies are shown for each subspace corresponding to *rotating* momentum p. Transparency of the points does not have any meaning, it is used to make overlapping data points more visible. Note that only some of the states shown here give a contribution to the spectral function $A(k = p, \omega)$. Calculations were performed using exact diagonalization on a chain with 28 sites and with $J = 0.4t$.

The existence of the separated ground state for a finite-size lattice does not yet guarantee the survival of the quasiparticle when we go to the thermodynamic limit. To address this concern we perform a finite size scaling of the energy gap ΔE between the ground state and the first excited state as well as the scaling of the quasiparticle

residue z at the ground state energy. We present the results in Fig. 5.4. To infer the proper scaling of the gap we notice that in the thermodynamic limit, the ground state energy should not be affected by a presence of a single hole. Based on the previous studies for the Heisenberg model [89] we conclude the proper scaling for the case of $\lambda = 1$ should be linear in $1/L$ up to a small logarithmic correction,

$$\Delta E(L) = \frac{a}{L} + \frac{b}{L\log(L)}, \tag{5.4}$$

where a and b are fitting parameters. For $\lambda \neq 1$ we decide to use the same scaling behavior. The result is shown in Fig. 5.4.(a-c) for *rotating* momenta $p = k \in \{0, \frac{\pi}{2}, \pi\}$. While for the t–J model ($\lambda = 1$) the gap ΔE goes close to zero when the system size L grows, for $\lambda \neq 1$ the data suggests the ground state should stay separated from higher energy states in the thermodynamic limit. This claim holds for all momenta (not shown).

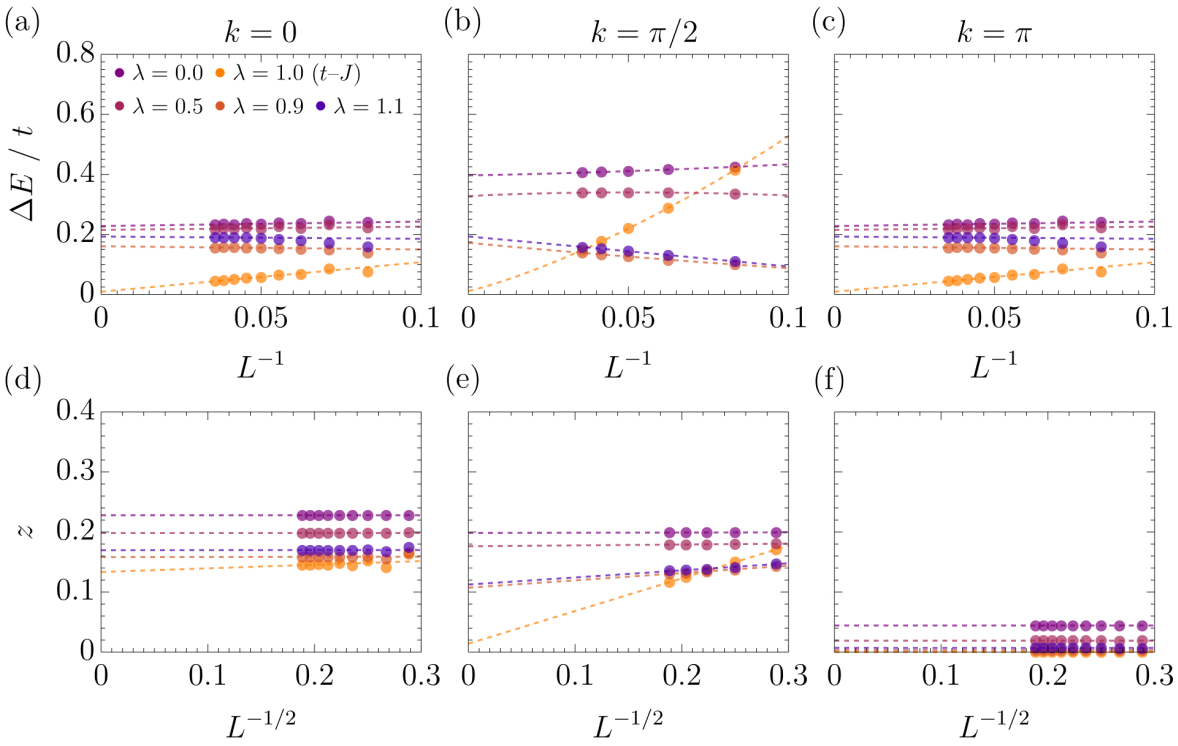

Figure 5.4: Finite size scaling of the energy difference ΔE between the ground state and the first excited state (top panels) and the hole quasiparticle residue z at the ground state energy (bottom panels). Data presented for *rotating* momenta $p = k \in \{0, \frac{\pi}{2}, \pi\}$. The scaling behavior has been obtained by fitting to the 5 highest L points in each case. Calculations were performed for $J = 0.4t$ on a periodic chain with 28 sites. Figure besed on Ref. [88].

To confirm the existence of the quasiparticle at the ground state energy for $\lambda \neq 1$ we need to make sure that the quasiparticle weight does not disappear in the thermodynamic limit. To this end, we follow the scaling obtained from the exact solution of the 1D t–J model with $J = 2t$ [90]. The scaling of the quasiparticle weight z for large system sizes is thus assumed to be linear in the inverse square root of the system size,

$$z(L) = \frac{a}{\sqrt{L}}, \tag{5.5}$$

where a is the fitting parameter. For all the cases our results yield that the quasiparticle weight is highest for small momenta $k \simeq 0$ and drops consecutively when k grows to the value of π. Nevertheless, as long as $\lambda \neq 1$ the results support a finite z when $L \to \infty$ for all k. Connecting this with the result for ΔE, we conclude that most likely the quasiparticle exists for all $\lambda \neq 1$. It is also the first sign that the case of $\lambda = 1$ is unique. This supports the claim that the two seemingly close spectra in Fig. 5.1 are indeed hiding a completely different physical picture.

We understand that this kind of numerical analysis might still not be convincing when it comes to determining whether there is a particular region of the values of λ around the value of 1 where there is no quasiparticle or it is just one point $\lambda = 1$ that is special. We claim that indeed $\lambda = 1$ is unique, and to further support this point we turn our attention to the ground state wave function of the 1D t–J model in the single hole limit.

5.2. Ground state properties

The essential feature of the spin-charge separation is the independence of the motion of the spin and the charge excitation in the system. On the other hand, spin polaron can be understood as a collective motion of a hole and a cloud of magnons around it. By studying the ground state wave function of the 1D t–J model in the single-hole limit, we hope to observe how those facts instantiate themselves in terms of spin and magnon order around the hole for different values λ of the magnon-magnon interactions. To this end, we study a 3-point correlation function in spin basis and coefficients of the ground state wave function expressed using the polaronic basis. This allows us to determine whether the ground state of the system is a spin polaron quasiparticle or if it should be understood in terms of the spin-charge separation.

5.2.1. Spin-hole-spin correlation function $C(s, d)$

We start with the spin-hole-spin correlation function $C(s, d)$ introduced in the previous studies to investigate the magnetic properties of the doped Fermi-Hubbard model cold atoms simulations [91]. This correlator can be in short written as,

$$C(s, d) = (-1)^d 4L \langle \hat{S}^z_0 (1 - \hat{\tilde{n}}_{s+d/2}) \hat{S}^z_d \rangle, \tag{5.6}$$

where s is the distance from the center of mass of two spins and d is the distance between the two spins. L denotes the length of the chain used in the calculations. The way this correlator works is simple. Without the hole in the system, the value of the above correlator would be positive everywhere, reflecting the antiferromagnetic order of the ground state [notice $(-1)^d$ "swallows" the alternating spin signs]. This value would be equal to 1 in the Ising limit, but spin fluctuations in the Heisenberg limit suppress it. When the hole is present in the system it can move and thus shift spins along its path. If only one of the two measured spins is shifted by the hole, then the correlation becomes ferromagnetic, i.e. the correlator becomes negative.

First, let us understand the difference between the $\lambda = 1$ and $\lambda = 0$ cases. The results are presented in Fig. 5.5. For $\lambda = 1$ [Fig. 5.5.(a)] we can see the correlation becomes negative when the hole is measured between the two spins up to the distance $d = L/2$. Such a result means that the hole can freely move in the system shifting as many spins as it wants and therefore it is a fingerprint of the spin-charge separation.

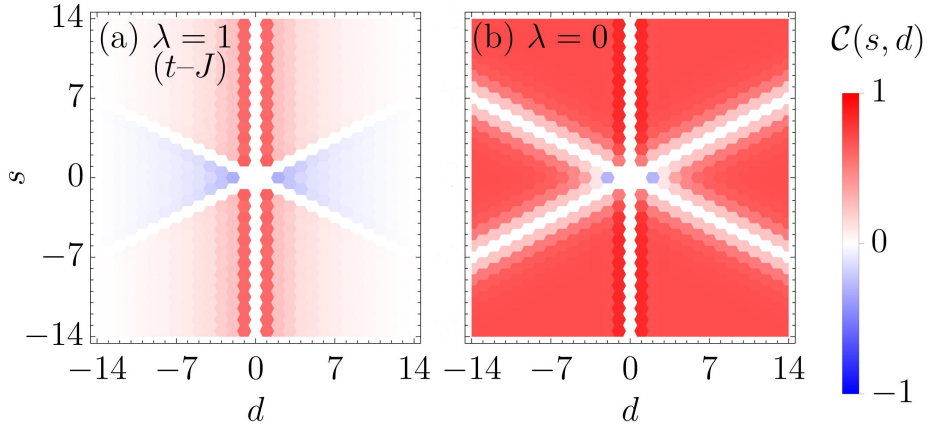

Figure 5.5: Three-point spin-hole-spin correlation function $\mathcal{C}(s,d)$ (a) with and (b) without the magnon-magnon interactions included. Data were obtained for a periodic chain with 28 sites and $J = 0.4t$ using the exact diagonalization. Figure taken from Ref. [88].

On the other hand, the correlator $C(s,d)$ obtained for $\lambda = 0$ [Fig. 5.5.(b)] tells quite a different story. Here only a very small number of spins shifted out of the antiferromagnetic order is likely to be found around the hole. This is exactly what a spin polaron should look like—the hole is dressed in a cloud of magnons and it can only move together with the cloud.

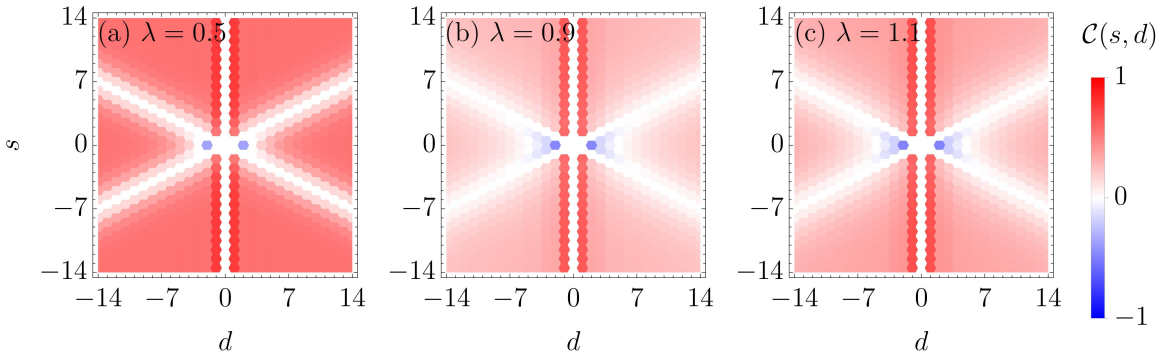

Figure 5.6: Three-point spin-hole-spin correlation function $\mathcal{C}(s,d)$ for three different strengths of the magnon interactions $\lambda \in \{0.5, 0.9, 1.1\}$. Data were obtained for a periodic chain with 28 sites and $J = 0.4t$ using the exact diagonalization. Figure taken from Ref. [88].

When we look at the same quantity calculated for other values of λ (see Fig. 5.6), we can notice, that even when the value of the magnon-magnon interactions is relatively close to the value of $\lambda = 1$, the hole is surrounded by only a small region of spins affected by the motion of the hole. For the presented values of $\lambda \neq 1$, the size of the area where the correlator is negative is intensive, so it does not change when the system size grows—the hole acts only locally. On the other hand, when $\lambda = 1$, it is extensive. We believe that this kind of transition can happen only when $\lambda \to 1$, since only then the energy cost of consecutive magnons arranged in a chain is finite [see Fig. 2.8.(a1-a2) and discussion in Sec. 2.3.2]. For any $\lambda \neq 1$ the energy cost of an infinite chain of magnons becomes infinitely large and thus the hole would not be able to excite the

infinitely many magnons for finite model parameters. In the end, for all $\lambda \neq 1$ the ground state of the system is a spin polaron.

5.2.2. Probability of observing n magnons attached to a hole c_n

In what follows we want to even further support the claim that the case of $\lambda = 1$ is unique and that for $\lambda \neq 1$ the ground state can be understood as a spin polaron. To this end, we study coefficients c_n describing the probability of finding a chain of exactly n consecutive magnons attached to the hole on one of its sides in the ground state of the 1D t–J model in the single-hole limit. We achieve it by diagonalizing the model in polaronic basis to find its ground state and then by extracting the coefficients of basis states fulfilling the condition that the hole is attached to the chain of exactly n consecutive magnons. We plot the results on the logarithmic scale in Fig. 5.7.

When $\lambda = 1$, the result is symmetric with respect to $(L-1)/2$, where $L-1$ is the maximum number of magnons possible in the system. Any number of magnons in a chain attached to the hole is probable to be found with almost the same coefficient c_n. We can see that the hole motion is not restricted by the created magnons. This is a fingerprint of the spin-charge separation in terms of polaronic basis states. When $\lambda \neq 1$ the coefficients c_n decay with n. The hole is most likely to excite only small chains of magnons. We infer that the motion of the hole is in this case restricted by created excitations—the hole dresses in a cloud of magnons around it and forms a spin polaron quasiparticle.

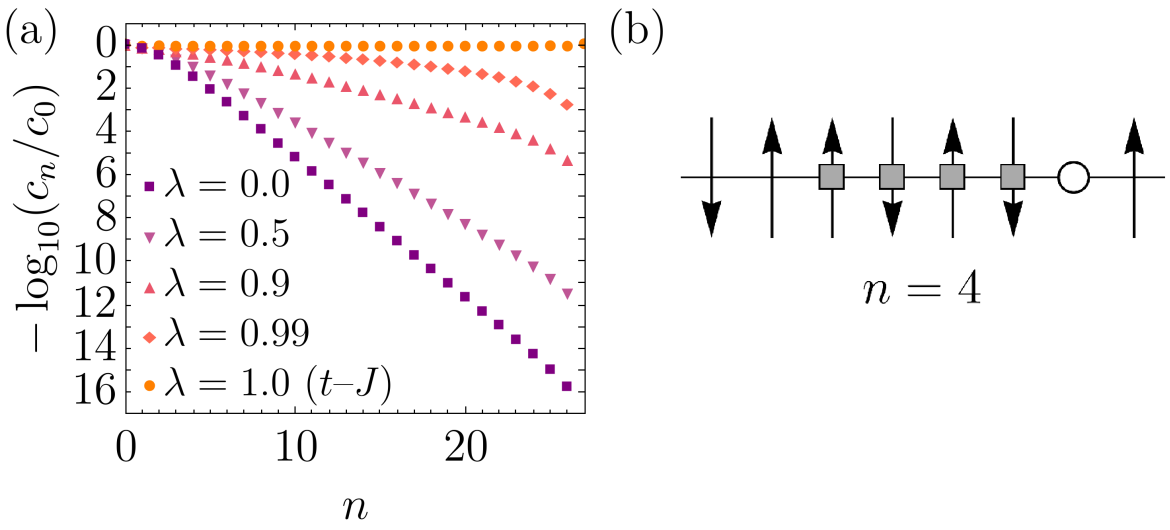

Figure 5.7: (a) size of the cloud of magnetic excitations due to a hole motion measured by the coefficients c_n of the contribution of states with exactly n magnons in a chain to the ground state of the 1D t–J model in the single-hole limit. (b) example of a state contributing to c_4. Calculations performed using exact diagonalization for $J = 0.4t$ on a periodic chain with 28 sites for various values of the magnon interaction λ. Figure taken from Ref. [88].

Interestingly, there is a drastic change in the form of the result obtained with exact diagonalization. While for $\lambda = 1$ we have $c_0 = c_{L-1}$, any value of $\lambda \neq 1$ immediately yields $c_{L-1} = 0$ up to the numerical precision. Such a result suggests that taking any $\lambda \neq 1$ breaks a certain symmetry of the system that is necessary for the spin-charge separation to take place. In the end, our results fully support the claim that for any

$\lambda \neq 1$ the ground state of the t–J model in the single hole limit can be understood as a spin polaron quasiparticle. And only when the exact value of $\lambda = 1$ is retained, the spin-charge separation takes precedence.

5.3. Application to the *quasi*-1D cuprates

Although there are algebraically decaying antiferromagnetic correlations, there is no long-range antiferromagnetic order in the 1D Heisenberg model. Moreover, hole doping also works against antiferromagnetism in cuprate compounds [see Fig. 1.1.(c)]. Yet neutron elastic diffraction studies combined with muon spin relaxation measurements performed on *quasi*-1D cuprates (Sr_2CuO_3 and Ca_2CuO_3) reveal the existence of magnetic order in this materials [63, 64]. The studies also point out that the magnetic order is a result of small but finite interchain magnetic interactions [63]. In what follows, we want to understand how the small interchain coupling affects the physics of the hole in *quasi*-1D cuprates. And we attempt to do it by mapping the above problem onto the t–J model with rescaled magnon-magnon interactions.

To this end, we will assume only the magnetic part of the interchain interactions is important since it affects many magnons, while the interchain hole hopping can be neglected [92]. Thus we consider the hole can move only along a single chain. The very small longer-range hopping can also be neglected [93]. Based on mean-field considerations, the interchain coupling between spin degrees of freedom is effectively described with the staggered magnetic field term [94],

$$\hat{H}_{J_\perp} = \frac{J_\perp}{2} \sum_{\langle i,j \rangle} \left[(-1)^i \hat{S}_i^z + (-1)^j \hat{S}_j^z \right], \tag{5.7}$$

where $J_\perp$ is the interchain spin coupling (see Fig 5.8). This way a two-dimensional problem where the middle chain feels the antiferromagnetic correlations of the neighboring chains is mapped onto the 1D problem of an antiferromagnetic chain in an external staggered magnetic field. Note that the sign of $J_\perp$ does not matter, both ferro- and antiferromagnetic interchain couplings result in an effective staggered field. The value of $J_\perp$, though typically order(s) of magnitude smaller than J, depends on the material, for example $J_\perp \approx -0.06J$ in $KCuF_3$ [94].

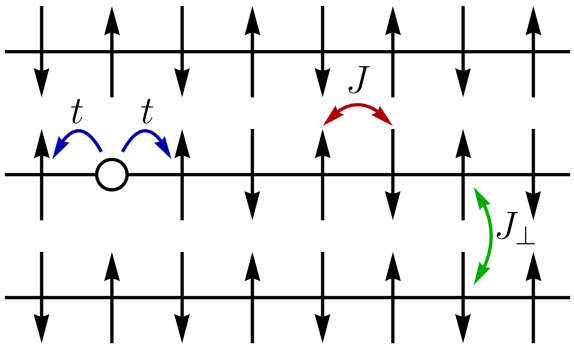

Figure 5.8: Cartoon of a set of coupled chains. The physics of a single chain is described with an antiferromagnetic t–J model. Due to interchain coupling $J_\perp$, the middle chain feels the staggered magnetic field from the neighboring chains. Figure taken from Ref. [88].

5.3.1. The t–J model in the staggered field

Let us now study the 1D t–J model in an external staggered magnetic field $\hat{H}_{J_\perp}$ by mapping it onto a polaronic basis. Performing the sublattice rotations followed by Holstein-Primakoff and slave-fermion transformations, see Sec 1.5.1, we obtain (up to a shift by a constant),

$$\hat{\mathcal{H}}_{J_\perp} = \frac{J_\perp}{2}\sum_{\langle i,j\rangle}\left(\hat{a}_i^\dagger\hat{a}_i\hat{h}_i\hat{h}_i^\dagger + \hat{a}_j^\dagger\hat{a}_j\hat{h}_j\hat{h}_j^\dagger\right) \approx \frac{J_\perp}{2}\sum_{\langle i,j\rangle}\hat{h}_i\hat{h}_i^\dagger\left(\hat{a}_i^\dagger\hat{a}_i + \hat{a}_j^\dagger\hat{a}_j\right)\hat{h}_j\hat{h}_j^\dagger. \tag{5.8}$$

Terms omitted on the right-hand side are $\propto J_\perp\left(\hat{a}_i^\dagger\hat{a}_i\hat{h}_j\hat{h}_j^\dagger + \hat{a}_j^\dagger\hat{a}_j\hat{h}_i\hat{h}_i^\dagger\right)$ and modify the magnetic field only around the hole. In the single-hole limit, we can therefore write,

$$\begin{aligned}\hat{\mathcal{H}}_{t\text{–}J} + \hat{\mathcal{H}}_{J_\perp} \approx\ & t\sum_{\langle i,j\rangle}\hat{P}_i\left(\hat{h}_i^\dagger\hat{h}_j\hat{a}_i + \hat{h}_i^\dagger\hat{h}_j\hat{a}_j^\dagger\right)\hat{P}_j + \text{H.c.},\\ &+\frac{J}{2}\sum_{\langle i,j\rangle}\hat{h}_i\hat{h}_i^\dagger\left[\hat{P}_i\hat{P}_j\hat{a}_i\hat{a}_j + \hat{a}_i^\dagger\hat{a}_j^\dagger\hat{P}_i\hat{P}_j\right]\hat{h}_j\hat{h}_j^\dagger\\ &+(1+\Delta)\frac{J}{2}\sum_{\langle i,j\rangle}\hat{h}_i\hat{h}_i^\dagger\left(\hat{a}_i^\dagger\hat{a}_i + \hat{a}_j^\dagger\hat{a}_j - 2\lambda\hat{a}_i^\dagger\hat{a}_i\hat{a}_j^\dagger\hat{a}_j\right)\hat{h}_j\hat{h}_j^\dagger.,\end{aligned} \tag{5.9}$$

where $\hat{\mathcal{H}}_{t\text{–}J}$ follows from Eq. (1.16) and the XXZ anisotropy Δ and the magnon-magnon interaction λ parameter are given by

$$\Delta = \frac{J_\perp}{J}, \quad \lambda = \frac{1}{1+\Delta}. \tag{5.10}$$

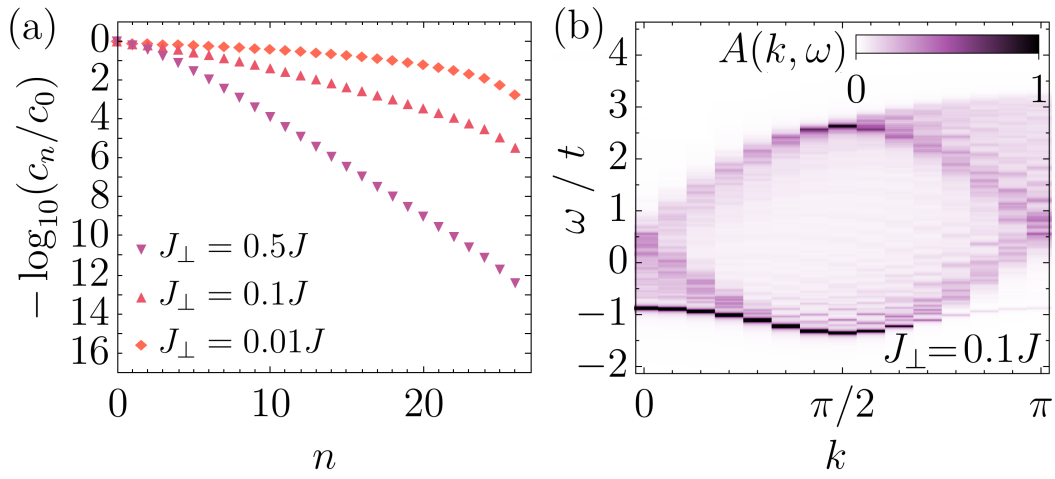

Figure 5.9: Ground state and spectral properties of the single hole in the anisotropic t–J model in an external magnetic field as given by Eq. (5.9). The coefficients c_n reflecting the probability of finding a chain of n consecutive magnons attached to a hole in the single-hole ground state are shown in the left panel (a). The spectral function of a single hole injected into the otherwise half-filled ground state is shown in the right panel (b). Calculations performed using exact diagonalization and the Lanczos method for a 28-site long periodic chain with $J = 0.4t$. Figure taken from Ref. [88].

For the antiferromagnetic interchain couplings $J_\perp > 0$, the magnon-magnon interactions are reduced, supporting rather the existence of spin polaron quasiparticle ground

state than a spin-charge separation picture. At the same time, small $\Delta > 0$ pushes the model slightly into the direction of the Ising limit, where we also could observe the separated peak at the ground state energy (see Fig. 3.7). To further confirm this, we perform exact diagonalization studies of the effective model defined in Eq. (5.9). The results for coefficients c_n of the ground state are shown in Fig. 5.9.(a), and they decay with n for $J_\perp \neq 0$. Note that the realistic values of the parameter $J_\perp/J \in [0.01, 0.1]$.

Interestingly, the spectral function of a single hole shown in Fig. 5.9.(b) is almost indistinguishable from the pure t–J model spectral function of a single hole (cf. Fig. 5.1). In Fig. 5.9.(b) there is a very faint weight at the ground state energy for $k > \frac{\pi}{2}$ and a small gap ΔE but in the experimental setup those features could not be resolved due to poor resolution of the ARPES measurements [20]. Therefore our result, which is based on the realistic t–J model for *quasi*-1D cuprates (see above), agrees with the current experiments yielding the important consequence for the interpretation of the ground state of lightly doped *quasi*-1D cuprates [27] in terms of a spin polaron.

5.4. Methods: Green's function in magnon-holon basis using exact diagonalization techniques

In the end, we provide a detailed description of the calculations of the Green's function used to obtain spectral function results presented in Sec. 5.1. The main goal of this Section is to present a proper way of calculating Green's function in polaronic language using exact diagonalization and to make it possibly time efficient. Note that an alternative approach is to calculate Green's function using the Lanczos method with an initial vector for the tridiagonalization procedure calculated according to Eqs. (5.28) and (5.32). Most importantly we want to avoid the typical caveat existing in the standard SCBA approaches where the resulting spectral function incorrectly turns out to be symmetric also around momentum $k = \frac{\pi}{2}$ [54]. This can happen when the rotation of a sublattice is not applied to the creation and annihilation operators present in the definition of Green's function, while the rest of the system has been subject to such rotation. As a result, the electron with the wrong spin is annihilated on the rotated sublattice. This artificially introduces a 2-site unit cell for the problem leading to the shrinkage of the Brillouin zone by half.

5.4.1. Rotating momentum states and the Green's function

Keeping the above discussion in mind, let us proceed to the solution. By definition, the action of the rotated Hamiltonian on the rotated state is equivalent to the action of the former Hamiltonian on the former state (see Sec. 1.5.1),

$$\hat{H}_{\mathrm{rot}}|\psi_{\mathrm{rot}}\rangle = \mathcal{R}_A \hat{H} \mathcal{R}_A^\dagger \mathcal{R}_A |\psi\rangle = \mathcal{R}_A \hat{H}|\psi\rangle. \tag{5.11}$$

The same holds for $\hat{\mathcal{H}}_{t\text{–}J}$ [Eq. (1.22)] acting on states expressed in the polaronic language.

Let us now observe the action of translation operators that simply shift the whole system by one site. We denote them by $\hat{T}_s$ for spin basis and $\hat{T}_m$ for polaronic basis. For example, we have,

$$\begin{aligned} \hat{T}_m|\varnothing\rangle = |\varnothing\rangle \equiv |\circ\circ\circ\circ\circ\ldots\rangle, \\ \mathcal{M}\mathcal{R}_A \hat{T}_s \mathcal{R}_A^\dagger \mathcal{M}^\dagger |\varnothing\rangle = |\Omega\rangle \equiv |\bullet\bullet\bullet\bullet\bullet\ldots\rangle, \end{aligned} \tag{5.12}$$

which gives,

$$\hat{T}_m \neq \mathcal{M}\mathcal{R}_A\hat{T}_s\mathcal{R}_A^\dagger\mathcal{M}^\dagger, \tag{5.13}$$

thus $\hat{T}_m$ is not just a transformation of $\hat{T}_s$ to polaronic language (rotation of a sublattice followed by the Holstein-Primakoff and Slave-Fermion transformations). One can notice that in fact,

$$\hat{T}_m = \mathcal{M}\mathcal{R}_B\hat{T}_s\mathcal{R}_A^\dagger\mathcal{M}^\dagger = \mathcal{M}\hat{T}_s\mathcal{M}^\dagger, \tag{5.14}$$

which can be understood as a translation followed by a rotation of all the spins.

In the undoped case, when $\lambda = 1$, the model commutes with the translation operator $\hat{T}_s$, but for $\lambda \neq 1$ it does not commute anymore. The latter can be observed by evaluating

$$[\mathcal{M}\mathcal{R}_A\hat{T}_s\mathcal{R}_A^\dagger\mathcal{M}^\dagger, \hat{\mathcal{H}}]|\varnothing\rangle = NJ(\lambda-1)\mathcal{M}\mathcal{R}_B\mathcal{R}_A^\dagger\mathcal{M}^\dagger|\varnothing\rangle, \tag{5.15}$$

where N denotes the number of sites. This happens because we rotate one sublattice to introduce magnons, which leads to a 2-site long unit cell. Thus using standard momentum states to block diagonalize the model for $\lambda \neq 1$ we would only have half of k-points. On the other hand, we have,

$$[\hat{T}_m, \hat{\mathcal{H}}] = 0, \tag{5.16}$$

which holds true also when $\lambda \neq 1$. Formally, it does not matter which translation operator we use to form a momentum state basis. Each of them comes with benefits and drawbacks. But as we will later show, on the level of the spectral function there will be a one-to-one correspondence between the momentum k of the hole introduced to the system and momentum k of the subspace of the Hamiltonian, even when those are obtained using different translation operators. Therefore, to block diagonalize the model we use $\hat{T}_m$ in the definition of a momentum state,

$$|\varphi(p)\rangle = \frac{1}{\sqrt{N_\varphi}}\sum_{r=0}^{N-1} \mathrm{e}^{-ipr}\hat{T}_m^r|\varphi\rangle. \tag{5.17}$$

Here $|\varphi\rangle$ is a representative state in polaronic language with periodicity R_φ. Periodicity R_φ is defined as the smallest non-zero number of translations $\hat{T}_m$ that transform state $|\varphi\rangle$ onto itself. Then it follows, $N_\varphi R_\varphi = N^2$. To distinguish momentum states obtained with $\hat{T}_m$ operator from momentum states obtained with $\hat{T}_s$ we label the former with p instead of k. For simplicity, we will refer to this new momentum p as *rotating* momentum, as $\hat{T}_m$ shifts all the spins by one site and then rotates them.

Our t–J Hamiltonian (regardless of the value of λ) conserves magnetization thus splitting the basis accordingly before introducing momentum states will lead to significant improvement of the maximum system size that can be studied. Since $\hat{T}_m$ mixes subspaces of opposite magnetization, one may do the trick by splitting the basis with respect to the absolute value of the magnetization. In all the investigated cases the ground state of the undoped case always belongs to the subspace with the smallest absolute value of magnetization. Restricting ourselves to even system sizes we need to take into consideration only states with the same number of spins up and down in the undoped case.

Further reduction of the computational effort may be obtained by considering the relation between *rotating* momentum q of the Heisenberg ground state, momentum k of the removed electron, and *rotating* momentum p of the eigenstates of the t-J model with a single hole. To understand it, let us have a look at the quantity of interest, the

momentum-dependent Green's function defined through Eq. (1.3). After introducing *rotating* momentum basis we can write,

$$G(k,\omega) = \sum_{p} \sum_{i \in I(p)} \frac{|\langle \varphi_i(p)|\hat{\tilde{c}}_{k\sigma}|\psi_{\mathrm{GS}}(q)\rangle|^2}{\omega - E_i(p) + E_{\mathrm{GS}}(q)}, \tag{5.18}$$

where $I(p)$ denotes the index set of eigenstates of the t–J model with a single hole and scalable magnon interactions within subspace p.

In general, the ground state of a model at half-filling could be located at different q subspaces, e.g. when calculated for different system sizes. In fact, in *rotating* momentum basis ground state of the Heisenberg model can be always found at $q = 0$. This holds true also when $\lambda \neq 1$.

Since the Green's function is parameterized by k, and q is known, the only simplification could therefore come from reducing the sum over p. This can be achieved by noticing the following fact,

$$\begin{aligned} G(k,\omega) &= \langle \psi_{\mathrm{GS}}(q=0)|\hat{\tilde{c}}^{\dagger}_{k\sigma}\hat{G}(\omega)\hat{\tilde{c}}_{k\sigma}|\psi_{\mathrm{GS}}(q=0)\rangle \\ &= \frac{1}{2}\langle \psi_{\mathrm{GS}}(0)|(\hat{\tilde{c}}^{\dagger}_{k\uparrow} + \hat{\tilde{c}}^{\dagger}_{k\downarrow})\hat{G}(\omega)(\hat{\tilde{c}}_{k\uparrow} + \hat{\tilde{c}}_{k\downarrow})|\psi_{\mathrm{GS}}(0)\rangle. \end{aligned} \tag{5.19}$$

Replacing $\hat{\tilde{c}}_{k\sigma}$ by $(\hat{\tilde{c}}_{k\uparrow} + \hat{\tilde{c}}_{k\downarrow})/\sqrt{2}$ in the desired quantity we still obtain the same result. With some careful calculation (remember p and q are not defined the same way k is) one can show for the above formula that only nonzero contribution comes from $p = k$. This way we can significantly reduce the time needed to perform the numerical evaluation of the Green's function for given k.

5.4.2. Relation between momenta p and k

Now we will show step by step how to arrive at the above-stated relation between k and p. Our model Hamiltonian is expressed in the polaronic basis. The relation between state in spin basis $|s\rangle$ and the same state in magnon-holon basis $|m\rangle$ can be simply written as,

$$|m\rangle = \mathcal{M}\mathcal{R}_A|s\rangle. \tag{5.20}$$

In this polaronic basis we introduce momentum states,

$$|m^{\mathrm{rep}}(0), p\rangle = \frac{1}{\sqrt{N_{m^{\mathrm{rep}}}}} \sum_{r=0}^{N-1} \exp(-ipr)\hat{T}^r_m|m^{\mathrm{rep}}(0)\rangle, \tag{5.21}$$

where $|m^{\mathrm{rep}}(0)\rangle$ is a representative state in polaronic basis with $|m^{\mathrm{rep}}(r)\rangle = \hat{T}^r_m|m^{\mathrm{rep}}(0)\rangle$ representing its translation by r sites. In practice, m^{rep} is just a number, whose binary representation reflects the state of the system, where "0" digits correspond to empty sites and "1" digits correspond to sites occupied by single magnon. The normalization factor $N_{m^{\mathrm{rep}}} = \frac{N^2}{R_{m^{\mathrm{rep}}}}$, and $R_{m^{\mathrm{rep}}}$ denotes periodicity of the state $|m^{\mathrm{rep}}(0)\rangle$, i.e. smallest positive number of translations $\hat{T}_m$ that transform $|m^{\mathrm{rep}}(0)\rangle$ onto itself. For more details see Ch. 4 on p. 55-67 of [95].

Operators $\hat{T}_s$ and $\hat{T}_m$ are related in the following way,

$$\hat{T}_m = \mathcal{M}\mathcal{R}_B\hat{T}_s\mathcal{R}^{\dagger}_A\mathcal{M}^{\dagger} = \mathcal{M}\hat{T}_s\mathcal{R}_A\mathcal{R}^{\dagger}_A\mathcal{M}^{\dagger} = \mathcal{M}\hat{T}_s\mathcal{M}^{\dagger}, \tag{5.22}$$

and the annihilation of the electron operator is simply,

$$\hat{\tilde{c}}^{(m)}_{r\sigma A} = \mathcal{M}\mathcal{R}_A \hat{\tilde{c}}_{r\sigma} \mathcal{R}_A^\dagger \mathcal{M}^\dagger, \tag{5.23}$$

where $\hat{\tilde{c}}^{(m)}_{r\sigma A}$ annihilates the electron in polaronic basis. Here $\sigma = +\frac{1}{2}$ with $r \in A$ or $\sigma = -\frac{1}{2}$ with $r \in B$ can be understood as presence of the magnon at site r. In terms of slave-fermion operators we can write,

$$\hat{\tilde{c}}^{(m)}_{r\sigma A} = \begin{cases} \hat{h}_i^\dagger \hat{P}_i, & \text{if } r \in A \wedge \sigma = -\frac{1}{2} \text{ or } r \notin A \wedge \sigma = +\frac{1}{2} \\ \hat{h}_i^\dagger \hat{P}_i \hat{a}_i, & \text{if } r \in A \wedge \sigma = +\frac{1}{2} \text{ or } r \notin A \wedge \sigma = -\frac{1}{2} \end{cases} \tag{5.24}$$

Note that the above is just a shorthand notation that we use to shorten further equations. For practical reasons in the implementation of the exact diagonalization algorithm, there is no need to actually keep track of whether we annihilate magnon or not when we create a hole. It is just enough to know where the hole is. This way we remember the magnetic configuration of the states before the hole was introduced. In the end, we want to arrive at the expression without operators, so it is enough to know what we have to do with the state when we say, we remove an electron (or introduce a hole).

We want to calculate the Green's function of the single hole, which can be expressed as,

$$G(k,\omega) = \frac{1}{2} \sum_p \sum_{i \in I(p)} \frac{|\langle \varphi_i(p)| \left(\hat{\tilde{c}}_{k\sigma} + \hat{\tilde{c}}_{k\bar{\sigma}} \right) |\psi_{\mathrm{GS}}(q)\rangle|^2}{\omega - E_i(p) + E_{\mathrm{GS}}(q)}, \tag{5.25}$$

where q is known. Expressing annihilation operators in the polaronic basis we get,

$$\begin{aligned} \hat{\tilde{c}}_{k\sigma} &= \frac{1}{\sqrt{N}} \sum_{r=0}^{N-1} \exp(-ikr) \hat{T}_s^r \hat{\tilde{c}}_{0\sigma} \hat{T}_s^{-r} \\ &= \frac{1}{\sqrt{N}} \sum_{r=0}^{N-1} \exp(-ikr) \mathcal{R}^\dagger_{\xi(r)} \mathcal{M}^\dagger \hat{T}_m^r \hat{\tilde{c}}^{(m)}_{0\sigma A} \hat{T}_m^{-r} \mathcal{M} \mathcal{R}_{\xi(r)} \\ &= \frac{1}{\sqrt{N}} \sum_{r=0}^{N-1} \exp(-ikr) \mathcal{R}^\dagger_{\xi(r)} \mathcal{M}^\dagger \hat{\tilde{c}}^{(m)}_{r\sigma A} \mathcal{M} \mathcal{R}_{\xi(r)} \\ &= \mathcal{R}_A^\dagger \mathcal{M}^\dagger \hat{\tilde{c}}^{(m)}_{k\sigma A} \mathcal{M} \mathcal{R}_A. \end{aligned} \tag{5.26}$$

where $\xi(r \in A(B)) = A(B)$ respectively. The definition of $\hat{\tilde{c}}^{(m)}_{k\sigma A}$ is such that,

$$\langle s' | \hat{\tilde{c}}_{k\sigma} | s \rangle = \langle m' | \hat{\tilde{c}}^{(m)}_{k\sigma A} | m \rangle. \tag{5.27}$$

Let us rewrite states $\langle \varphi_i(p)|$ and $|\psi_{\mathrm{GS}}(q)\rangle$ in a somewhat more useful way,

$$|\psi_{\mathrm{GS}}(q)\rangle = \mathcal{R}_A^\dagger \mathcal{M}^\dagger \sum_{m^{\mathrm{rep}}(0)} a_{m^{\mathrm{rep}}(0)}(q) |m^{\mathrm{rep}}(0), q\rangle, \tag{5.28}$$

$$\langle \varphi_i(p)| = \sum_m b_m^{(i)}(p)^* \langle m, N-1, p| \mathcal{M}\mathcal{R}_A, \tag{5.29}$$

where m denotes configuration of magnons and $N-1$ stands for position of the hole in representative state $\langle m, N-1, p|$. As the representative states we chose those with

the hole in the last site, but in general, it does not matter which site we chose due to periodic boundary conditions. Moreover, $a_{m^{\mathrm{rep}}(0)}(q)$ is a coefficient of the ground state wave function $|\psi_{\mathrm{GS}}(q)\rangle$ corresponding to momentum state $|m^{\mathrm{rep}}(0), q\rangle$ and $b_m^{(i)}(p)$ is in similar way coefficient of the i-th wave function of the model with a single hole that stands in front of momentum state $|m, N-1, p\rangle$. This way we have,

$$\begin{aligned}\langle\varphi_i(p)|\left(\hat{\tilde{c}}_{k\sigma}+\hat{\tilde{c}}_{k\bar{\sigma}}\right)|\psi_{\mathrm{GS}}(q)\rangle = \\ \sum_m\sum_{m^{\mathrm{rep}}(0)} a_{m^{\mathrm{rep}}(0)}(q)b_m^{(i)}(p)^*\langle m, N-1, p|\left(\hat{\tilde{c}}^{(m)}_{k\sigma A}+\hat{\tilde{c}}^{(m)}_{k\bar{\sigma}A}\right)|m^{\mathrm{rep}}(0), q\rangle.\end{aligned} \tag{5.30}$$

Now we will just work out the above to show that for given k, q the only contribution comes from $p = k + q$. The important thing to notice is, that in our system for any state $|\varphi\rangle$ within the polaronic basis we have,

$$\mathcal{M}\mathcal{R}_A\mathcal{R}^\dagger_{\xi(r)}\mathcal{M}^\dagger\left(\hat{\tilde{c}}^{(m)}_{r\sigma A}+\hat{\tilde{c}}^{(m)}_{r\bar{\sigma}A}\right)\mathcal{M}\mathcal{R}_{\xi(r)}\mathcal{R}^\dagger_A\mathcal{M}^\dagger|\varphi\rangle = \left(\hat{\tilde{c}}^{(m)}_{r\sigma A}+\hat{\tilde{c}}^{(m)}_{r\bar{\sigma}A}\right)|\varphi\rangle. \tag{5.31}$$

This is simple to understand. We can annihilate either spin up or down at site r. Since we have a sum of operators for both spins the whole bracket will always annihilate an electron, regardless of the rotations of spins. Finally, rotations are performed twice (once before annihilation, and once after), so the resulting state is not rotated w.r.t. the initial state. Thus we obtain,

$$\begin{aligned}\left(\hat{\tilde{c}}^{(m)}_{k\sigma A}+\hat{\tilde{c}}^{(m)}_{k\bar{\sigma}A}\right)|m^{\mathrm{rep}}(0), q\rangle = \\ \frac{1}{\sqrt{NN_{m^{\mathrm{rep}}}}}\sum_{R=0}^{N-1}\sum_{l=0}^{N-1} e^{-ikR-iql}\left(\hat{\tilde{c}}^{(m)}_{R\sigma A}+\hat{\tilde{c}}^{(m)}_{R\bar{\sigma}A}\right)\hat{T}^l_m|m^{\mathrm{rep}}(0)\rangle = \\ \frac{1}{\sqrt{NN_{m^{\mathrm{rep}}}}}\sum_{R=0}^{N-1}\sum_{l=0}^{N-1} e^{-ikR-i(k+q)l}\hat{T}^l_m\left(\hat{\tilde{c}}^{(m)}_{R\sigma A}+\hat{\tilde{c}}^{(m)}_{R\bar{\sigma}A}\right)|m^{\mathrm{rep}}(0)\rangle = \\ \frac{1}{\sqrt{NN_{m^{\mathrm{rep}}}}}\sum_{R=0}^{N-1}\sum_{l=0}^{N-1} e^{-ikR-i(k+q)l}|m^{\mathrm{rep}}(l), R+l\rangle.\end{aligned} \tag{5.32}$$

Above, the state $|m^{\mathrm{rep}}(l), R + l\rangle$ is a state with a hole located at site $R + l$. We can write,

$$|m^{\mathrm{rep}}(l), R+l\rangle = \hat{T}_m^{R+l+1}|m', N-1\rangle, \tag{5.33}$$

where $m' = m^{\mathrm{rep}}(N-1-R)$. This way we see that,

$$\begin{aligned}\langle m, N-1, p|\sum_{R,l=0}^{N-1} e^{-ikR-i(k+q)l}\hat{T}_m^{R+l+1}|m', N-1\rangle \\ = \frac{e^{ip}}{\sqrt{N}}\sum_{R,l=0}^{N-1} e^{i(p-k)R}e^{i(p-(k+q))l}\delta_{m,m'} = e^{ip}\sqrt{N}\sum_{R=0}^{N-1} e^{i(p-k)R}\delta_{p,k+q}\delta_{m,m'}.\end{aligned} \tag{5.34}$$

So indeed, $\delta_{p,k+q}$ ensures that the only contribution comes from $p = k + q$. Moreover, as we mentioned before, the ground state of the model without holes happens to be

located at $q = 0$. Therefore we have $p = k$, and in the end we obtain,

$$G(k,\omega) = \sum_{i\in I(k)} \frac{\left| \sum_{m} \sum_{m^{\mathrm{rep}}(0)} \frac{a_{m^{\mathrm{rep}}(0)}(0) b_m^{(i)}(k)^* e^{ik}}{2\sqrt{N_{m^{\mathrm{rep}}}}} \sum_{R=0}^{N-1} \delta_{m,m^{\mathrm{rep}}(N-1-R)} \right|^2}{\omega - E_i(k) + E_{\mathrm{GS}}(0)}. \tag{5.35}$$

5.5. Conclusions

We numerically study the 1D t–J model with scalable magnon-magnon interactions, Eq. (1.22). Although the overall shape of the spectral function $A(\omega)$ of a single hole introduced to undoped t–J chain seems similar with and without magnon-magnon interactions (see Fig. 5.1) the detailed studies of the quasiparticle weight and energy gap (see Fig. 5.4) reveal that when magnon-magnon interactions are missing the ground state is a quasiparticle. Further, by studying spin-hole-spin correlations $C(s,d)$ we confirm that the spin-charge separation picture in 1D t–J model is unstable to collapse into a spin polaron, see Sec. 5.2.1. Analyzing the ground state wave function in terms of probabilities c_n of finding the chain of n magnons attached to the hole (see Sec. 5.2.2) we can confidently say that the exact value of magnon-magnon interactions $\lambda = 1$ is a unique case (the same was also true for the 1D t–J^z model, see Ch. 2). For $\lambda \neq 1$ the ground state should be understood as a spin polaron, and only when $\lambda = 1$ (exact case of the t–J model) the spin-charge separation is recovered as the size of the spin polaron in this case grows to infinity. This shows that magnon-magnon interactions play a crucial role in determining the physics of the single hole in the 1D antiferromagnet.

We discuss the relevance of our studies for understanding ARPES measurements on *quasi*-1D cuprates, see Sec. 5.3. We show that the small interchain coupling present in 1D cuprates can be described by the t–J model with rescaled magnon-magnon interactions [and with small XXZ anisotropy, see Eq. (5.9)]. This qualitatively changes the physical picture of a hole in the 1D cuprates, cf. Fig 5.7 and 5.9. The ground state of *quasi*-1D cuprates should be rather seen as a spin polaron. Altogether, the physics of the hole in 1D and 2D antiferromagnets turns out to be much more similar than different.

Chapter 6

Summary

Let us summarize the presented studies by contrasting the common understanding of the problem of a single hole in the t–J and t–J^z model with the findings of this thesis. We will cover here four cases discussed in the main chapters of the thesis:

I. 1D t–J^z model, see Ch. 2,

II. t–J^z model on a Bethe lattice with coordination $z = 4$, see Ch. 2,

III. 2D t–J^z model, see Ch. 3 and Ch. 4,

IV. 1D t–J model, see Ch. 5.

We provide new insights into the problem of a single hole in all the above cases. Besides we update the state-of-the-art spectral function of a single hole in some of them, providing not only detailed calculations but also deep understanding. We will go one by one, in each case starting the description by discussing the general understanding of single-hole physics in that case. Then we will contrast it with the results presented in this thesis including a discussion of the spectral function or ground state and excited states properties.

I. 1D t–J^z model.

The broadly agreed understanding is that the spectral function of a single hole in this case consists of a single delta-like peak at the ground state energy and a broad incoherent spectrum of excited states split from the ground state for all couplings $J/t > 0$, see Fig. 2.3. The hole introduced to the otherwise undoped system creates a single immobile spinon and later can separate and move freely in the system, see Fig. 1.2. In this sense, the physics of a single hole in 1D t–J^z model is often understood in terms of spin-charge separation.

Out understanding: In this thesis, we study the 1D t–J^z model in magnon-holon basis, where propagating hole excites or annihilates magnons in the system. It turns out that the critical value of the magnon-magnon interactions in this case removes the cost of creating consecutive magnons by the hole, thus only the very first magnon costs non-zero energy, see Fig. 2.8.(a2). Nevertheless, this is enough to bind the hole, as it turns out that the probability P_n of finding states with chains of n magnons attached to the hole decays exponentially with n, see Fig. 2.8.(a1). By varying the strength λ of magnon-magnon interactions we discover that the ladder spectrum in excited states

is formed for all the values of the interaction but one—the exact case of the 1D t–J^z model ($\lambda = 1$), cf. Eq. (2.19) and (2.31). For this particular value, the ladder spectrum disappears as the energy difference between the excited states drops to 0.

II. t–J^z model on a Bethe lattice with coordination $z > 2$.

The broadly agreed understanding of this problem is such that the hole introduced to the undoped system becomes subject to a perfect discrete linear potential from disrupted AF order. The energy in the system is proportional to the number of spins shifted out of the order created by the moving hole. This results in a discrete set of energy levels giving rise to a ladder-like spectral function of a single hole. The distance between energy levels scales like $(J/t)^{2/3}$ in an analog to a problem of a particle in a triangular well.

Out understanding: In magnon-holon basis, the mobile hole propagates through the system and excites immobile magnons. Each such magnon costs non-zero energy, see Fig. 2.8.(c2-d2). Neglecting the magnon-magnon interactions only quantitatively affects the spectral function of a single hole resulting in rescaled distance between the peaks in the ladder spectrum, cf. Fig 2.4 and 2.5. New insights into the problem come from studying the ground state properties. We discover that the cloud of magnons around the hole decays superexponentially in space as a result of the linear energy growth in the system with the number of magnons, see Fig. 2.8. By contrasting this result with the quantum gas microscopy experiments on the 2D Hubbard model we conclude that the hole in a doped Hubbard model at finite temperature is not subject to a linear potential, see Sec. 2.3.3.

III. 2D t–J^z model.

The broadly agreed understanding of a hole in 2D t–J^z model is mostly the same as in the case of the Bethe lattice. When the hole propagates in the system the disrupted AF order acts as an attractive potential on the hole resulting in the autolocalized state. Calculations based on SCBA or the diagrammatic approach yield the ladder-like spectrum for the spectral function of a single hole with energy gaps between peaks scaling as $(J/t)^{2/3}$. The only difference compared to the Bethe lattice case, seems to be related to the possibility for the hole to move in loops on the 2D square lattice. This gives rise to a finite broadening of the spectral lines, which is supposed to explain the discrepancies between analytical approaches and exact diagonalization. Magnon-magnon interactions are not considered important.

Out understanding: Apart from the well-known vibrational states scaling as $(J/t)^{2/3}$, we show the existence of two other types of states in the t–J^z model with a single hole on a 2D square lattice: states with linear energy gap scaling $\propto J/t$, and densely packed (in energy) states forming a broad incoherent spectrum.

We show that the discrete linear potential from created magnons is substantially warped when magnon-magnon interactions are taken into account exactly on the 2D square lattice, cf. 3.5 and 3.6. Developed by us the self-avoiding walks approximation (see Sec. 3.2) for the 2D t–J^z model shows that the contribution from the magnon-magnon interactions is enough to obtain a very good agreement of the spectral function with the exact diagonalization results for all studied couplings $J/t > 0.4$, see Fig. 3.7. The contribution from loops seems then negligible for studied system parameters. Surprisingly, the spectral function is not of the ladder-like type, but it consists of a quasi-

particle peak at the single-hole ground state energy and a broad incoherent spectrum of the excited states. We provide a detailed understanding of the collapse of the ladder spectrum as a result of the magnon-magnon interactions and tangential paths present on the 2D square lattice, see Sec. 3.3.2.

Then we study the rotational degrees of freedom for the hole in the 2D t–J^z model and discover that rotational modes with energy scaling $\propto J/t$ hybridize with the vibrational modes $(J/t)^{2/3}$ on the square lattice (but not on the Bethe lattice), see Fig. 4.1. We explain the onset of linear dependence is due to the symmetry of the rotational states producing leftover magnons, which cannot be annihilated, see Sec. 4.4.1. Moreover, we introduce a toy model showing that the hybridization of the rotational and vibrational modes originates in the lack of perfect C_3 symmetry for the hole moving *forward* in the square lattice (such symmetry is present on the Bethe lattice with coordination $z = 4$), see Sec. 4.4.2.

IV. 1D t–J model.

It is widely known that the spectral function of a single hole introduced to the Heisenberg antiferromagnet is fully incoherent. This is a result of the lack of electronic quasiparticles where instead the spin and charge degrees of freedom separate and move independently of each other in the thermodynamic limit.

Out understanding: In magnon-holon basis, the moving holon can create magnons for free thanks to the critical value of the magnon-magnon interactions and to the quantum spin fluctuations which remove the cost of the very first magnon as well. As a result, the holon can dress in infinitely many magnons. Spin-charge separation is therefore equivalent to infinitely large spin polaron. This is confirmed by studying the single-hole ground state wave function as no decay for states with higher numbers of magnons is observed, see Fig. 5.7. On the other hand, it turns out the spin-charge separation is a fragile state, unstable to collapse into spin polaron for infinitesimal perturbation of the magnon-magnon interactions, see discussions in Ch. 5, e.g. due to the small staggered field coming from other chains in *quasi*-1D cuprates, see Sec. 5.3. This has an important consequence for the interpretation of the ARPES experiments on *quasi*-1D cuprates, where the spin-charge separation is replaced by a spin polaron.

Bibliography

[1] N. F. Mott, Proceedings of the Physical Society. Section A, **62**, 416–422 (1949).

[2] F. Bloch, Zeitschrift für Physik, **52**, 555–600 (1929).

[3] C. Kittel, *Introduction to Solid State Physics*, Wiley, New York, 1996.

[4] M. Imada, A. Fujimori, and Y. Tokura, Rev. Mod. Phys., **70**, 1039–1263 (1998).

[5] D. I. Khomskii, *Basic Aspects of the Quantum Theory of Solids: Order and Elementary Excitations*, Cambridge University Press, Cambridge, 2010.

[6] Y. Krockenberger, B. Eleazer, H. Irie, and H. Yamamoto, Journal of the Physical Society of Japan, **83**, 114602 (2014).

[7] C. Ye, P. Cai, R. Yu, X. Zhou, W. Ruan, Q. Liu, C. Jin, and Y. Wang, Nature Communications, **4**, 1365 (2013).

[8] M. R. Norman and C. Pépin, Reports on Progress in Physics, **66**, 1547 (2003).

[9] H. Yamauchi and M. Karppinen, Materials Science and Engineering: B, **54**, 92–97 (1998).

[10] M. Napoletano, J. Gallardo Amores, E. Magnone, G. Busca, and M. Ferretti, Physica C: Superconductivity, **319**, 229–237 (1999).

[11] Z. Hiroi, N. Kobayashi, and M. Takano, Nature, **371**, 139–141 (1994).

[12] Z. Hiroi, N. Kobayashi, and M. Takano, Physica C: Superconductivity, **266**, 191–202 (1996).

[13] Y. Tokura, H. Takagi, and S. Uchida, Nature, **337**, 345–347 (1989).

[14] A. Guarino, C. Autieri, P. Marra, A. Leo, G. Grimaldi, A. Avella, and A. Nigro, Phys. Rev. B, **105**, 014512 (2022).

[15] M. B. Maple, MRS Bulletin, **15**, 60–67 (1990).

[16] H. Takagi, S. Uchida, and Y. Tokura, Phys. Rev. Lett., **62**, 1197–1200 (1989).

[17] B. Keimer, S. A. Kivelson, M. R. Norman, S. Uchida, and J. Zaanen, Nature, **518**, 179–186 (2015).

[18] E. Dagotto, Rev. Mod. Phys., **66**, 763–840 (1994).

[19] J. G. Bednorz and K. A. Müller, Zeitschrift für Physik B Condensed Matter, **64**, 189–193 (1986).

[20] A. Damascelli, Z. Hussain, and Z.-X. Shen, Rev. Mod. Phys., **75**, 473–541 (2003).

[21] L. N. Cooper, Phys. Rev., **104**, 1189–1190 (1956).

[22] D. J. Scalapino, Rev. Mod. Phys., **84**, 1383–1417 (2012).

[23] P. Radaelli, J. Wagner, B. Hunter, M. Beno, G. Knapp, J. Jorgensen, and D. Hinks, Physica C: Superconductivity, **216**, 29–35 (1993).

[24] F. C. Zhang and T. M. Rice, Phys. Rev. B, **37**, 3759–3761 (1988).

[25] J. Hubbard, Proc. Roy. Soc. (London), **276**, 238–257 (1963).

[26] H. Q. Lin and J. E. Hirsch, Phys. Rev. B, **35**, 3359–3368 (1987).

[27] Z. Chen, Y. Wang, S. N. Rebec, T. Jia, M. Hashimoto, D. Lu, B. Moritz, R. G. Moore, T. P. Devereaux, and Z.-X. Shen, Science, **373**, 1235–1239 (2021).

[28] E. H. Lieb and F. Y. Wu, Physical Review Letters, **20**, 1445–1448 (1968).

[29] E. H. Lieb and F. Wu, Physica A: Statistical Mechanics and its Applications, **321**, 1–27 (2003). Statphys-Taiwan-2002: Lattice Models and Complex Systems.

[30] K. A. Chao, J. Spałek, and A. M. Oleś, Phys. Rev. B, **18**, 3453–3464 (1978).

[31] M. Daghofer, K. Wohlfeld, A. M. Oleś, E. Arrigoni, and P. Horsch, Phys. Rev. Lett., **100**, 066403 (2008).

[32] K. Wohlfeld, M. Daghofer, A. M. Oleś, and P. Horsch, Phys. Rev. B, **78**, 214423 (2008).

[33] V. Y. Krivnov and D. V. Dmitriev, Russian Journal of Physical Chemistry A, **88**, 1914–1921 (2014).

[34] K. Liu, Z.-Y. Lu, and T. Xiang, Phys. Rev. Mater., **3**, 044802 (2019).

[35] B. J. Kim, H. Koh, E. Rotenberg, S.-J. Oh, H. Eisaki, N. Motoyama, S. Uchida, T. Tohyama, S. Maekawa, Z.-X. Shen, and C. Kim, Nature Physics, **2**, 397–401 (2006).

[36] A. E. Feiguin, C. Helman, and A. A. Aligia, *Effective one-band models for the 1D cuprate* $Ba_{2-x}Sr_xCuO_{3+\delta}$, arXiv:2303.11905 (2023).

[37] M. Brunner, F. F. Assaad, and A. Muramatsu, The European Physical Journal B - Condensed Matter and Complex Systems, **16**, 209–212 (2000).

[38] H. Zhang, T. Pincelli, C. Jozwiak, T. Kondo, R. Ernstorfer, T. Sato, and S. Zhou, Nature Reviews Methods Primers, **2**, 54 (2022).

[39] J. A. Sobota, Y. He, and Z.-X. Shen, Rev. Mod. Phys., **93**, 025006 (2021).

[40] A. Einstein, Annalen der Physik, **322**, 132–148 (1905).

[41] H. Iwasawa, E. Schwier, M. Arita, A. Ino, H. Namatame, M. Taniguchi, Y. Aiura, and K. Shimada, Ultramicroscopy, **182**, 85 (2017).

[42] N. F. Mott and R. Peierls, Proceedings of the Physical Society, **49**, 72 (1937).

[43] P. W. Anderson, Phys. Rev., **115**, 2–13 (1959).

[44] J. Voit, Reports on Progress in Physics, **58**, 977 (1995).

[45] C. Kim, A. Y. Matsuura, Z.-X. Shen, N. Motoyama, H. Eisaki, S. Uchida, T. Tohyama, and S. Maekawa, Phys. Rev. Lett., **77**, 4054–4057 (1996).

[46] C. Kim, Z.-X. Shen, N. Motoyama, H. Eisaki, S. Uchida, T. Tohyama, and S. Maekawa, Phys. Rev. B, **56**, 15589–15595 (1997).

[47] H. Fujisawa, T. Yokoya, T. Takahashi, S. Miyasaka, M. Kibune, and H. Takagi, Phys. Rev. B, **59**, 7358–7361 (1999).

[48] D. Poilblanc, A. Läuchli, M. Mambrini, and F. Mila, Phys. Rev. B, **73**, 100403 (2006).

[49] A. Koitzsch, S. V. Borisenko, J. Geck, V. B. Zabolotnyy, M. Knupfer, J. Fink, P. Ribeiro, B. Büchner, and R. Follath, Phys. Rev. B, **73**, 201101 (2006).

[50] J. Vijayan, P. Sompet, G. Salomon, J. Koepsell, S. Hirthe, A. Bohrdt, F. Grusdt, I. Bloch, and C. Gross, Science, **367**, 186–189 (2020).

[51] T. Giamarchi, *Quantum Physics in One Dimension*, Oxford University Press, Dec. 2003.

[52] L. N. Bulaevskii, E. L. Nagaev, and D. I. Khomskii, JETP, **27**, 836 (1968).

[53] S. Schmitt-Rink, C. M. Varma, and A. E. Ruckenstein, Phys. Rev. Lett., **60**, 2793–2796 (1988).

[54] G. Martinez and P. Horsch, Phys. Rev. B, **44**, 317–331 (1991).

[55] F. Grusdt, M. Kánasz-Nagy, A. Bohrdt, C. S. Chiu, G. Ji, M. Greiner, D. Greif, and E. Demler, Phys. Rev. X, **8**, 011046 (2018).

[56] C. S. Chiu, G. Ji, A. Bohrdt, M. Xu, M. Knap, E. Demler, F. Grusdt, M. Greiner, and D. Greif, Science, **365**, 251–256 (2019).

[57] J. Koepsell, J. Vijayan, P. Sompet, F. Grusdt, T. A. Hilker, E. Demler, G. Salomon, I. Bloch, and C. Gross, Nature, **572**, 358–362 (2019).

[58] Y. Wang, A. Bohrdt, S. Ding, J. Koepsell, E. Demler, and F. Grusdt, Phys. Rev. Research, **3**, 033204 (2021).

[59] A. Bohrdt, Y. Wang, J. Koepsell, M. Kánasz-Nagy, E. Demler, and F. Grusdt, Phys. Rev. Lett., **126**, 026401 (2021).

[60] Y. Wang, K. Wohlfeld, B. Moritz, C. J. Jia, M. van Veenendaal, K. Wu, C.-C. Chen, and T. P. Devereaux, Phys. Rev. B, **92**, 075119 (2015).

[61] F. Ronning, K. M. Shen, N. P. Armitage, A. Damascelli, D. H. Lu, Z.-X. Shen, L. L. Miller, and C. Kim, Phys. Rev. B, **71**, 094518 (2005).

[62] S. Maekawa and T. Tohyama, Reports on Progress in Physics, **64**, 383 (2001).

[63] K. M. Kojima, Y. Fudamoto, M. Larkin, G. M. Luke, J. Merrin, B. Nachumi, Y. J. Uemura, N. Motoyama, H. Eisaki, S. Uchida, K. Yamada, Y. Endoh, S. Hosoya, B. J. Sternlieb, and G. Shirane, Phys. Rev. Lett., **78**, 1787–1790 (1997).

[64] M. Matsuda, K. Katsumata, K. M. Kojima, M. Larkin, G. M. Luke, J. Merrin, B. Nachumi, Y. J. Uemura, H. Eisaki, N. Motoyama, S. Uchida, and G. Shirane, Phys. Rev. B, **55**, R11953–R11956 (1997).

[65] T. Holstein and H. Primakoff, Phys. Rev., **58**, 1098–1113 (1940).

[66] J. König and A. Hucht, SciPost Phys., **10**, 007 (2021).

[67] F. Grusdt and L. Pollet, Phys. Rev. Lett., **125**, 256401 (2020).

[68] A. Bohrdt, E. Demler, and F. Grusdt, Phys. Rev. Lett., **127**, 197004 (2021).

[69] K. K. Nielsen, Phys. Rev. B, **106**, 115144 (2022).

[70] O. A. Starykh and G. F. Reiter, Phys. Rev. B, **53**, 2517–2522 (1996).

[71] S. Sorella and A. Parola, Phys. Rev. B, **57**, 6444–6473 (1998).

[72] C. L. Kane, P. A. Lee, and N. Read, Phys. Rev. B, **39**, 6880–6897 (1989).

[73] J. S. Gardner, M. J. P. Gingras, and J. E. Greedan, Rev. Mod. Phys., **82**, 53–107 (2010).

[74] A. A. Aczel, A. M. Cook, T. J. Williams, S. Calder, A. D. Christianson, G.-X. Cao, D. Mandrus, Y.-B. Kim, and A. Paramekanti, Phys. Rev. B, **93**, 214426 (2016).

[75] G. Watson, *A Treatise on the Theory of Bessel Functions*, Cambridge Mathematical Library, Cambridge University Press, 1995.

[76] A. L. Chernyshev and P. W. Leung, Phys. Rev. B, **60**, 1592–1606 (1999).

[77] K. Bieniasz, P. Wrzosek, A. M. Oles, and K. Wohlfeld, SciPost Phys., **7**, 066 (2019).

[78] G. F. Reiter, Phys. Rev. B, **49**, 1536–1539 (1994).

[79] A. Bohrdt, C. S. Chiu, G. Ji, M. Xu, D. Greif, M. Greiner, E. Demler, F. Grusdt, and M. Knap, Nature Physics, **15**, 921–924 (2019).

[80] P. Wrzosek and K. Wohlfeld, Phys. Rev. B, **103**, 035113 (2021).

[81] F. Grusdt, E. Demler, and A. Bohrdt, SciPost Phys., **14**, 090 (2023).

[82] E. Merzbacher, *Quantum mechanics*, J. Wiley, New York, 2d ed ed., 1970.

[83] F. Gantmakher, *The Theory of Matrices*, no. t. 1 in AMS Chelsea Publishing Series, Chelsea Publishing Company, 1959.

[84] J. Koepsell, D. Bourgund, P. Sompet, S. Hirthe, A. Bohrdt, Y. Wang, F. Grusdt, E. Demler, G. Salomon, C. Gross, and I. Bloch, Science, **374**, 82–86 (2021).

[85] D. Sénéchal, D. Perez, and M. Pioro-Ladrière, Phys. Rev. Lett., **84**, 522–525 (2000).

[86] R. Eder and Y. Ohta, Phys. Rev. B, **56**, 2542–2550 (1997).

[87] C. Kim, Z.-X. Shen, N. Motoyama, H. Eisaki, S. Uchida, T. Tohyama, and S. Maekawa, Phys. Rev. B, **56**, 15589–15595 (1997).

[88] P. Wrzosek, A. Kłosiński, Y. Wang, M. Berciu, C. E. Agrapidis, and K. Wohlfeld, *The fate of the spin polaron in the 1D antiferromagnets*, arXiv:2203.01846 (2022).

[89] S. Haas, Phys. Rev. Lett., **80**, 4052–4055 (1998).

[90] S. Sorella and A. Parola, Phys. Rev. Lett., **76**, 4604–4607 (1996).

[91] T. A. Hilker, G. Salomon, F. Grusdt, A. Omran, M. Boll, E. Demler, I. Bloch, and C. Gross, Science, **357**, 484–487 (2017).

[92] F. Grusdt, Z. Zhu, T. Shi, and E. Demler, SciPost Phys., **5**, 057 (2018).

[93] S. Li, A. Nocera, U. Kumar, and S. Johnston, Communications Physics, **4**, 217 (2021).

[94] H. J. Schulz, Phys. Rev. Lett., **77**, 2790–2793 (1996).

[95] A. W. Sandvik, A. Avella, and F. Mancini, AIP, **1297**, 135–338 (2010).